UNIVERSITY OF OKLAHOMA

GRADUATE COLLEGE

LONG OFFSET SEISMIC DATA ANALYSIS FOR RESOURCE PLAYS

A DISSERTATION

SUBMITTED TO THE GRADUATE FACULTY

in partial fulfillment of the requirements for the

Degree of

DOCTOR OF PHILOSOPHY

By

BO ZHANG
Norman, Oklahoma
2014

LONG OFFSET SEISMIC DATA ANALYSIS FOR RESOURCE PLAYS

A DISSERTATION APPROVED FOR THE
CONOCOPHILLIPS SCHOOL OF GEOLOGY AND GEOPHYSICS

BY

Dr. Kurt J. Marfurt, Chair

Dr. Ze'ev Reches

Dr. Benjamin Shiau

Dr. Isaac Hall

Dr. Jamie Rich

I would like to dedicate this dissertation to my family and friends whose support, patience, and persistent encouragement was instrumental in allowing me to complete this degree program.

Acknowledgements

I would never have been able to finish my dissertation without the help, support, patient guidance from my principal supervisor, Kurt Marfurt. Through the four years, He provided me with the freedom and unwavering continuous support for doing research. Thank you for developing my geophysics skills and the help on my life side. Your knowledge and noble qualities will be lifetime wealth for me.

I would like to extend my sincere gratitude to the members of my committee: Ze'ev Reches, Benjamin Shiau, Isaac Hall, Jamie Rich, and Xingru Wu for their commitment to serve on my committee and their inspiring comments on my research. Thanks to Tim Kwiatkowski in extending my ability in programming, mathematical and geophysical skills. His encouraging words inspired me to write the prototype interactive residual velocity analysis interface which is now used for velocity analysis in the AASPI consortium.

I appreciate the time and support from fellow students and friends in the AASPI team including Bradley Wallet, Supratik Sarkar, Roderick Perez, Oswaldo Davogustto, Victor Pena, Miguel Angelo, Xavier Refunjol, Ha Mai**,** Jeremy Fisk, Atish Roy, Ozan Elis, Sunday Amoyedo, Lanre Aboaba, Marcus Cahoj, Thang Ha, Alfredo Fernandez Abad, Rachel Barber, and many others not listed for their great help. My sincere thanks go to the Chinese club (Zhonghong Wan, Deshuang Chang, Kui Zhang, Huailai Zhou, Yanxia Guo, Shiguang Guo, Tengfei Lin, Fangyu Li, Jie Qi, and Tao Zhao) of AASPI. They provided key help during these years.

I would like to express my deeply gratitude to my family, my parents, and my grandma in law. Their help and support always was there for me. I deeply apologize that I can't be physically nearer to them.

I would like to express my deepest love to my kids Linyue Zhang, Linwan Zhang, and Linwu Zhang. Your coming into the world bring me a lot of joy in my life.

Finally, I am deeply indebted to my beloved one, Yan Lin for all her support and personal sacrifice in the family. You were always there cheering me up and stood by me through the good times and bad. Without your support and endless love, this work would not have been complete.

Table of Contents

List of Figures

Abstract

Wide-azimuth, long-offset seismic surveys are becoming increasingly common in unconventional exploration plays, where three the key objectives are to estimate the direction of maximum horizontal stress, to predict the intensity and orientation of any fractures, and to differentiate brittle from ductile lithology.

Minimization of NMO and migration stretch, which usually appears at long offset, is one of the main issues for long-offset seismic processing. The stretch not only lowers the seismic resolution, but also hinders subsequent prestack inversion such as lambda-rho ($\lambda\rho$), mu-rho ($\mu\rho$), and amplitude variation with offset and azimuth (AVAz) analysis of the long-offset signal. The first part of this dissertation uses a matching pursuit based normal moveout correction (MPNMO) to reduce NMO-stretch effect in long offset data.

Nonhyperbolic velocity analysis is components for long-offset seismic processing. Conventional migration velocity analysis mainly has two limitations. First we need to interpolate the velocity and anisotropy parameters along spatial and temporal axes between adjacent manually picked locations. Such interpolation can smooth over any intermediate velocity and anisotropy anomalies contained in the gathers. Second, smoothed RMS velocities can give rise to unacceptable interval velocities using the simple Dix equation. I developed an automated nonhyperbolic velocity analysis workflow in the second part of this dissertation that uses the conventional analysis as a starting estimate.

The third part of this dissertation illustrates a workflow to preserve the data fidelity for far offset seismic gathers. The workflow begins by performing reverse NMO on the time migrated gathers using the initial migration velocity. Then I obtain the optimal

velocity and anellipticity model using a differential evolutionary automatic algorithm. Next I apply nonstretch NMO correction to the time migrated gathers using the new velocity and anellipticity model resulting in flattened nonstretched prestack gathers. Finally, I apply prestack structure oriented smoothing algorithm to further improve the signal to noise ratio. In this manner, both stacking power and vertical resolution are improved by aligning the data and by avoiding stretch, and removing migration aliasing artifacts.

The fourth part of this dissertation proposed a strategy to evaluate brittleness of unconventional resources plays by integrating petrophysics and seismic data analysis. I start by computing rock properties and brittleness index (BI) from mineral content logs. Then I define a classification pattern between rock properties and BI using proximal support vector machine training and testing on the selected benchmark wells. Next I perform simultaneous prestack inversion using commercial software on the prestack conditioned seismic gathers. Finally, I estimate 3D brittleness evaluation for the target reservoirs by applying the recognized classification pattern to the prestack inversion volumes.

The final part of my dissertation focuses on automatic fault surfaces extracting using seismic attributes. The extracting procedure is modeled after a biometric algorithm to recognize capillary vein patterns in human fingers. First, a coherence or discontinuity volume is converted to binary form indicating possible fault locations. This binary volume is then skeletonized to produce a suite of fault sticks. Finally, the fault sticks are grouped to construct fault surfaces using a classic triangulation method. The processing in the first two steps is applied time slice by time slice, thereby minimizing the influence of staircase artifacts seen in discontinuity volumes.

.

Chapter 1: Non-stretching NMO correction of prestack time-migrated gathers using a matching-pursuit algorithm

Bo Zhang[1], Kui Zhang[2], Shiguang Guo[1] and Kurt J. Marfurt[1],

[1]The University of Oklahoma, ConocoPhillips School of Geology and Geophysics,

[2]BGP Inc., China National Petroleum Company,

This paper was published by SEG journal Geophysics in 2013.

Title: Non-stretching NMO correction of prestack time-migrated gathers using a matching-pursuit algorithm

ABSTRACT

Wide-azimuth, long-offset surveys are becoming increasingly common in unconventional exploration plays, where two key objectives are to estimate azimuthal anisotropy to predict the direction of maximum horizontal stress, and to differentiate high total organic carbon (TOC) from more “frackable” quartz- and carbonate-rich strata. The conventional NMO correction which processes the data sample-by-sample results in the well-known decrease of frequency content and amplitude distortion through stretch, which both lowers the seismic resolution and hinders lambda-rho - mu-rho ($\lambda\rho$-$\mu\rho$) and amplitude variation with offset and azimuth (AVAz) analysis of the long-offset signal. To mitigate the stretch typically associated with far offsets, we use a matching pursuit based normal moveout correction (MPNMO) to reduce NMO-stretch effect in long offset data. MPNMO corrects the data wavelet-by-wavelet rather than sample-by-sample, thereby avoiding stretch. We apply our technique as part of a residual velocity analysis workflow to a pre-stack time-migrated data volume acquired over the Northern Chicontepec Basin, Mexico. The results show higher resolution both on the pre-stack gathers and on the stacked data volume.

INTRODUCTION

Normal-moveout (NMO) correction applied to common-midpoint (CMP) gathers are one of the most important routine processes applied to seismic data and is a prerequisite for CMP stack and many other procedures (Shatilo and Aminzadeh, 2000). The objective of the NMO correction is to resample a finite-offset trace in a CMP gather to approximate the kinematics of a zero-offset trace. The standard NMO correction causes wavelet stretching which lowers the frequency content of the corrected reflection event at far offset. This stretching will affect all subsequent processing and inversion. For example, unmuted stacked traces exhibit lower frequency content, and therefore have lower resolution and hinder the search for subtle traps (Noah, 1996). NMO stretch also affects AVO analysis by distorting the AVO gradient (Swan 1988, 1997; Ursin and Ekren, 1995).

In flat layers, only the zero-offset traces strictly represent the correct sequence of reflection coefficients (reflectivity function); other finite-offset-corrected traces contain a distortion of the vertical reflectivity function where wavelets have been stretched or even reversed. Buchholtz (1972) was one of the first authors to quantify the artifacts introduced by the NMO correction. Dunkin and Levin (1973) studied the effect of stretch in frequency domain and concluded that usual NMO correction stretches the wavelet in such a way that the spectrum of the NMO-corrected wavelet is a linearly-compressed version of the original spectrum. The amount of compression depends on x, the source-detector separation or “offset” and $V(t_0)$, the velocity model at normal incidence two-way travel time t_0. Barnes (1992) analyzed the correction distortion in instantaneous frequency and instantaneous power domain, and found a time-variant frequency distortion caused by the NMO correction. Miller (1992) studied the impact of muting on the frequency content of stacked images. Owusu and Spencer (1995) analyzed the VSP moveout stretch for a horizontally stratified medium. In Noah's (1996) examples, even minor changes in frequency caused by the NMO correction have a major impact on the interpretation.

As offset increases we often encounter nonhyperbolic moveout in both isotropic and anisotropic media (de Bazelaire, 1988; de Bazelaire and Viallix, 1994; Castle, 1994; Bolshykh, 1956; Dix, 1955; Ursin and Stovas, 2006; Alkhalifah, 1997, 1998; Fomel and Stovas, 2010). Such long-offset data are critical for extending the accuracy of AVO and extracting more rock property information. Dynamic correction of these kinds of wide incidence angle gathers using the hyperbolic equation will introduce not only stretch, but also large time bias which appear on NMO corrected gathers as "hockey sticks". Unfortunately flattening such hockey sticks still results in NMO stretch. In general, severely stretched traces are simply muted out as noise, thus sacrificing the crucial information contained in long offset data. Although estimation of such anisotropy and long offset AVO analysis and prestack impedance inversion is our primary objective, in this paper we focus on eliminating the limitations on such analysis due to wavelet stretch.

Rupert and Chun's (1975) Block-Move-Sum (BMS) method is perhaps the first non-muting solution to address stretch in the NMO correction. The BMS method treats data blocks which are moved as a unit with a single dynamic correction, thus eliminating trace stretching and reducing trace distortion. The drawback to this method is that it introduces wavelet replication and discontinuity between adjacent blocks at far-offset traces where the data blocks overlap. Byun and Nelan (1997) applied a time-varying filter based on a stretch coefficient analysis to the NMO-corrected traces to reduce the loss of high frequencies. Lichman (2000) presented a Phase Moveout method where he substituted the phase spectrum of the minimum-offset-trace for the phase spectra of each finite offset trace, thereby avoiding the usual wavelet stretch. Based on the assumption that all time samples of a digital reflected wavelet at a particular offset have the same normal moveout, Shatilo and Aminzadeh (2000) proposed a Constant Normal Moveout correction strategy which applied a constant moveout for a finite time window of a seismic trace, protecting the corrected traces from stretching and distortion. The most critical factors for successful application of this method are to have an NMO-velocity accuracy better than 1% and an accurate estimate of the window length containing the reflection event. This technique may also produce some corresponding amplitude distortion in the overlapping intervals. Hicks (2001) described a method for removing NMO stretch during stack that uses the Parabolic Radon Transform. He also introduced a new transform, which is a combination of Radon and Spatial Fourier Transforms, to remove stretch from the NMO-corrected CMP gathers. The drawbacks of this approach have been discussed by Trickett (2003).

Brouwer (2002) expanded on the block-move-out technique and suggested an alternative approach based on the correction of tapered blocks of seismic data, followed by a coherence filter (Bruland and Johansen, 1994) to compensate for the specific artifacts thus introduced. Trickett (2003) developed a stretch-free stack process; the method replaces the two steps of NMO correction and stacking with a single-step inversion to zero offset. The main disadvantage of this procedure is that an NMO-corrected CMP gather which is useful for AVO analysis is never formed. Hunt et al. (2003) created pseudo-NMO-corrected gathers, and then identified numerous new prospects using the stretch-free stacking process and AVO analysis.

Hilterman and Van Schuyver (2003) developed a processing and interpretation approach for wide-angle gathers, named Seismic Wide-Angle Processing, to avoid NMO stretch for a specified target horizon. This method first pre-stack migrates blocks of seismic data in the common-offset domain using event-based traveltime rather than sample-based traveltime tables. The travel times are based on a reflection ray-tracing model for each offset. The disadvantage is that only the target horizon is truly flat in the CMP gathers after the processing. Perroud and Tygel (2004) developed a quasi-static NMO shift approach, which can be obtained from the usual dynamic NMO process in a manner similar to a block-moveout process, to avoid stretch as much as possible. This method first requires performing the usual NMO velocity analysis, which estimates t_0 and $V(t_0)$ for each reflection event. They adjust $V(t_0)$ to maintain the local travel time parallelism for each user-identified band-limited reflection event. Unfortunately, this adjustment increases the NMO stretch effect between the identified reflection events. More recently, Masoomzadeh et al. (2010) carefully studied the influence of the data block size to the distortion of the signal and noted that smaller block sizes introduce stretch while larger block sizes generate image discontinuities at the block boundaries. They proposed using iso-moveout curves (lines of equal moveout) in the time-velocity panel to achieve multi-block constant moveout for the selected individual events, leading to a nonstretch correction for the selected events. Nonstretch stacking is achieved by the use of a zigzag velocity function. The main drawbacks are the potential for discontinuities at the window boundaries and the need to estimate appropriate block lengths.

We introduce a strategy which reduces the NMO stretch at far offsets using a matching pursuit wavelet decomposition technology. We start by reviewing the conventional NMO correction equation, using cartoons describing the stretch problem introduced by the conventional correction. Cartoons illustrate the wavelet replication and discontinuity problem that occurs using the block-based correction strategy. Next, we present our non-stretch NMO strategy based on matching pursuit. Finally, we apply our method to a pre-stack time-migrated volume acquired over the Northern Chicontepec Basin, Mexico, and show the improvements on both the corrected gathers and final stacked section.

CONVENTIONAL NMO CORRECTION AND STRETCH

NMO correction transforms seismic traces with arbitrary offset *h* into their zero-offset approximations using the NMO velocity (Shatilo and Aminzadeh, 2000). Assuming a layer cake model for the NMO correction, we obtain the well-known hyperbolic travel time equation (Dix, 1955) as a function of two-way traveltime at zero-offset t_0, offset x, and NMO velocity $V(t_0)$

$$t(x) = \sqrt{t_0^2 + \frac{x^2}{V^2(t_0)}}, \tag{1}$$

where $V(t_0)$ is approximated by the root-mean-square (RMS) velocity for flat-layered media. Using equation 1, the NMO correction time at offset x and zero-offset time t_0 can be written as

$$\Delta t_{NMO} = t(t_0, x) - t_0 = \sqrt{t_0^2 + \frac{x^2}{V^2(t_0)}} - t_0 \,. \tag{2}$$

The conventional correction is implemented on a sample-by-sample basis, using different values of Δt_{NMO} for different samples having a different value of t_0 in the trace. Consequently, samples within one wavelet will suffer different amounts of correction, thereby causing distortion.

Figure 1.1 illustrates the distortion of finite-offset seismic traces for a simple case of two reflection events, R1 and R2. The time interval at zero offset between the two dashed lines is equal to the wavelet duration. Assume we know the correct NMO correction velocity through semblance-based velocity analysis. For a given reflection event, the stretching is exacerbated with increasing offset. The most severe stretching occurs at the intersection of reflection hyperbolae. Beyond such intersection points, the standard NMO correction gives rise to local time-reversal of the signal. These reverse waveforms are particularly harmful to stacking, to high resolution velocity analysis based on flattened events, to AVO analysis, and to noise suppression, as well as other techniques that could benefit from the long-offset data information. Furthermore, sample values must be interpolated to fill in gaps created by the differential stretch.

NONSTRETCH NMO CORRECTION

To avoid stretching for the non-zero offset traces, the moveout correction needs to be constant for all samples that belong to the same reflection wavelet. Variations of the Block-based Moveout Correction provide a means to approximately achieve this goal.

The Block-based moveout NMO correction

The Block-based Moveout correction has two main limitations. First, the block size needs to be a function of the time duration of the reflection events. Second the block boundaries overlap at farther offset if the correction velocity increases with depth, giving rise to the wavelet repetition and discontinuities at the block boundaries. Figure 1.2 illustrates the block-based correction procedure. First, the zero offset trace $d_0(t, x=0)$ is divided into data blocks which may or may not overlap (Figure 1.2a). The block length, τ, and the block centers, t_0, are the two key factors affecting the accuracy of the correction. Rupert and Chun (1975), Shatilo and Aminzadeh (2000) suggested that the block length should be the same as the time duration of the wavelet. In the example here, the t_0 axis is subdivided into adjacent but non-overlapping blocks. The block sizes τ_1 and τ_2 are set to approximate the wavelet duration. Masoomzadeh et al. (2010) modified the NMO velocity to better achieve this goal. Since the NMO velocity usually increases with depth, the travel time of two successive blocks will be compressed at the long offset, which results in overlapping areas for adjacent blocks at far offsets, indicated by the green areas.

Each data block is corrected as a unit from the top to the bottom of the t_0 axis (Figure 1.2b). The samples located in the overlapping area (green) are used twice during the correction resulting in either a repetition or a discontinuity at the block boundaries. The degree of repetition worsens with increasing offset. This repetition harms the stack, creates artificial stacked reflections, and lowers the seismic resolution.

The matching pursuit NMO correction

The NMO-uncorrected traces, $d(t)$, can be regarded as the convolution of the seismic wavelet with the reflectivity series and added noise

$$d(t) = r(t) * w(t) + n(t),$$

(3)

where $r(t)$ is reflectivity series, $w(t)$ is wavelet, and $n(t)$ is noise. This classic theory suggests that the NMO correction can be implemented on a wavelet-by-wavelet basis, with the moveout applied to the reflection events, $r(t)$, rather than to the data samples, $d(t)$. we achieve this goal by using a matching-pursuit wavelet-based decomposition algorithm, commonly used in spectral decomposition algorithms (e.g. Liu and Marfurt, 2005, 2007).

Our input data consist of pre-stack time migrated seismic cube, $d(t, x_n)$, after performing reverse NMO correction using the migration velocity function. Our output data consist of MPNMO-corrected gathers, $d_{MPNMO}(t_0, x_n)$, modeled uncorrected gathers, $d_{mod}(t, x_n)$, and the residual or difference, $d_{res}(t, x_n)$, between the original and modeled uncorrected gathers. The process begins by selecting the NMO correction trajectory curve using either hyperbolic (equation 2) or non-hyperbolic moveout (e.g., Alkhalifah, 1997), as appropriate. Then we build a library of analytic Ricker or Morlet wavelets. Before the MPNMO correction loops begin, residual data are initialized to the input uncorrected data while modeled data and MPNMO-corrected data are initialized to be zero. At each decomposition and correction iteration, j, we apply a constant normal-moveout correction to the residual uncorrected data and stack the corrected gather to form a residual stacked trace. We compute its envelope $e(t_0)$ and pick $t_0^{(k)}$ of the K largest envelope peaks that exceed 50% of the value of the largest envelope, and at each trace n compute moveout times $t_n^{(k)}$ for each offset, x_n. For each residual trace n in the current gather, we also compute its Hilbert Transform to form an analytic trace and calculate the instantaneous frequency, $f_n^{(k)}$ at time locations of $t_n^{(k)}$ and look up a precomputed analytic wavelet, $w[t, f_n^{(k)}]$. Finally, the analytic wavelets are least-squares fit to the analytic residual trace, $d_n^{(j)}$, to obtain the amplitude, $a_n[t^{(k)}]$and phase $\varphi_n[t^{(k)}]$ of the analytic wavelet, $a_n[t^{(k)}]$ and phase

$\varphi_n[t^{(k)}]$ (Liu and Marfurt, 2007). The K scaled wavelets are then subtracted from the previous, $(j$-$1)^{th}$ version of the un-NMO-corrected residual trace

$$d_{res}^{(j)}(t,x_n) = d^{(j-1)}(t,x_n) - \sum_{k=1}^{K} a_n^{(k)} w\left[t - t_n^{(k)}, f^{(k)}\right] \exp\left[i\varphi_n^{(k)}\right], \tag{4}$$

and added to the previous version of the MPNMO-corrected and modeled uncorrected traces

$$d_{MPNMO}^{j}(t_0,x_n) = d_{MPNMO}^{j-1}(t_0,x_n) + \sum_{k=1}^{K} a_n^{(k)} w\left[t - t_0^{(k)}, f^{(k)}\right] \exp\left[i\varphi_n^{(k)}\right], \tag{5}$$

and

$$d_{mod}^{j}(t,x_n) = d_{mod}^{j-1}(t,x_n) + \sum_{k=1}^{K} a_n^{(k)} w\left[t - t_n^{(k)}, f^{(k)}\right] \exp\left[i\varphi_n^{(k)}\right]. \tag{6}$$

The above process is repeated until the total energy of the residual trace falls below a desired threshold (Figure 1.3). At present if crossing events exits in our gathers, we just simply add the scaled wavelets to the time $t_0^{(k)}$ which has the largest stacking power.

In this paper, assume that the MPNMO correction velocity function comes from high resolution velocity analysis, such as the method proposed by the Key and Smithson (1990). To obtain a good-quality corrected gathers, the error of NMO-velocity should be less than 1%, such as that for the method proposed by Shatilo and Aminzadeh (2000). Larger errors will place the wavelets at an incorrect time value of t_0, which will harm subsequent AVO and prestack inversion processes.

To better illustrate the above MPNMO produce, we apply the workflow shown in Figure 1.3 to a synthetic case. The gather is composed of five reflection events. The first and second events cross each other while the fourth and fifth events strongly interfere at far offset (Figure 1.4a). The offsets range from 50 to 3000 m at increments of 50 m. A Ricker wavelet with a 30 Hz dominant frequency is used to generate the synthetic gathers.

Figure 1.4b shows the corrected results using conventional NMO algorithm. Notice that all the events are stretched to some extent at the farthest offset, especially those events located in the blue rectangle. Crossing travel time curves give rise to wavelet repetitions, indicated by red circles in Figure 1.4b. In contrast, the MPNMO algorithm preserves wavelets during the correction (Figure 1.4c). Events within the green rectangle in Figure 1.4c have anonymously low energy compared to other offsets for the second reflection. This artifact is because MPNMO simply move all matched wavelets at crossing time t (labeled with green rectangle in Figure 1.4a) to time t_0 of the first reflection (labeled with the green circle in Figure 1.4c). MPNMO also favors one event over another in decomposition of the interfering fourth and fifth reflection events.

To quantify the improvement of MPNMO over conventional NMO we compare the spectra of the corrected reflection events for five different offsets. For conventional NMO, the spectra of the first and second reflectors shifts to lower frequencies side when the offset exceeds the crossover point (Figures 1.5a and b). The spectral shift to lower frequencies with increasing offset is more continuous for the third but results in severe stretching at far offset (Figure 1.5c). The spectra features of the fourth reflection is erratic as it interferes with the underlying and (at farther offsets) crossing fifth reflector (Figure 1.5d). The fifth reflector is stronger, is less contaminated by interference with the forth reflector, and suffers from less stretch, such that its spectra shift smoothly to lower and lower values with increasing offset (Figure 1.5e).

Figure 1.6 shows that the spectra of these five reflection events is much better preserved using MPNMO, with the spectra for reflectors 1-3 (Figures 1.6a-c) preserved with increasing offset. The spectra of the fourth reflection changes moderately from trace to trace, but exhibits a consistent shape which is a measure of tuning. The spectra of the later-arriving fifth reflection (Figure 1.6e) are similar to that of those Figure 1.5e corrected using conventional NMO. The fifth reflection is not heavily affected by stretching.

A second measure of the fidelity of the correction is to correlate the near-offset trace with all other offsets (Figures 1.7). Note that cross-correlation coefficients for the MPNMO-corrected reflectors (Figure 1.7b) is much better correlated to the zero-offset trace than when using conventional NMO (Figure 1.7a). This waveform consistency is critical to robust AVO and prestack inversion results.

Figure 1.8 illustrates the sensitivity of MPNMO to noise. Figure 1.8a shows the result of adding 15% random noise to the synthetic gathers shown in Figure 1.4a. The noise is sufficiently strong that it is hard to see the second reflection events. The last three traces of the third reflections is also overwhelmed by noise. Figure 1.8b shows that MPNMO successfully corrects the noisy gathers without generating obvious artifacts.

Our final synthetic test is examine the sensitivity of MPNMO to velocity errors. We set the velocity for the third event to be 10% too slow, resulting in an overcorrected, but relatively non-stretched event (Figure 1.9).

APPLICATION

Having calibrated our algorithm on synthetic data, we now apply it to a residual velocity analysis work flow to pre-stack time-migrated CMP gathers in the Northern

Chicontepec Basin, Mexico. The target tight sand Paleocene-Eocene Chicontepec formation lies between $t_0=0.8$ *s* and $t_0=1.2$ *s*. Interpretation of the Chicontepec reservoirs is hampered by geologic complexity, overlying volcanics, and limited resolution (Sarkar, 2011). Figure 1.10a shows a representative CMP gather after reverse NMO correction which "re-squeezes" the migration stretch. The shallow part of the conventional NMO-corrected results suffers severe stretch at far offsets. This stretch can notably lower the seismic resolution in the stack and is harmful to pre-stack inversion. Usually such severely stretched data are muted out (Figure 1.10b) based on a pre-defined muting criteria. In this example we allow wavelets to stretch no more than 150%. Next, we apply the workflow shown in Figure 1.3 to the same CMP gather shown in Figure 1.10a and obtain the MPNMO corrected results (Figure 1.10c), the precomputed wavelet library is Morlet wavelet. Note that MPNMO minimizes the stretch that occurs in the shallow far offset data when compared to the conventionally NMO-corrected data (Figure 1.9d). These corrected far-offset data can be used to improve the stability of AVAz and $\lambda\rho$-$\mu\rho$ inversion.

Figures 1.11a and 1.11b show the amplitude spectra for angle range limited stacked traces to corrected traces shown Figure 1.10b and 1.10c. Red, blue and green lines show the spectra of near-(0-10^o), middle- (10^o-20^o), and far- (20^o-30^o) angle range stacked traces. Due to the increasing stretch with the increase of incidence angle introduced by the conventional NMO correction, the spectral bandwidth (the green line in Figure 1.11a) of the middle- and far-angle stacked traces is distorted and narrower than that of the near-angle stacked traces. In contrast, MPNMO preserves the spectral bandwidth for both middle- and far-angle stacks (Figure 1.11b).

As we did for the synthetic example, we wish to compare the change in waveform as a function of offset or angle. We show the correlation between the near- and mid-angle stacks in Figure 1.12a and the near- and far-angle stacks in Figure 1.12b. Note the overall higher correlation using MPNMO (the red curves) vs. conventional NMO (the blue curves).

After the moveout correction, we stack the corrected CMP traces such as shown in Figures 1.10b and 1.10c to form seismic stacked sections. The traditionally-corrected and stacked section (Figure 1.13a) is acceptable for mapping structure but not stratigraphy (Sarkar, 2011). The interfering events are not well resolved using the conventional correction, such as the pinch-out locate in the red circles in Figures 1.13a and 1.13b. Furthermore the reflection events are more continuous by applying MPNMO correction to the same data set, for example the events that are labeled with the red rectangle in Figures 1.13a and 1.13b. To quantify the improved resolution, we compare the average spectrum features (Figure 1.14) of stacked sections (Figures 1.13). Red, and blue lines are respective the spectra of stacked section from MPNMO correction (Figure 1.13b) and conventional NMO correction (Figure 1.13a). Note that spectra of MPNMO correction show higher ratio of high frequency content compared that of conventional NMO correction.

LIMITATIONS

Like conventional NMO, MPNMO will generate under- (over-) corrected traces if the velocity function is higher (lower) than it should be. Although the cost of MPNMO is significantly greater than both conventional NMO and the published nonstretch NMO correction algorithms, the cost is significantly less than the prestack time migration algorithm used to generate generates the input gathers. Through parallelization and precomputation not only of wavelets, but of moveout functions, the cost becomes acceptable. Crossing events can be approximately handled, but results in amplitude artifacts that could harm subsequent AVO and prestack inversion workflows. Proper partitioning of this energy to the appropriate t_0 location may require integrating concepts associated with high resolution Radon transforms.

CONCLUSIONS

Conventional NMO corrections introduce stretch at offsets that are large relative to reflection depth. This stretch lowers the seismic resolution and distorts the seismic waveform. Block-based correction algorithms avoid stretch but result in wavelet repetition at the block boundary, giving rise to artifacts. Our matching pursuit NMO correction is implemented on a wavelet-by-wavelet basis, reducing stretch and avoiding wavelet repetition. By minimizing stretch, more far-offset data are available for subsequent $\lambda\rho$-$\mu\rho$ and AVAz inversion. The final stacked section has improved band width, which is critical for interpreting thin reservoirs.

ACKNOWLEDGEMENTS

The authors thank PEMEX for permission to use and show their data, and three anonymous referees whose detailed comments and suggestions. We also thank the sponsors of Attribute-Assisted Seismic Processing and Interpretation Consortium (AASPI) for their guidance and financial support.

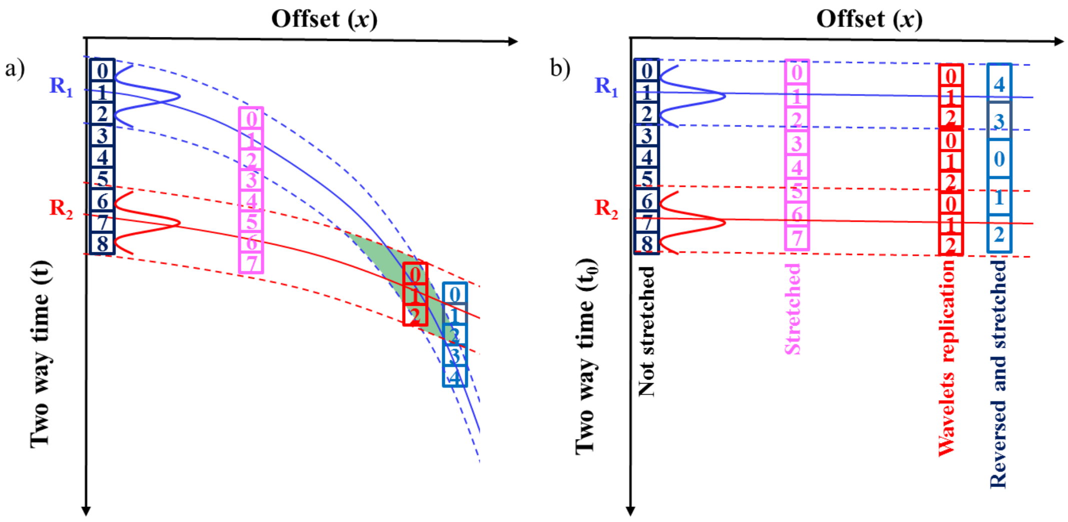

Figure 1.1. Schematic diagrams showing conventional NMO correction for two reflection events (R1 and R2) (a) before (b) after NMO correction. Only the zero-offset samples maintain the same waveform before and after correction; the degree of stretch increases with increasing offset. Shallower events (R_1) undergo greater stretch than deeper events (R_2). The maximum stretch occurs at the crossing point, beyond which the samples' chronological order is reversed.

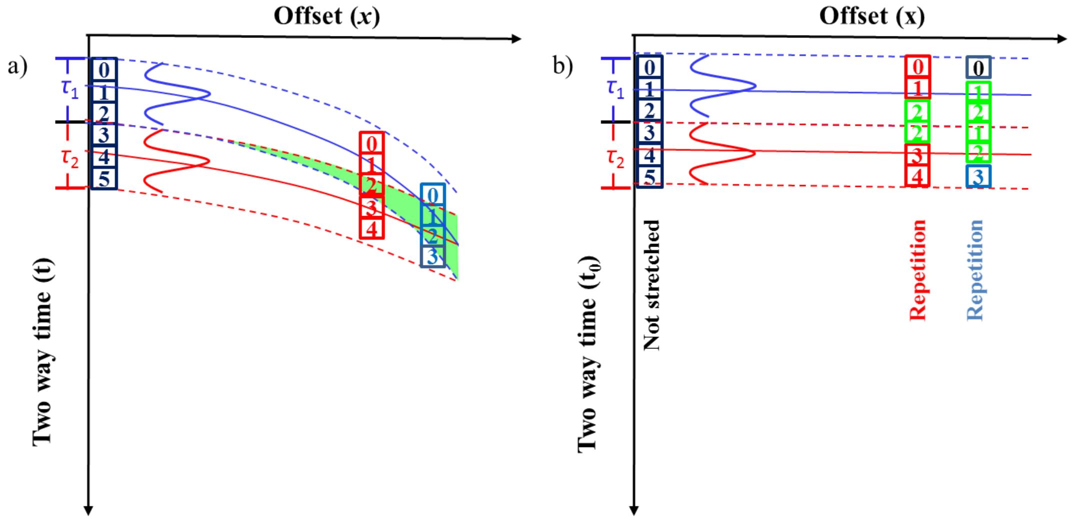

Figure1.2. Cartoons illustrating the implementation and limitation of the block-based NMO correction. (a) The zero-offset time is divided into adjacent data blocks of variable time duration (τ_1 and τ_2). The samples within each block have the same amount of moveout correction. If the NMO correction velocity increases with depth (or zero-offset travel time), the travel time will be compressed with increasing offset, giving rise to overlap (indicated by the green area) at the boundary between the two adjacent blocks. (b) Two interfering reflection events after block-based nonstretch NMO correction. Because of the compression of travel time with depth, the samples indicated by green amplitude values located in the overlapping area of adjacent block will be used twice, giving rise to wavelet repetition and discontinuities.

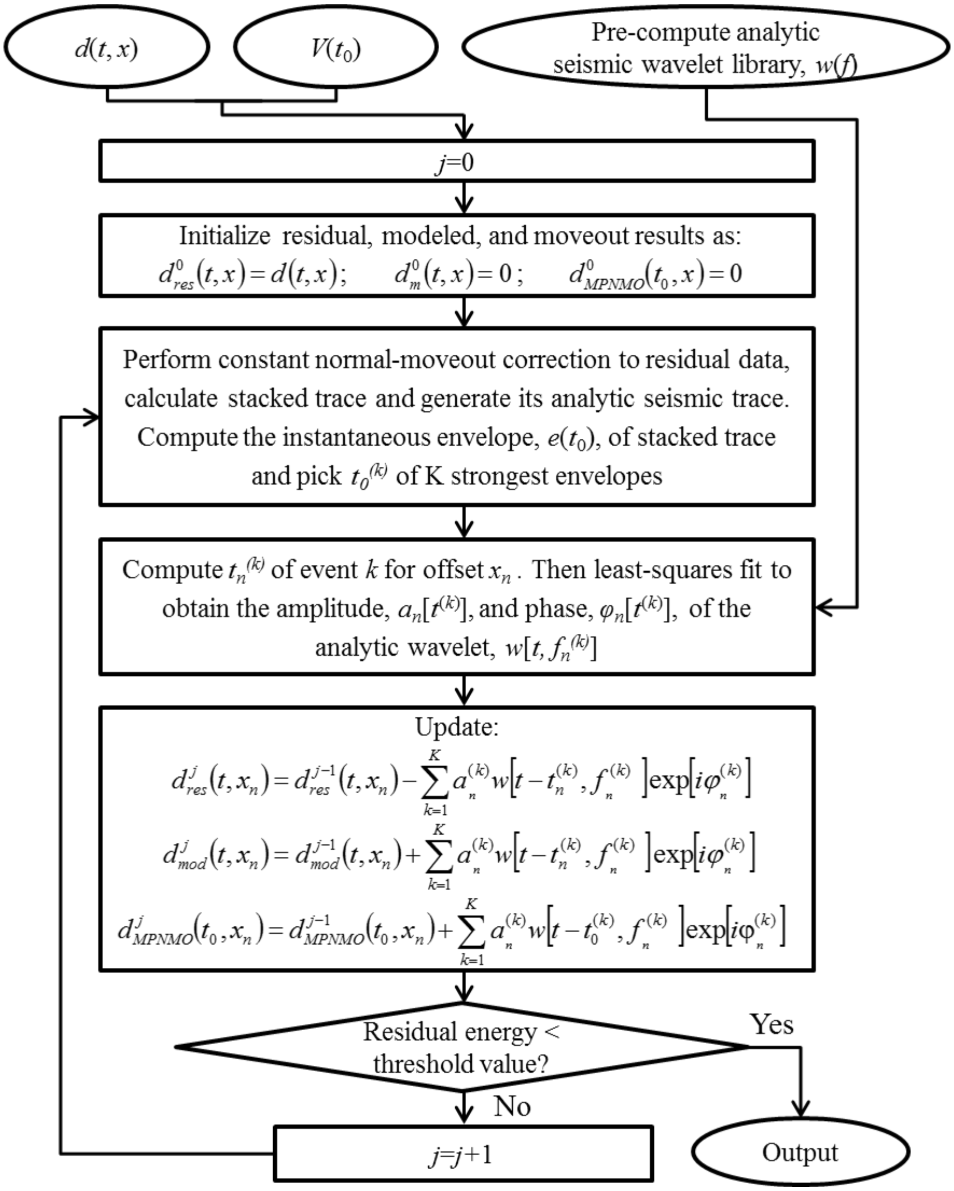

Figure 1.3. Flowchart showing the nonstretch NMO correction workflow based on the matching-pursuit wavelet decomposition technique. Instead of sample-by-sample, the correction is implemented on a wavelet-by-wavelet basis.

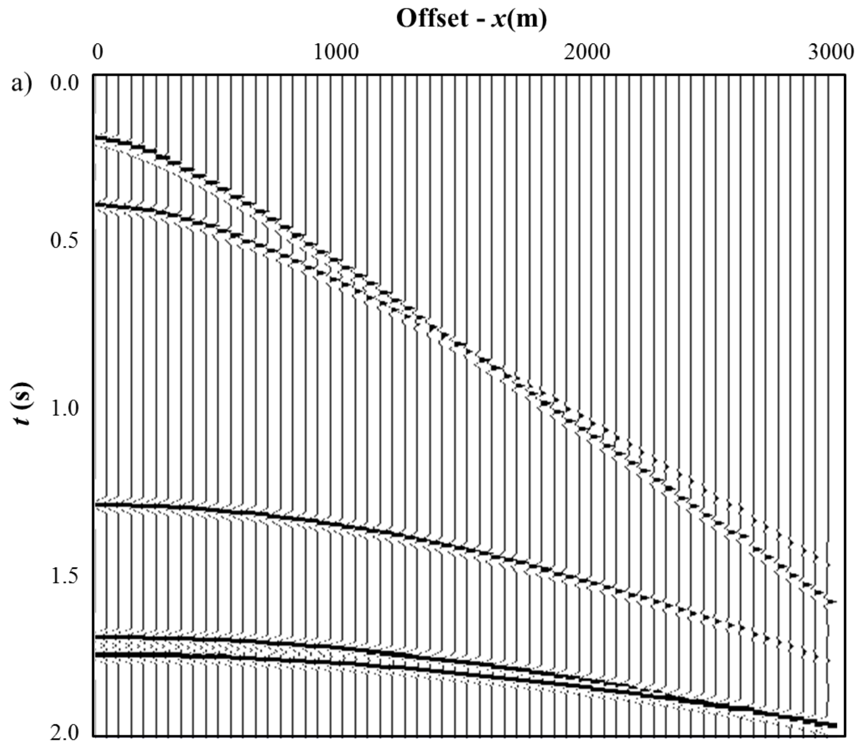
Offset - *x*(m)
0
1000
2000
3000
a)
0.0
0.5
1.0
1.5
2.0
t (s)

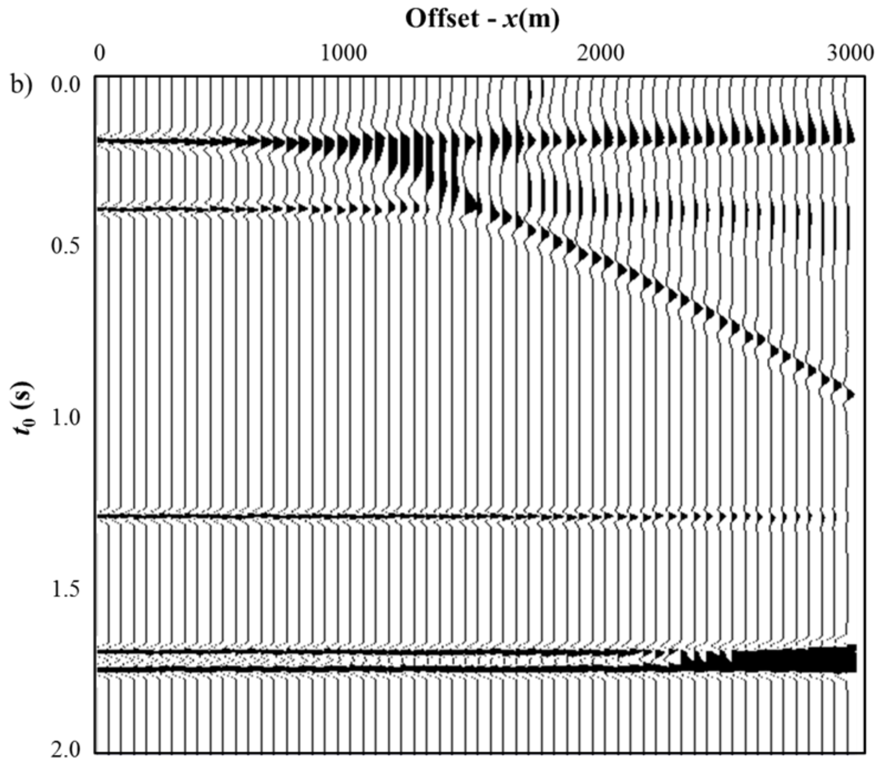
Offset - *x*(m)
0
1000
2000
3000
b)
0.0
0.5
1.0
1.5
2.0
t_0 (s)

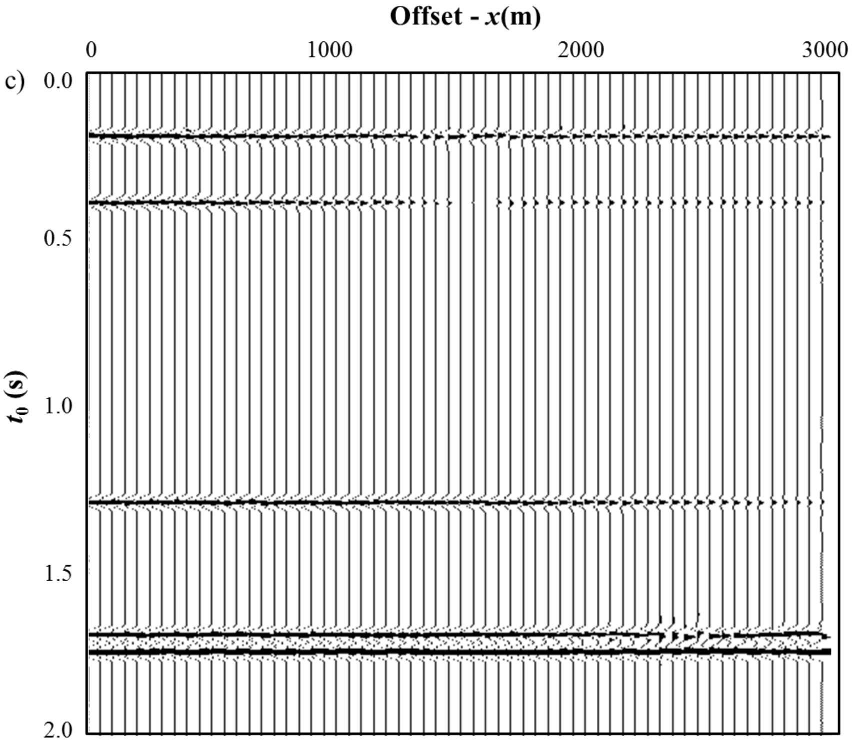

Figure 1.4. (a) A synthetic input gather and corresponding corrected gathers after (b) conventional NMO and (c) MPNMO corrections.

a)

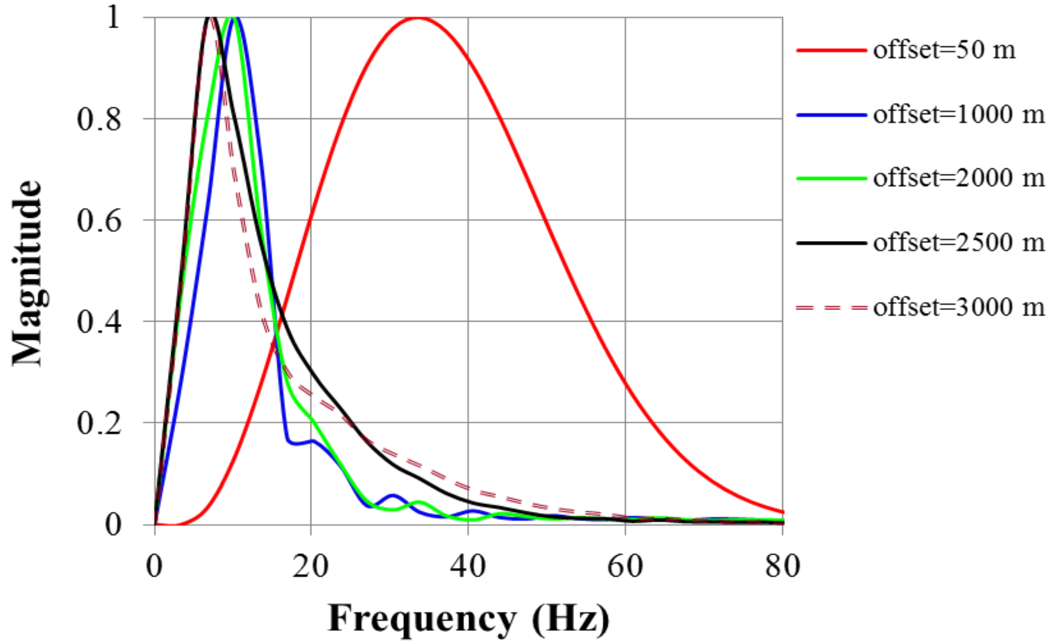
1
0.8
0.6
0.4
0.2
0
Magnitude
0
20
40
60
80
Frequency (Hz)
offset=50 m
offset=1000 m
offset=2000 m
offset=2500 m
offset=3000 m

b)

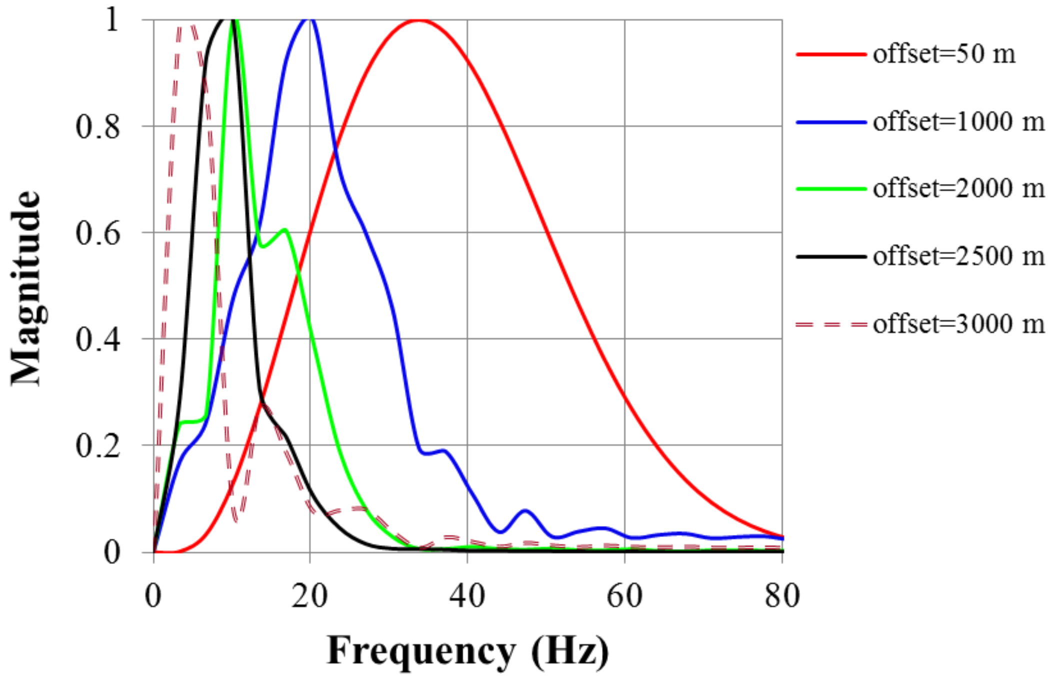
1
0.8
0.6
0.4
0.2
0
Magnitude
0
20
40
60
80
Frequency (Hz)
offset=50 m
offset=1000 m
offset=2000 m
offset=2500 m
offset=3000 m

c)

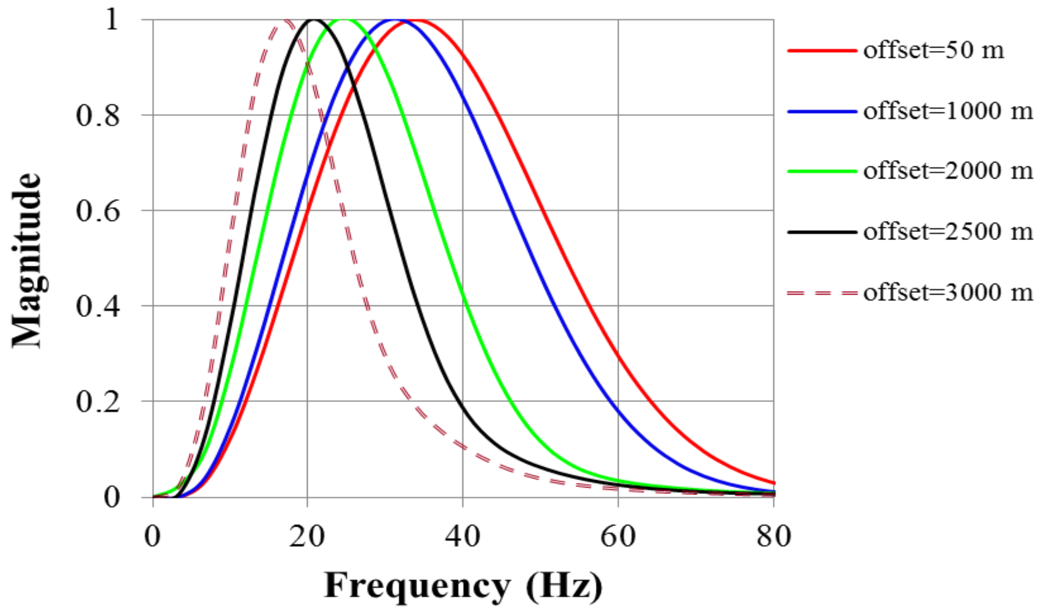
Magnitude
Frequency (Hz)
0
0.2
0.4
0.6
0.8
1
0
20
40
60
80
offset=50 m
offset=1000 m
offset=2000 m
offset=2500 m
offset=3000 m

d)

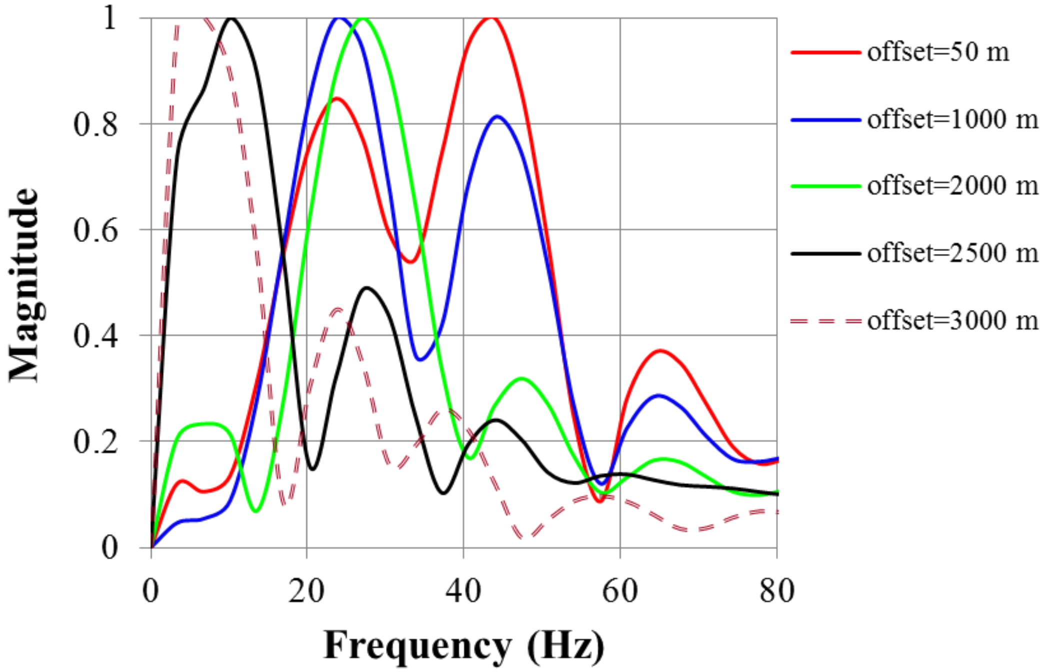
Magnitude
Frequency (Hz)
0
0.2
0.4
0.6
0.8
1
0
20
40
60
80
offset=50 m
offset=1000 m
offset=2000 m
offset=2500 m
offset=3000 m

e)

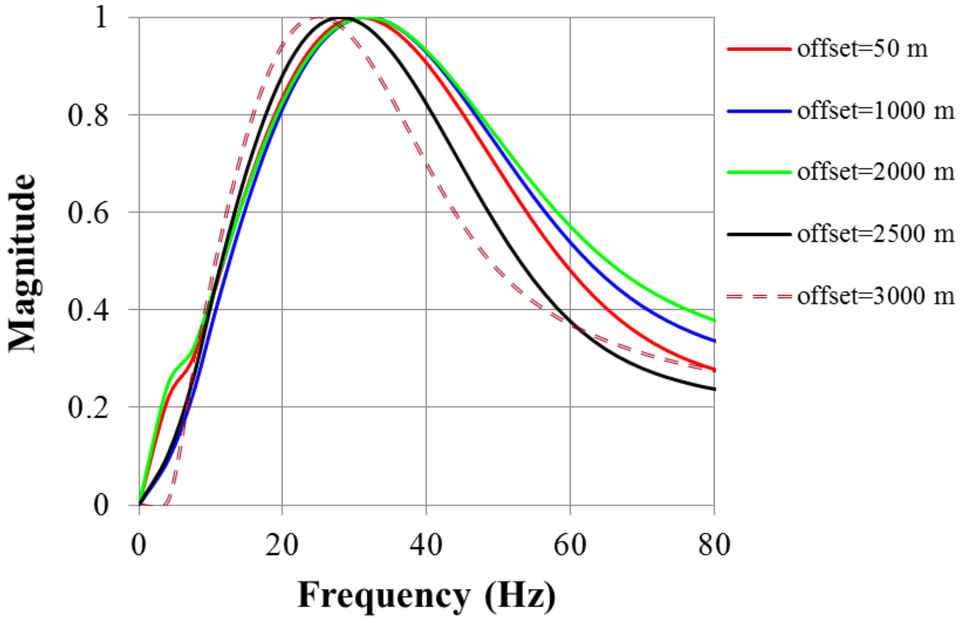

Figure 1.5. Representative spectra as a function of offset for conventional NMO corrected gathers for the (a) first, (b) second, (c) third, (d) fourth, and (e) fifth corrected reflection events shown in Figure 1.4b.

a)

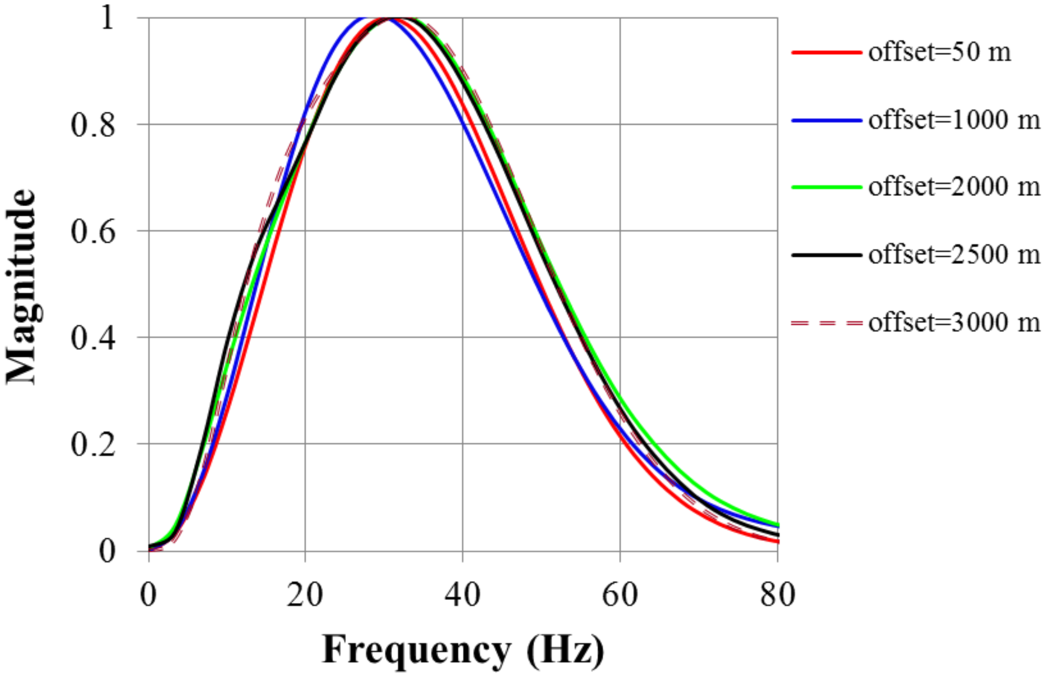
Magnitude
1
0.8
0.6
0.4
0.2
0
0
20
40
60
80
Frequency (Hz)
offset=50 m
offset=1000 m
offset=2000 m
offset=2500 m
offset=3000 m

b)

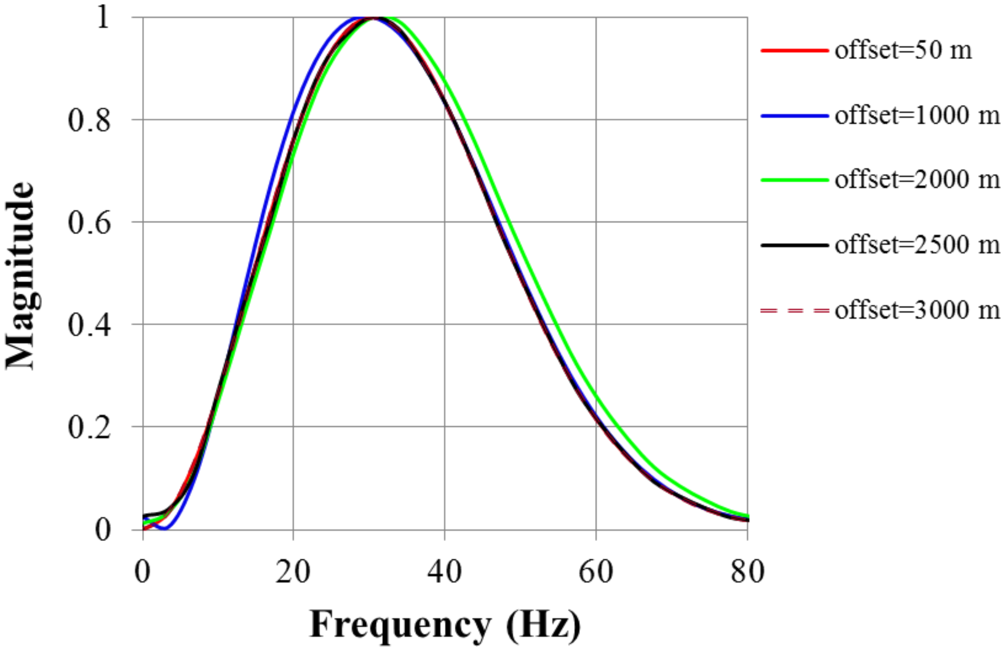
Magnitude
1
0.8
0.6
0.4
0.2
0
0
20
40
60
80
Frequency (Hz)
offset=50 m
offset=1000 m
offset=2000 m
offset=2500 m
offset=3000 m

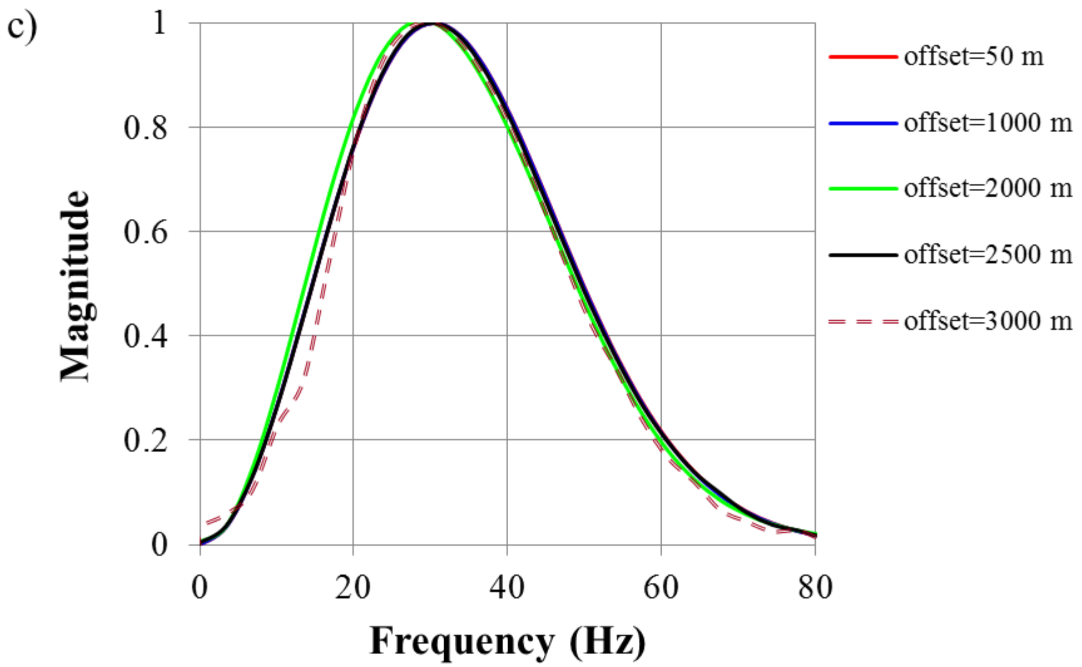
c)
Magnitude
1
0.8
0.6
0.4
0.2
0
0
20
40
60
80
Frequency (Hz)
offset=50 m
offset=1000 m
offset=2000 m
offset=2500 m
offset=3000 m

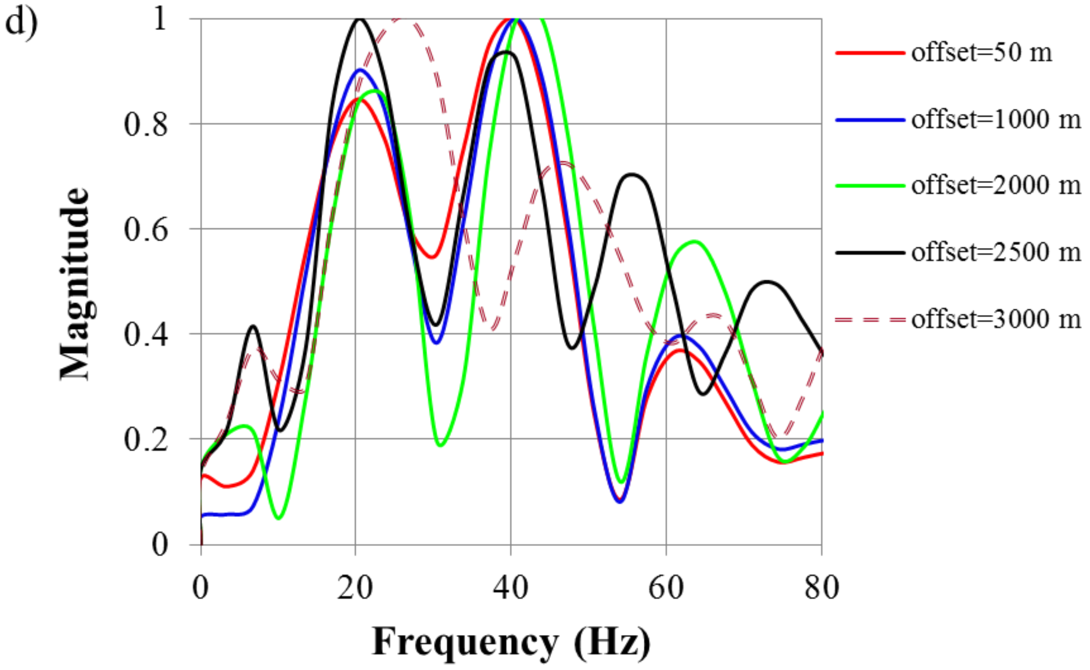
d)
Magnitude
1
0.8
0.6
0.4
0.2
0
0
20
40
60
80
Frequency (Hz)
offset=50 m
offset=1000 m
offset=2000 m
offset=2500 m
offset=3000 m

e)

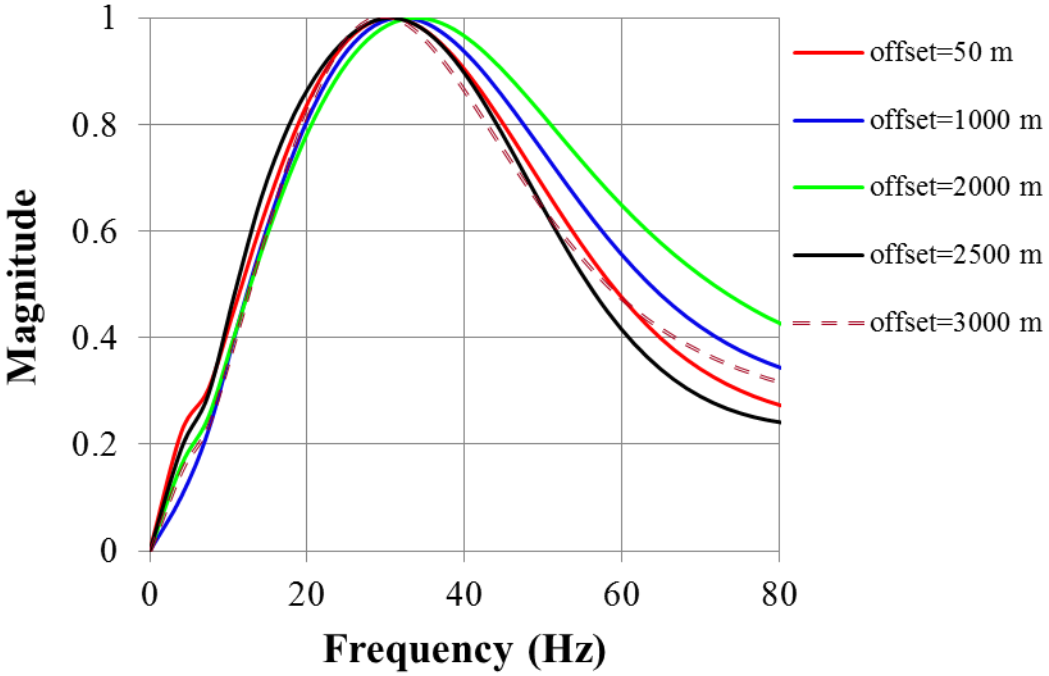

Figure 1.6. Representative spectra as a function of offset for MPMO corrected gathers for the (a) first, (b) second, (c) third, (d) fourth, and (e) fifth corrected reflection events shown in Figure 1.4b.

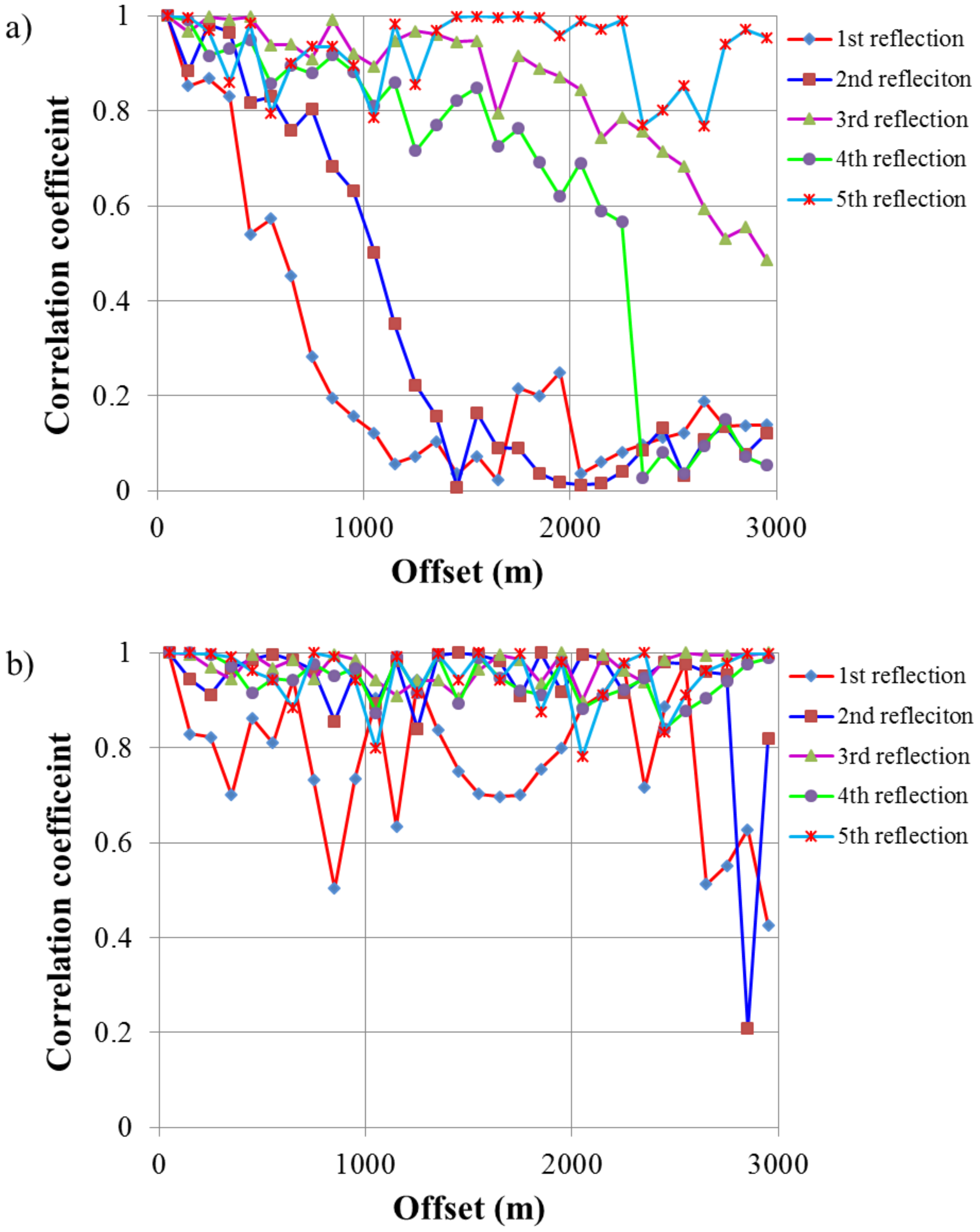

Figure 1.7. Cross-correlation coefficients between the zero-offset trace and finite-offset corrected using (a) conventional NMO and (b) MPNMO applied to the gather shown Figure 1.4a.

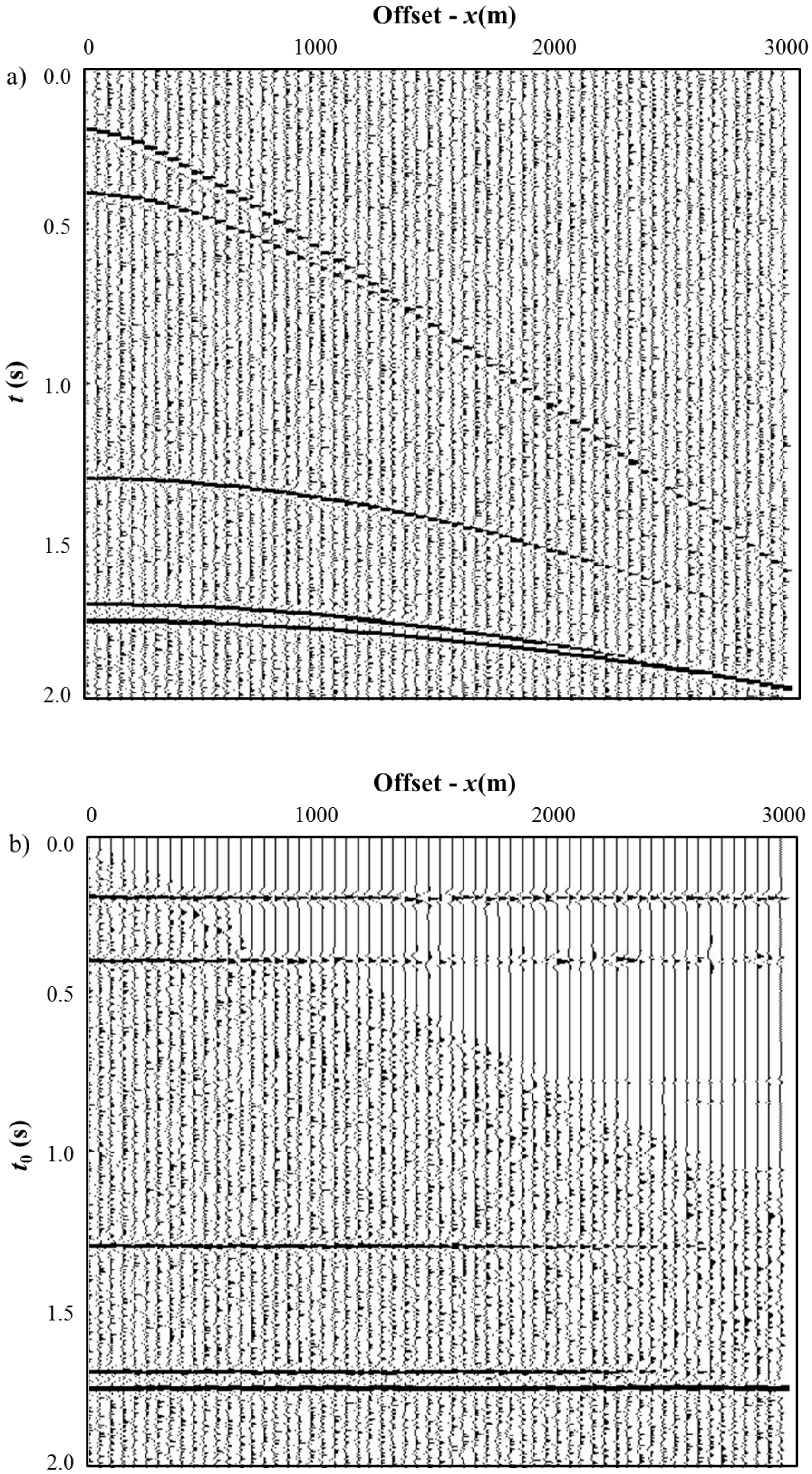

Figure 1.8. A synthetic gather with random noise (a) before and (b) after MPNMO correction.

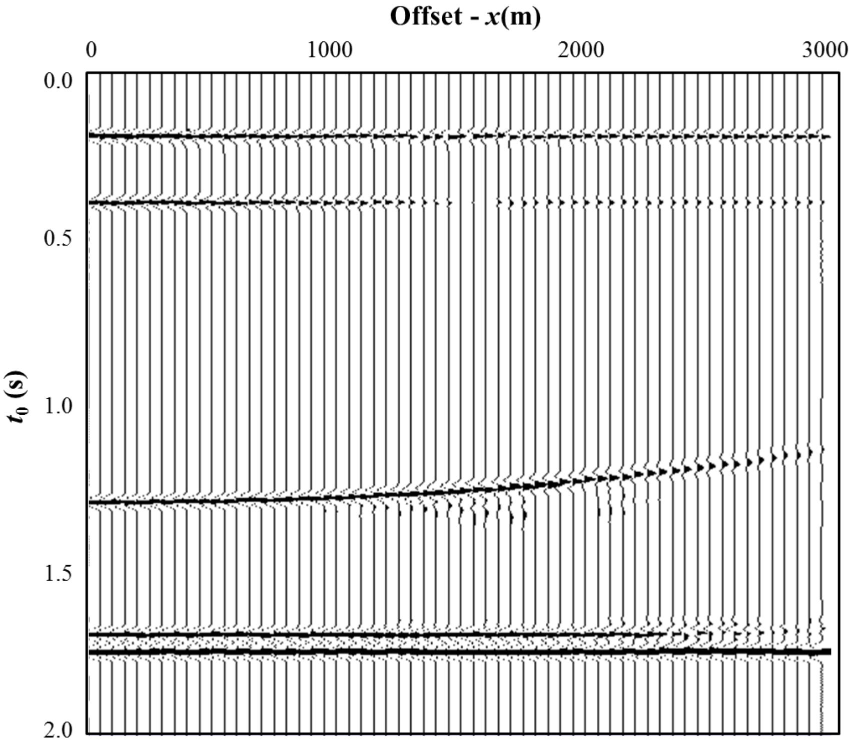

Figure 1.9. Although MPNMO minimizes stretch effects, it does not correct for errors in velocity. Here the gather shown in Figure 1.4a is corrected with MPNMO using a velocity that was 10% too slow, thereby overcorrecting the data.


a)
Offset - *x*(m)
0
1000
2000
3000
t (s)
0.5
1.0
1.5

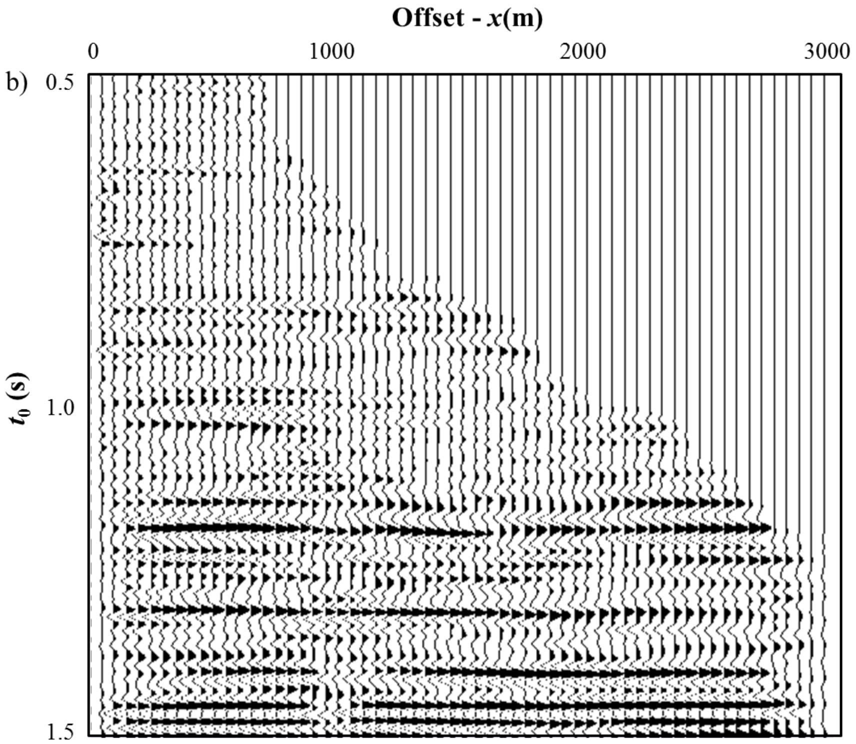
b)
Offset - *x*(m)
0
1000
2000
3000
t_0 (s)
0.5
1.0
1.5

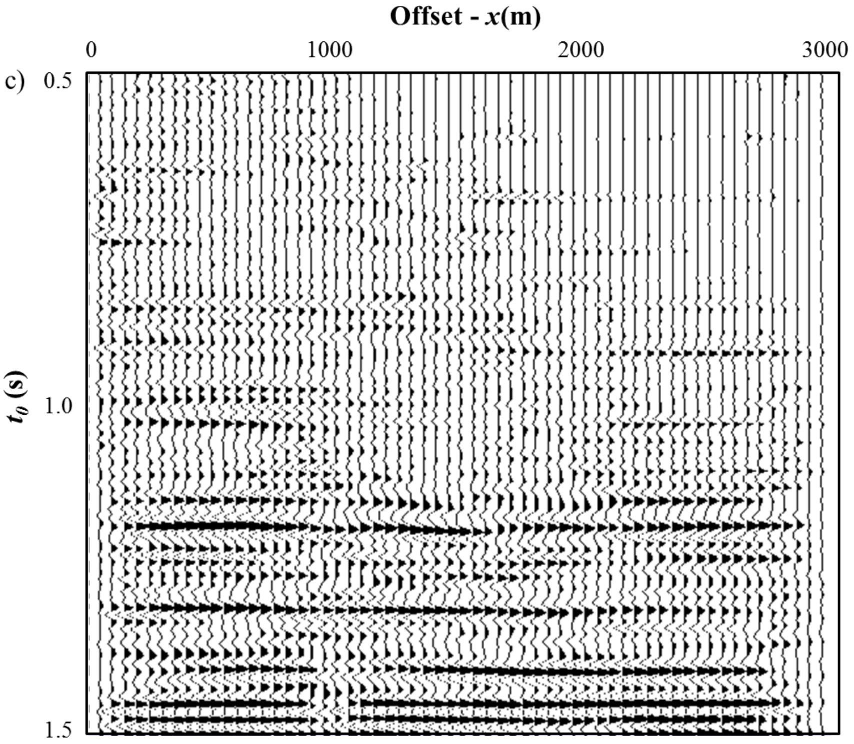

Figure 1.10. Applying (b) conventional NMO and (c) MPNMO correction to a representative pre-stack time migrated gather (a) from the Chicontepec Basin, Mexico (CMP no. 1 in Figure 1.13).

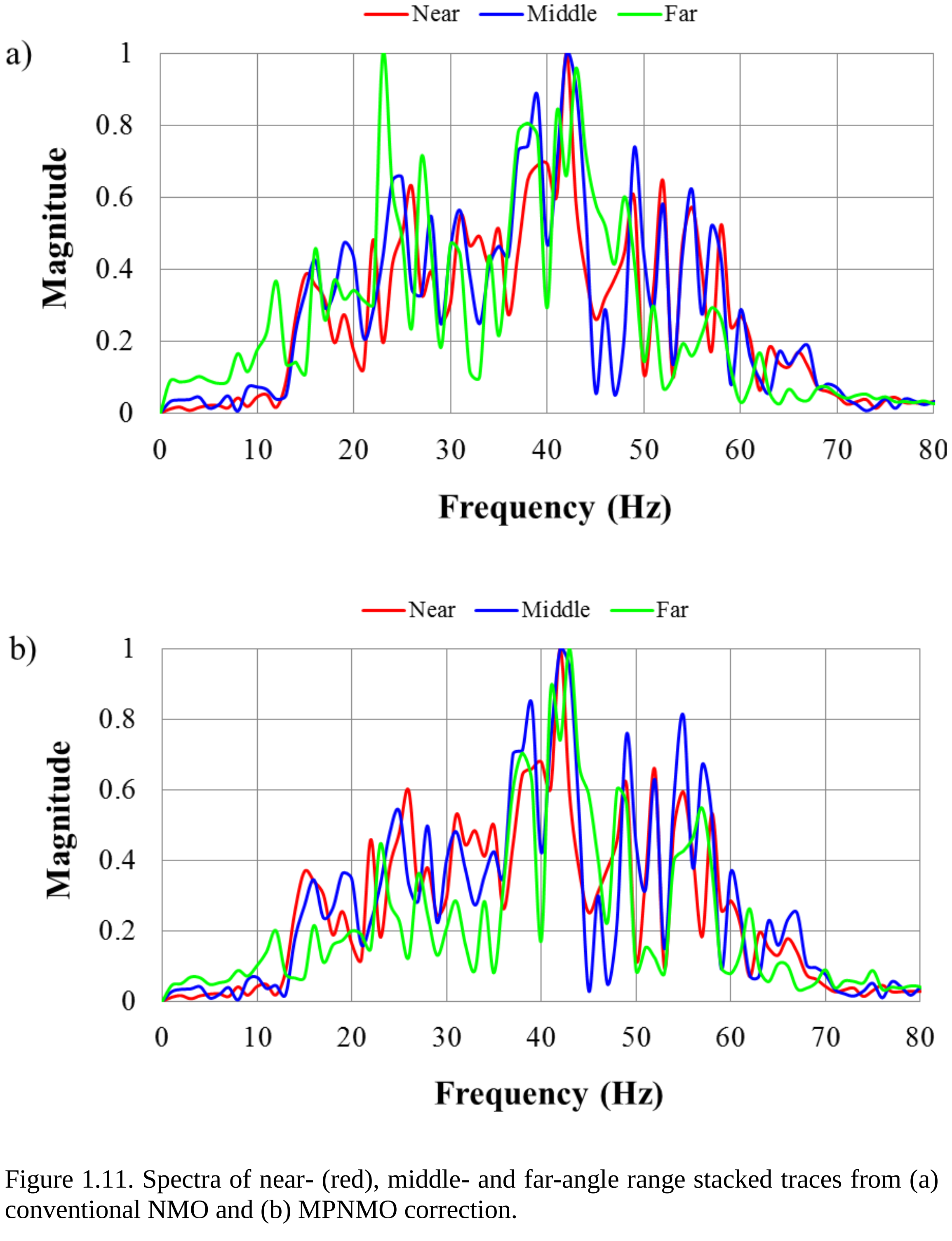

Figure 1.11. Spectra of near- (red), middle- and far-angle range stacked traces from (a) conventional NMO and (b) MPNMO correction.

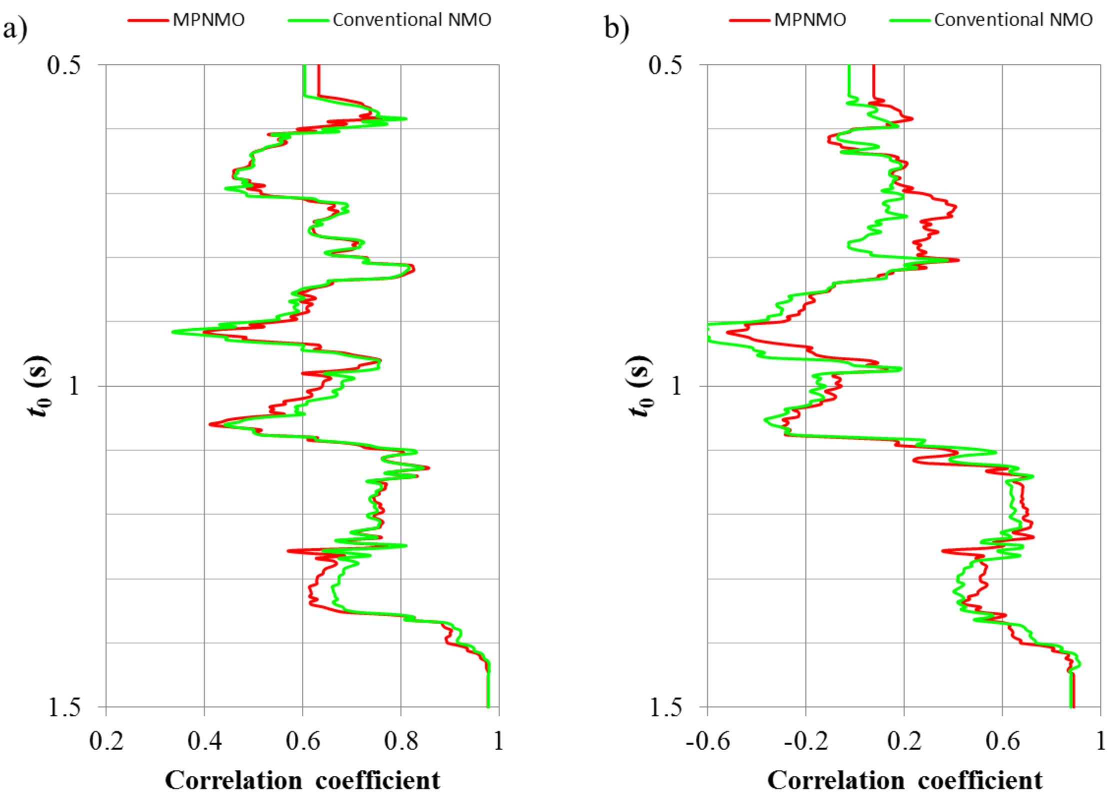

Figure 1.12. Correlation coefficients between (a) the near- and mid-angle stacks and (b) the near- and far-angle stacks using conventional NMO (in blue) and MPNMO (in red).

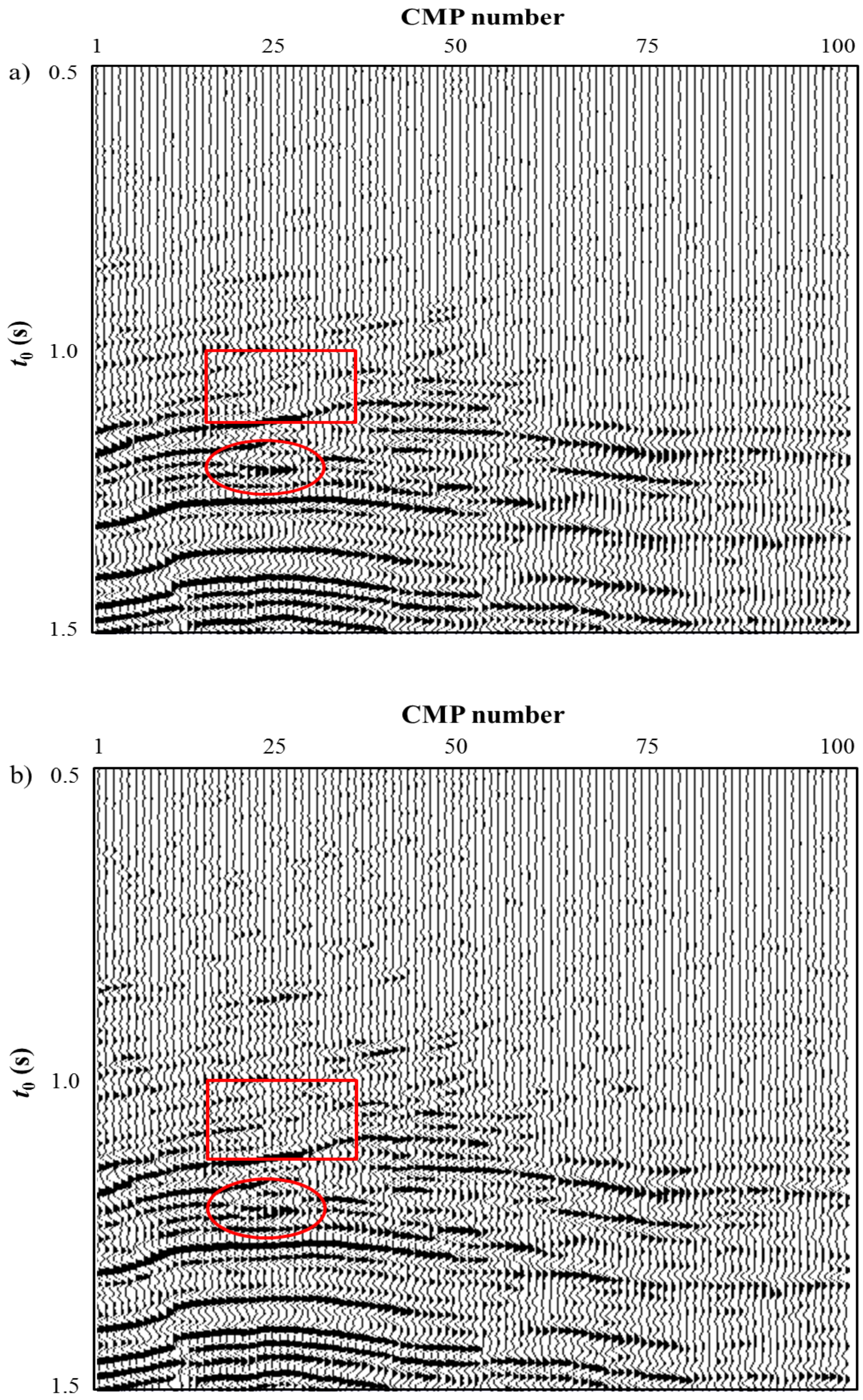

Figure 1.13. Stacked sections after (a) conventional NMO correction with 150% muting criteria and (b) MPNMO correction algorithm shown in Figure 1.3. The target Paleocene-Eocene Chicontepec formation lies between *t*=0.8*s* and *t*=1.2*s* (Sarkar, 2011). Note the improved resolution (such as the events marked by the red circle) and continuity (such as the event marked by the red rectangle) of the reflection events using MPNMO correction method.

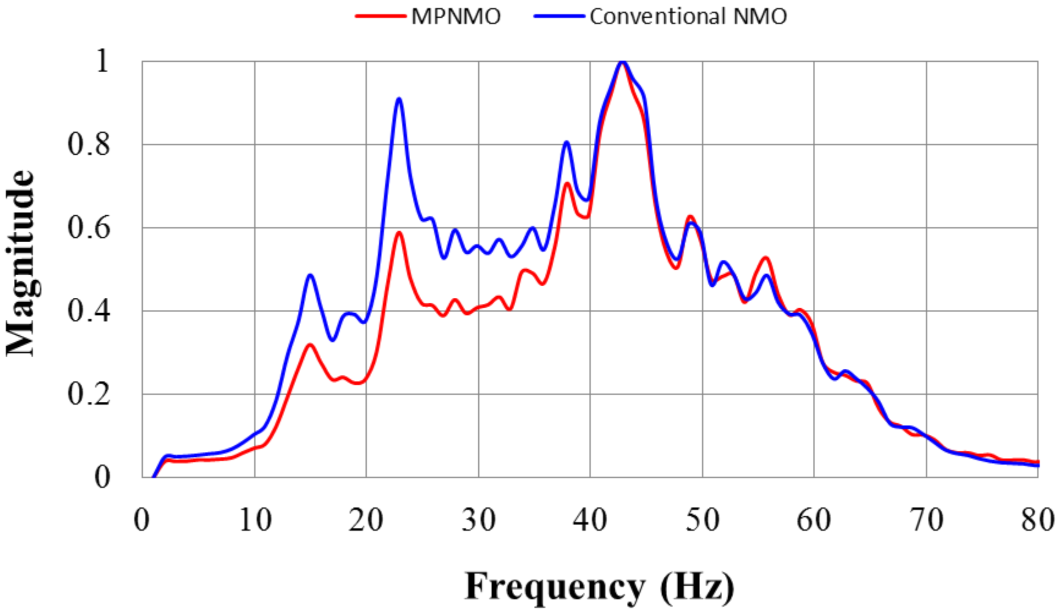

Figure 1.14. Average amplitude spectra for stacked sections shown in Figure 1.13 corresponding to the conventional NMO corrected gathers in blue, and MPNMO-corrected gathers in red.

REFERENCES

Alkhalifah, T., 1997, Seismic data processing in vertically inhomogeneous TI media: Geophysics, **62**, 662-675.

Alkhalifah, T., 1998, Acoustic approximations for processing in transversely isotropic media: Geophysics, **63**, 623-631.

Barnes, A. E., 1992, Another look at NMO stretch: Geophysics, **57**, 749-751.

Bolshykh, S. F., 1956, About an approximate representation of the reflected wave traveltime curve in the case of a multi-layered medium: Applied Geophysics (in Russian), **15**, 3-15.

Brouwer, J. H., 2002, Improved NMO correction with a specific application to shallow seismic data: Geophysical Prospecting, **50**, 225-237.

Bruland, L., and T.A. Johansen, 1994, Resolving interfering events through cyclic sampling and median filtering: First Break **12**, 445-452.

Buchholtz, H., 1972, A note on signal distortion due to dynamic (NMO) corrections: Geophysical Prospecting, **20**, 395-402.

Byun, B. S., and E. S. Nelan, 1997, Method and system for correcting seismic traces for normal move-out stretch effects: U.S. Patent 5, 684, 754.

Castle, R. J., 1994, A theory of normal moveout: Geophysics, **59**, 983-999.

de Bazelaire, E., 1988, Normal moveout revisited: Inhomogeneous media and curved interfaces: Geophysics, **53**, 143-157.

de Bazelaire, E., and J. R. Viallix, 1994, Normal moveout in focus: Geophysical Prospecting, **42**, 477-499.

Deregowski, S. M., 1990, Common-offset migrations and velocity analysis: First Break, **8**, 225-234.

Dix, C. H., 1955, Seismic velocities from surface measurements: Geophysics, **20**, 68-86.

Dunkin, J. W., and F.K. Levin, 1973, Effect of normal moveout on a seismic pulse: Geophysics, **38**, 635-642.

Fomel, S., and A. Stovas, 2010, Generalized nonhyperbolic moveout approximation: Geophysics, **75**, U9-U18.

Hicks, G. J., 2001, Removing NMO stretch using the Radon and Fourier-Radon transforms: 63rd Annual International Meeting, EAGE, Extended Abstracts, A-18.

Hilterman, F., and C. Van Schuyver, 2003, Seismic wide-angle processing to avoid NMO stretch: 73rd Annual International Meeting, SEG, Expanded Abstracts, 215-218.

Hunt, L., S. Trickett, D. Levesque, P. McKenny, B. Link, and S. Jamieson, 2003, The effect of stretch free stacking on a clastic exploration play in Alberta, Canada: 73rd Annual International Meeting, SEG, Expanded Abstracts, 321-324.

Key, S., and S. B. Smithson, 1990, New approach to seismic-reflection event detection and velocity determination: Geophysics, **55**, 1057-1069.

Lichman, E., 2000, Automated phase-based moveout correction: 69th Annual International Meeting, SEG, Expanded Abstracts, 1150-1153.

Liu, J., and K. J. Marfurt, 2005, Matching pursuit decomposition using Morlet wavelet: 75th Annual International Meeting, SEG, Expanded Abstracts, 786–789.

Liu, J., and K. J. Marfurt, 2007, Instantaneous spectral attributes to detect channels: Geophysics, **72**, P23–P31.

Masoomzadeh, H., P. J. Barton, and S. C. Singh, 2010, Nonstretch moveout correction of long-offset multichannel seismic data for subbasalt imaging: Example from the North Atlantic: Geophysics, **75**, R83-R91.

Miller, R. D., 1992, Normal moveout stretch mute on shallow-reflection data: Geophysics, **57**, 1502–1507.

Noah, J. T., 1996, NMO stretch and subtle traps: The Leading Edge, **15**, 345-347.

Owusu, J. C., and T. W. Spencer, 1995, VSP normal moveout stretch: Geophysics, **60**, 1579-1582.

Perroud, H., and M. Tygel, 2004, Nonstretch NMO: Geophysics, **69**, 599-607.

Rupert, G. B., and J. H. Chun, 1975, The block move sum normal moveout correction: Geophysics, **40**, 17-24.

Shatilo, A., and F. Aminzadeh, 2000, Constant normal-moveout (CNMO) correction: A technique and test results: Geophysical Prospecting, **48**, 473-488.

Sarkar, S., 2011, Depositional history and reservoir characteristics of structurally confined for deep turbidites, Northern Chicontepec Basin, Mexico: Ph.D. thesis, The University of Oklahoma

Swan, H.W., 1988, Amplitude versus offset analysis in a finely layered media: 58th Annual International meeting, SEG, Expanded Abstracts, 1195-1198.

Swan, H.W., 1997, Removal of offset-dependent tuning in AVO analysis: 67th Annual International meeting, SEG, Expanded Abstracts, 175-178.

Trickett, S., 2003, Stretch-free stacking: 73rd Annual International Meeting, SEG, Expanded Abstracts, 2008-2011.

Ursin, B., and B. O. Ekren, 1995, Robust AVO analysis: Geophysics, **60**, 317-326.

Ursin, B., and A. Stovas, 2006, Traveltime approximations for a layered transversely isotropic medium: Geophysics, **71**, D23-D33.

Chapter 2: Horizon-based semi-automated nonhyperbolic velocity analysis

Bo Zhang[1], Tao Zhao[1], Jie Qi[1] and Kurt J. Marfurt[1],

[1]The University of Oklahoma, ConocoPhillips School of Geology and Geophysics,

This paper was accepted by SEG journal Geophysics in 2014.

Title: Horizon-based semi-automated nonhyperbolic velocity analysis

ABSTRACT

With higher capacity recording systems, long-offset surveys are becoming common in seismic exploration plays. Long offsets provide leverage against multiples, have greater sensitivity to anisotropy, and are key to accurate inversion for shear impedance and density. There are two main issues associate with preserving the data fidelity contained in the far offsets 1) nonhyperbolic velocity analysis and 2) mitigating the migration/NMO stretch. Current nonhyperbolic velocity analysis workflows first estimate moveout velocity V_{nmo} based on the offset-limited gathers, then pick an effective anellipticity η_{eff} using the full-offset gathers. Unfortunately estimating V_{nmo} at small aperture may be inaccurate, with picking errors in V_{nmo} introducing errors in the subsequent analysis of effective anellipticity. We propose an automated algorithm to simultaneously estimate the nonhyperbolic parameters. Instead of directly seeking an effective stacking model, the algorithm finds an interval model that gives the most powerful stack. The searching procedure for the best interval model is conducted using a direct, global optimization algorithm called differential evolutionary (DE). Next we apply an anti-stretch workflow to minimize the stretch at far offset after obtaining the optimal effective model. The automated velocity analysis and anti-stretch workflow are tested on the data volume acquired over the Fort Worth Basin, USA. The results show noticeable improvement both on the pre-stack gathers and on the stacked data volume.

INTRODUCTION

Velocity analysis applied on common-midpoint (CMP) gathers is usually based on computing the coherence of moveout corrected gathers using zero-offset times and a suite of trial stacking velocities. Velocity analysis is one of the most important and interpreter-time consuming tasks in seismic processing. The accuracy of velocity analysis depends on 1) the resolution of velocity spectra, 2) The accuracy of the selected equation in approximating the kinematic behaviors of the reflection events, and 3) the skill and experience of data processor.

Semblance is perhaps the most commonly used coherency measurements for velocity spectra (Taner and Koehler, 1996; Neidell and Taner, 1971). Swan (2001) is one of the first researchers to develop high resolution velocity spectra algorithm that accounts for amplitude variations with offset. Larner and Celis (2007) improved both the resolution and reliability of velocity spectra by just using selected subsets of crosscorrelation rather than all possible ones in the gathers. To minimize the effect of AVO phenomenon that exists in prestack gathers, Fomel (2009) proposed a generalized “AB semblance” that is particularly attractive for velocity analysis of class II AVO anomalies where the polarity of the reflections changes. To further improve the resolution of semblance-based velocity spectra, Luo and Hale (2010) introduce a weighting function that slightly increases the cost of calculation but are still comparable to that of conventional semblance. Biondi and Kostov (1989) introduced high-resolution velocity spectra by using an eigenstructure method rather than semblance. Key and Smithson (1990) also used eigenstructure analysis, which is based on covariance measurement of NMO-corrected traces, to get higher velocity spectrum and locate the reflection events. Kirlin (1992) deduced the relationship between semblance and eigenstructure velocity estimators. The eigenstructure-based estimators have higher resolution but greater computation cost. Sacchi (1998) further improved the resolution of velocity spectra by integrating a bootstrap method in the covariance computation. Unfortunately his computational cost is also very expensive.

The approximated kinematic behaviors of the moveout correction for P-wave reflection traveltime is defined by either hyperbolic (Dix, 1955) or nonhyperbolic equations (Thomsen, 1986; Alkhalifah and Tsvankin, 1995; Alkhalifah, 1997). The hyperbolic traveltime approximation equation is based on the assumption of homogeneous isotropic or elliptically anisotropic layer-cake model and need to be restricted to small aperture (the offset-to-depth ratio $2h/z \leq 1.0$). As offset increases we often encounter nonhyperbolic moveout in both isotropic (Bolshykh, 1956, Taner and Koehler, 1969; de Bazelaire, 1988) and anisotropic media (Alkhalifah, 1997; Fomel and Stovas, 2010; Alkhalifah, 2011). Ignoring the anisotropy in prestack migration will fail to properly correct for the moveout of dipping reflectors and injects errors for the reflectors. The most common nonhyperbolic equations are fourth-order approximations expressed using three parameters 1) the two-way zero-offset travel time t_0, 2) the short-spread NMO velocity V_{nmo}, and 3) effective anellipticity η_{eff}. The effective anellipticity combines the effects of long offset ray bending (the "Snell" effect) as well as intrinsic anisotropy. Alkhalifah (1997) introduced what is now the most commonly used two-step approach for nonhyperbolic velocity analysis, where one first estimates the NMO velocity on offset-limited truncated gather using hyperbolic NMO correction, followed by estimation of effective anellipticity using the full-offset gathers. Unfortunately, small aperture NMO velocity analysis may be inaccurate. Picking errors in V_{nmo} introduce errors into the subsequent analysis of effective anellipticity.

Conventional velocity analysis (CVA) requires manually picking the peaks of the semblance panel. Such picking is tedious, and a great deal of effort has been invested in attempting to accelerate this process. CVA also requires a great deal of skill and experience. There is no guarantee that the picked RMS velocity represents the true earth model with erroneous picks (for example of multiple reflections) leading to infeasible interval velocities. Toldi (1989) proposed one of the first velocity analysis algorithms that avoids manual picking. Instead of directly searching the RMS velocity, his algorithm examines suite of possible interval velocity models, calculates the corresponding RMS velocity using Dix equation, and then estimates the corresponding stacking power. The final product is an interval velocity model that when converted to a moveout curve corresponds to the most powerful stacking. His least-squares optimization algorithm is parameterized by layers of equal time thickness without explicitly considering the location of reflection events. Building on the concept of measuring the degree of reflections flattening using an l_1-norm in the τ-p domain, Calderón-Macías et al. (1998) performed automatic velocity analysis to recover the interval velocity model. Van der Baan and Kendall (2002) also inverted the model in the τ-p domain, and concluded that there exists a family of kinematically equivalent models that exhibit identical moveout curves. Siliqi et al. (2003) obtained dense model parameters by simultaneously picking velocity and anellipticity. Abbad et al. (2009) proposed two-step automatic nonhyperbolic velocity analysis using a normalized bootstrapped differential semblance (BDS). They first performed hyperbolic velocity analysis on truncated small-offset data at coarse space to identify events, and then implemented dense nonhyperbolic velocity analysis about the identified events. The BDS estimator has higher resolution than differential semblance (DS), but can significantly increase the computation cost. Choi et al. (2010) developed an efficient automatic velocity analysis algorithm by using BDS and Monte Carlo inversion.

Most velocity analysis is done in a processing shop by professional processors. These velocities are then used to prestack migrate the data. Our goal in this paper is to present a workflow that improves upon these images, giving a residual velocity analysis.

To use the critical information contained in the long offset data, we need not only to flatten the reflections at far offset using nonhyperbolic travel time equation but also minimize the stretch typically associated with large aperture. In this paper, we first extend Toldi's (1989) method by adding interval anellipticity as one of the parameters for the model to perform automatic nonhyperbolic analysis based on user defined horizons. We then follow Zhang et al., (2013) to minimize the stretch at far offset. We apply our technique as a residual velocity analysis workflow to a pre-stack time-migrated data volume acquired over the Fort Worth Basin, USA, and show the improvements on both the prestack corrected gathers and final stacked section.

AUTOMATED NONHYPERBOLIC VELOCITY ANALYSIS

There are mainly two issues in performing automatic residual velocity analysis. The first issue is to select a proper travel time equation. The second issue is to define the objective function as a function of proposed model. In this paper we employ the well-known nonhyperbolic trajectory (Alkhalifah, 1997). Our model parameters consist of interval velocity v_{nmo} and anellipticity $\eta_{int}(\tau)$. The objective is to find an interval model that gives the maximum stacking power (semblance). Our optimization engine is a direct, global searching called differential evolution (DE) algorithm.

Travel time equations

The shifted hyperbola (de Bazelaire, 1988; Castle, 1994) and Alkhalifah-Tsvankin (Alkhalifah and Tsvankin, 1995; Alkhalifah, 1997) approximation are among the most commonly used traveltime equations for nonhyperbolic velocity analysis. Since we wish to perform residual velocity analysis on anisotropic shale reservoirs, we employ Alkhalifah-Tsvankin approximation

$$t^2(x) = t_0^2 + \frac{x^2}{V_{nmo}^2} - \frac{2\eta_{eff} x^4}{V_{nmo}^2\left[t_0^2 V_{nmo}^2 + (1+2\eta_{eff})x^2\right]}, \tag{1}$$

where t_0 is the two-way traveltime at zero-offset, x is offset, $V_{\mathrm{nmo}}(t_0)$ is the NMO velocity at small apertures, and η_{eff} is effective anellipticity.

For VTI (vertical transverse isotropy) media, Alkhalifah (1997) deduced the relationship between effective and interval values using Dix forward equations

$$V_{nmo}^2(t_0) = \frac{1}{t_0}\int_0^{t_0} v_{nmo}^2(\tau)\, d\tau, \tag{2a}$$

and

$$\eta_{eff}(t_0) = \frac{1}{8}\left\{\frac{1}{t_0 v_{nmo}^4(t_0)}\int_0^{t_0} v_{nmo}^4(\tau)\left[1+8\eta_{int}(\tau)\right] d\tau - 1\right\}, \tag{2b}$$

where $\eta_{int}(\tau)$ is the instantaneous (interval) anisotropy, and v_{nmo} is the interval NMO velocity given by

$$v_{nmo}(\tau) = v(\tau)\sqrt{1+2\delta(\tau)}, \tag{3}$$

where $v(\tau)$ is the vertical interval velocity and $\delta(\tau)$ is one of the Thomsen's anisotropy parameters (Thomsen, 1986). Note that although Equation 1 has higher accuracy than the conventional Dix equation, it is not suitable for velocity analysis when the absolute value of η_{eff} exceeds 0.2. And large value of η_{eff} might may result in a possible smoother and lower resolution mode of η_{int}. Furthermore equation 1 may introduce up to 2% travel time error when the aperture is greater than 2.0 (Alkhalifah, 1997).

Differential evolution (DE) optimization

Least-squares maximization is usually the optimization engine for automatic velocity analysis (e.g., Toldi, 1989). Classical least-squares requires the Hessian matrix (or approximations of the Hessian using the Jacobian matrix) to define the next search step. Unfortunately the relationship between the stacking power and a given interval model is highly nonlinear (Toldi, 1989). For this reason, we use an efficient, global search engine named differential evolution (DE), which is described in Appendix A, to obtain the optimal interval velocity and anellipticity model. The advantage of DE is that it avoids any estimation of derivatives but rather requires more computation to generate forward models, and it is more expensive than that of least-square based optimization.

The Objective function

Toldi (1989) proposes a two-step workflow to conduct automated hyperbolic velocity analysis. First, he calculates the stacking slowness from predicted trial interval slowness models. Then the algorithm computes the total stacking power of corrected gathers. The model with the greatest stacking power is considered as the best model. We follow Toldi's workflow by extending it to automated nonhyperbolic velocity analysis. Toldi (1989) parameterizes the interval velocity model using equally-spaced increments along the t_0 axis. In contrast, since we focus on residual velocity analysis of migrated gathers, we geologically consider our interval model using user-defined horizons. We choose the semblance S as the estimator of stacking power to minimize cost, though eigenstructure methods provide higher resolution (Key and Smithson, 1990; Sacchi, 1998). The objective of our algorithm is to search an interval model **m** that gives the maximum semblance value S. And the model **m** consists of the interval NMO velocity v_{nmo} and instantaneous (interval) anisotropy η_{int} parameters

$$\mathbf{m} = \left(v_{nmo}, \eta_{\text{int}}\right), \tag{4a}$$

and objective function $Q(\mathbf{m})$

$$Q(\mathbf{m}) = \sum_i \sum_j \sum_k S_i\left(\mathbf{m}, x_j, y_k\right), \tag{4b}$$

where x and y stand for inline and crossline, and indices i, j, k indicate the index of time, inline, and crossline samples.

Figure 2.1 illustrates the proposed workflow for automatic nonhyperbolic velocity analysis. Our input data consist of prestack time migrated CMP gathers, the initial migration velocity, and interpreted horizons. The outputs are flattened gathers, and a model of interval velocity and anellipticity that best flatten the gathers. The prestack gathers are generated from time-migrated gather that have been subjected to a reverse NMO correction using the migration velocity. The horizons are manually interpreted on an offset-limited stack of the migrated gathers, and are used to parameterize the interval model **m**. The algorithm starts by building an initial interval velocity model from migration velocity, then generates suite of alternative models in the decision space. Next, the model undergoes DE mutation and crossover to generate a set of new trial interval models and calculate the effective models using equation 2. The algorithm estimates the objective function for each model, better models survive into the next generation. We repeat generating and evaluating the new models until all the reflection events are flattened, or convergence slows down.

MINIMIZE THE STRETCH ASSOCIATED WITH FAR OFFSET

Migration and NMO corrections are conducted sample by sample which results in the well-known decrease of frequency content and amplitude distortion through stretch at far offset. To avoid the effects of serious stretch associated with far offsets, we usually mute the farther offsets based on a user-defined criterion. Muting of far offset not only lowers the stacking power, it also reduces information necessary for accurate prestack inversion of shear impedance and density. Zhang et al. (2013) developed a wavelet-based algorithm named MPNMO (the matching-pursuit-based normal moveout correction) to minimize the stretch at large aperture. Their algorithm first applies reverse NMO correction, which “resqueezes” the migration stretch of the time migrated gathers, and then conducts a wavelet-based NMO correction on the reverse NMO corrected gathers. In this paper, we apply their workflow to the time migrated gathers using new the velocity and anellipticity model. In this manner, resolution is improved first by aligning the data and second by avoiding stretch. Furthermore the AVO phenomenon exited in the prestack gathers is well preserved.

APPLICATION

To illustrate the effectiveness of the proposed workflow, we apply it to prestack time migrated CMP gathers in the Fort Worth Basin (FWB), USA. The FWB is a foreland basin and covers approximately 54000 mi^2 (14000 km^2) in north-central Texas. The target is Mississippian Barnett Shale which is one of the largest unconventional reservoir in the world and spreads approximately 28000 mi^2 (72520 km^2) across the FWB. Although the Barnett Shale (da Silva, 2013) is present in 38 counties in Texas, production is mainly restricted to Denton, Tarrant, Johnson, and Wise Counties in the northeastern portion of the FWB. Our survey is located in Wise County and has a maximum offset of 13000 ft. The target Barnett Shale lies at approximately 7000 ft depth. Figure 2.2 shows a simplified stratigraphic column of the FWB in Wise County (Silva, 2013; Montgomery et al., 2005). Note the Barnett Shale lies directly on the easy-to-pick Viola limestone.

Figure 2.3 is a representative time-migrated CMP gather using the two-term hyperbolic travel time equation. Note the "hockey stick" and stretch indicated by the white arrows at far offsets. Both "hockey stick" and stretch are harmful for the following processing and prestack inversion. The "hockey stick" can blur reflection events in the stacked volume while the stretch lowers the resolution of shear impedance and inversion volume. Usually, seriously stretched data are muted out (Figure 2.4) based on a user-defined muting criterion. In this example we allow wavelets to stretch no more than 130%. Figure 2.5 shows a prestack gather after applying reverse NMO correction on the gather shown in Figure 2.3. The RMS migration velocity (Figure 2.6a) comes from performing hyperbolic velocity analysis on coarse grid (20x20) super gathers. The migration velocity is then converted to interval velocity (Figure 2.6b) as one of the inputs for our algorithm. Figure 2.7 shows the horizons used for parameterizing the model. They are interpreted on the stacked volume which just uses the near offset data of time migrated gather (Figure 2.4). During each generation we only update the interval slowness and anellipticity values located at those horizons. Other interval model values are interpolated using values on the horizons.

To automatically flatten the gather shown in Figure 2.5 without picking, we apply the workflow shown in Figure 2.1 to obtain the corrected results (Figure 2.8). The initial interval anellipticity η_{int} is set to zero and the maximum absolute value of corresponding η_{eff} is limited to 0.2 during the optimization. The maximum absolute deviation of interval velocity from the initial model is not permitted to more than 20%. Figures 2.9a and 2.9b show the optimal interval NMO velocity and anellipticity. The corresponding optimal RMS velocity and effective anellipticity are respectively shown in Figures 2.9c and 2.9d. Compared to the initial velocity model, the optimized interval NMO and RMS velocity have higher resolution. The differences between initial and optimized velocities are caused by 1) the isotropic assumption compensating for the anellipticity (Abbad, et al., 2009) and 2) the initial velocity analysis performed on coarse grids super gathers having lower lateral resolution. Some correlations are observed between the inverted model and the geology features in the stacked section. For example, velocity pattern (high-low-high) indicated by the white arrows in Figure 2.9a correlates to the Marble Falls Limestone – Upper Barnett Shale – Forestburg Limestone sequences. The velocity increase indicated by the grey arrows corresponds to the Viola limestone. The feature in Figure 2.9b indicated by white arrow is associated with Barnett Shale which is known to be a VTI media. It can be used as a direct anisotropy indicator (Abbad, et al., 2009).

Note that although the reflection events are flattened by our algorithm, we still cannot use the information contained at far offset due to the serious stretch indicated by the white arrows in Figure 2.8. At present MPNMO minimizes the stretch to some extent, but cannot resolve highly interfering and crossing events. Before using this algorithm, we therefore apply muting to the time migrated gathers (Figure 2.3) which allow wavelets to stretch no more than 180% (Figure 2.10a). Then we apply a reverse NMO correction (Figure 2.10b) on the muted gathers. Finally we implement MPNMO algorithm (Figure 2.10c). Note that MPNMO minimizes the stretch that occurs at the far offset data when compared to the original time-migrated gathers. Figures 2.11a and 2.11b shows vertical slices through the stacked volume from traditional time migrated gathers after muting and MPNMO corrected gathers. Note the greater stacked energy (red arrows) and improved resolution (yellow arrow) of the MPNMO results. To better see the improvements, we displayed a zoomed in part of the stacked section (Figure 2.12a and 2.12b) between 1.15s and 1.4s where our reservoir locates. Those horizons are no longer located at the troughs or peaks on the new stacked section and need re-interpretation. Note the improved resolution indicated by yellow arrows and more continuous reflection events indicated by the red arrow. Unfortunately the stacking power indicated by green arrow has lower energy compared to that of conventional. This artifact arises because MPNMO does not properly handle interfering reflections in prestack domain and moves all the interfered energy of current wavelets to the lower reflection events. To quantify the improved resolution, we compare the average amplitude spectra of the stacked data shown in Figure 2.13. The blue and red curves represent the stacked data using gathers shown in Figure 2.4 and MPNMO correction (Figure 2.10c). The MPNMO spectrum obviously has a greater ratio of high to low frequencies.

CONCLUSIONS

"Hockey stick" and stretch are the two main issues associated with long offset data processing. We propose a two-step workflow for maximizing the usage of information contained in far offsets. The first one is an automatic nonhyperbolic velocity analysis to obtain an interval model that gives the maximum stacking power. The interval model based search ensures that the optimized model is physically feasible and avoids sudden variations. In our application the interval velocity has very good correlation with the reflection events in the stacked section. Unfortunately the interval anellipticity is ambiguous and need further comparison to well log data. Nonhyperbolic velocity analysis can mitigate the "Hockey stick" but not the stretch appeared at large aperture. MPNMO minimizes the stretch and improves the stacking power and resolution critical for interpreting thin reservoirs. Another advantage benefiting from MPNMO is that more far-offset data are available for subsequent $\lambda\rho$-$\mu\rho$ and AVO inversion.

The proposed methodology has some short comings. The algorithm favors flattening stronger reflection events due to their large stacking power, and may ignore some weak reflections. Also it still cannot estimate the nonuniqueness in the solution. There may exist a suite of kinematically equivalent models that exhibit identical moveout curves. The employed anti-stretch algorithm cannot decompose the highly compressed or crossing events. Future works therefore include 1) resolving interfering and crossing events in prestack domain and 2) employing well logs as the calibration during the optimization procedure.

ACKNOWLEDGEMENTS

The authors thank Devon Energy for permission to use and show their data. We also thank the sponsors of the Attribute-Assisted Seismic Processing and Interpretation Consortium (AASPI) for their guidance and financial support. The final version of this paper benefited tremendously from the comments and suggestions of the anonymous associated editor, Dr. Kyoung-Jin Lee and three anonymous referees.

APPENDIX A

The differential evolutionary (DE) optimization algorithm used in this paper was initially proposed by Storn and Price (1997). The initial population of DE is randomly generated within the decision space. If the total variable number of the objective function is *K*, then the n^{th} member at the g^{th} generation can be expressed as:

$$\mathbf{m}_{n,g} \equiv \left(m_{n,g}^{(1)},\quad \ldots,\quad m_{n,g}^{(k)},\quad \ldots,\quad m_{n,g}^{(K)}\right) \quad n=1,2,\ldots,N;\ g=1,2,\ldots,G, \tag{A-1}$$

where *N* is the population number, *G* is the total generation, and *k* is the index for variables. DE exhibits the basic features of any general evolutionary algorithm and is comprised of mutation, crossover, and selection.

Mutation: For a given target vector $\mathbf{m}_{n,\mathrm{g}}$ at generation *g*, randomly select three vectors from the population to generate the donor vector:

$$\mathbf{v}_{n,g} = \mathbf{m}_{r_1,g} + F \cdot \left(\mathbf{m}_{r_2,g} - \mathbf{m}_{r_3,g}\right), \tag{A-2}$$

where the indexes r_1, r_2, and r_3 represent selected integers from [1,*N*] that are different from n, and *F* is a user-defined scaling factor.

Crossover: The target vector $\mathbf{m}_{n,\mathrm{g}}$ is recombined with the donor vector $\mathbf{v}_{n,\mathrm{g}}$ to develop the trial vector $\mathbf{u}_{n,\mathrm{g}}$. Elements of the donor vector enter the trial vector with a probability C_r:

$$u_{n,g}^{(k)} = \begin{cases} v_{n,g}^{(k)} & \text{if } RAND(0,1) \le C_r \\ m_{n,g}^{(k)} & \text{otherwise} \end{cases} \tag{A-3}$$

where n=1,2,⋯,*N*, *k*=1,2,⋯,*K*, *RAND*(0,1) is the k^{th} evaluation of a uniform random number generator.

Selection: The target vector $\mathbf{m}_{n,\mathrm{g}}$ is evaluated against the trial vector $\mathbf{u}_{n,\mathrm{g}}$, with the better model surviving into the next generation:

$$\mathbf{m}_{n,\mathbf{g+1}} = \begin{cases} \mathbf{u}_{n,\mathbf{g}} & \text{if } Q(\mathbf{u}_{n,\mathbf{g}}) \le Q(\mathbf{x}_{n,\mathbf{g}}) \\ \mathbf{m}_{n,\mathbf{g}} & \text{otherwise} \end{cases}. \qquad \text{(A-4)}$$

We repeat implementing equation A-2 to A-4 until the maximum generation *G* is reached or the convergence rate is smaller than user-defined value.

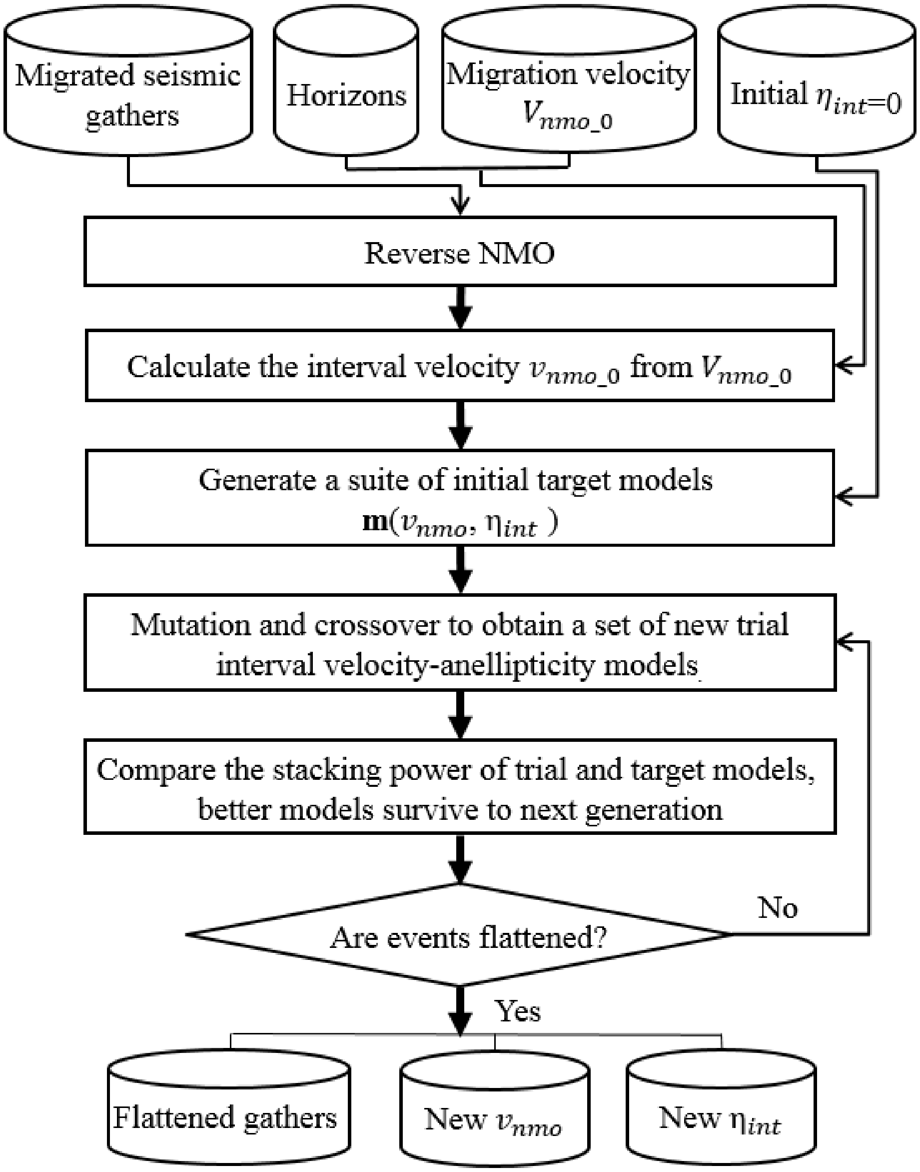

Figure 2.1. Flowchart showing the automated nonhyperbolic velocity analysis. The model parameters consist of interval NMO velocity and anellipticity. The objective is to find a model that gives the maximum stacking power using a global optimization strategy called differential evolution.

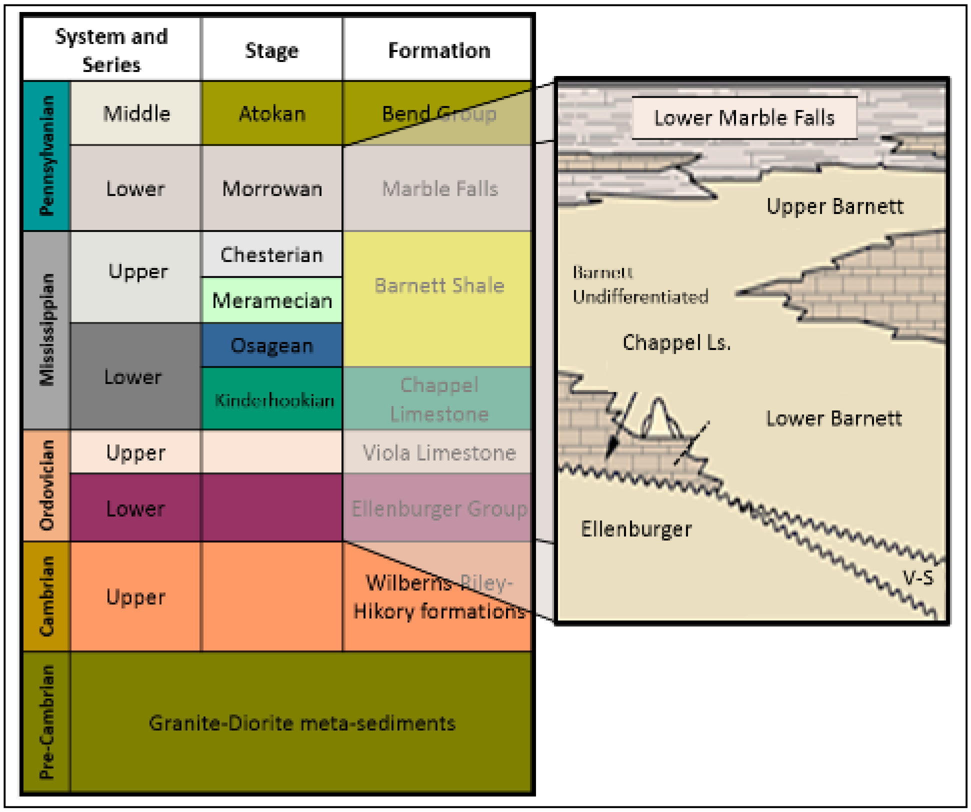

Figure 2.2. Simplified stratigraphic column of the Fort Worth Basin in Wise County (da Silva, 2013). The Barnett Shale lies between the Marble Falls and Viola Limestone in our survey area.

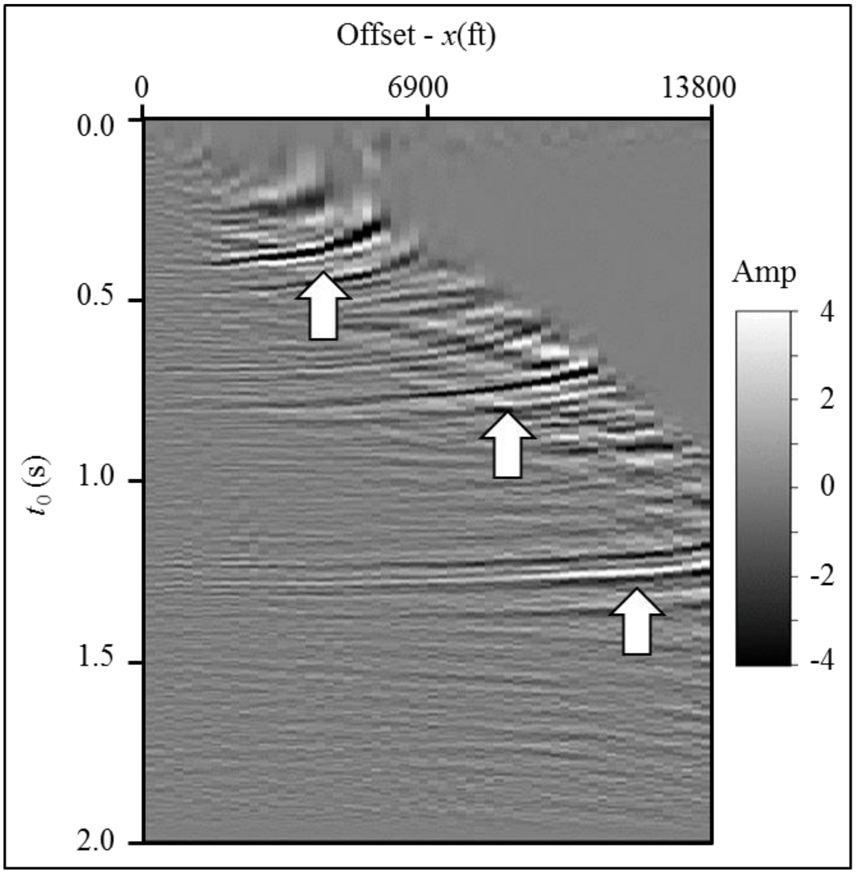

Figure 2.3. A representative time-migrated CMP gather using two term hyperbolic travel time equation and the migration velocity shown in Figure 2.6. Note the "hockey stick" and stretch indicated by the white arrows at far offset.

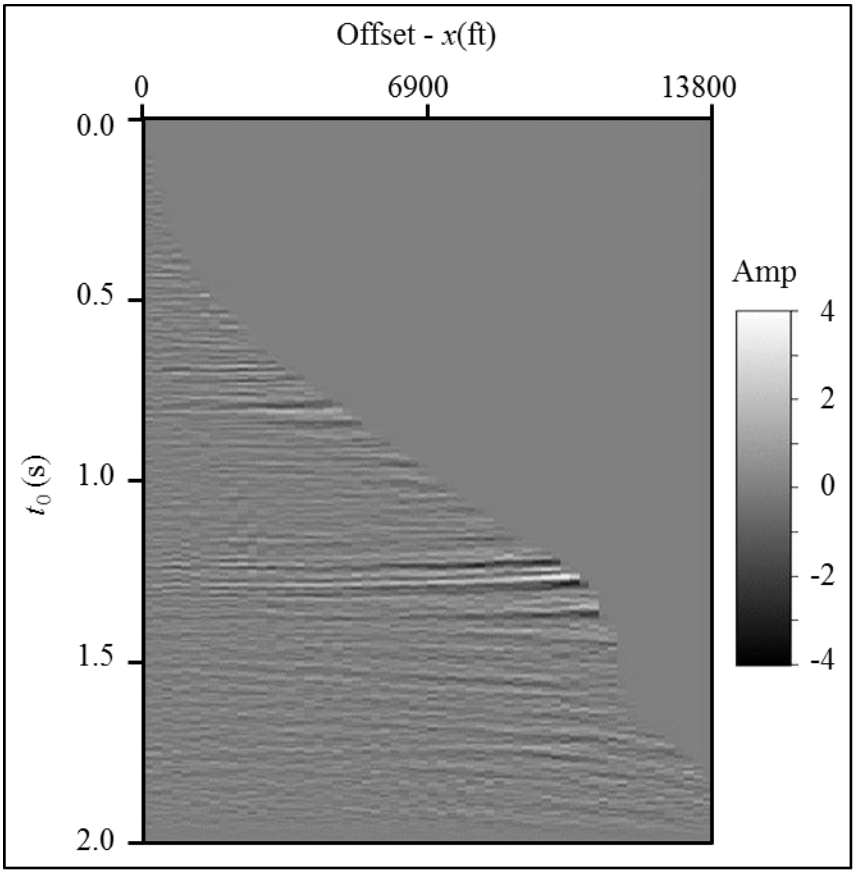

Figure 2.4. The gather shown in Figure 2.3 after muting. The wavelet is not allowed to stretch more than 130%, resulting in the loss of information in the far offset.

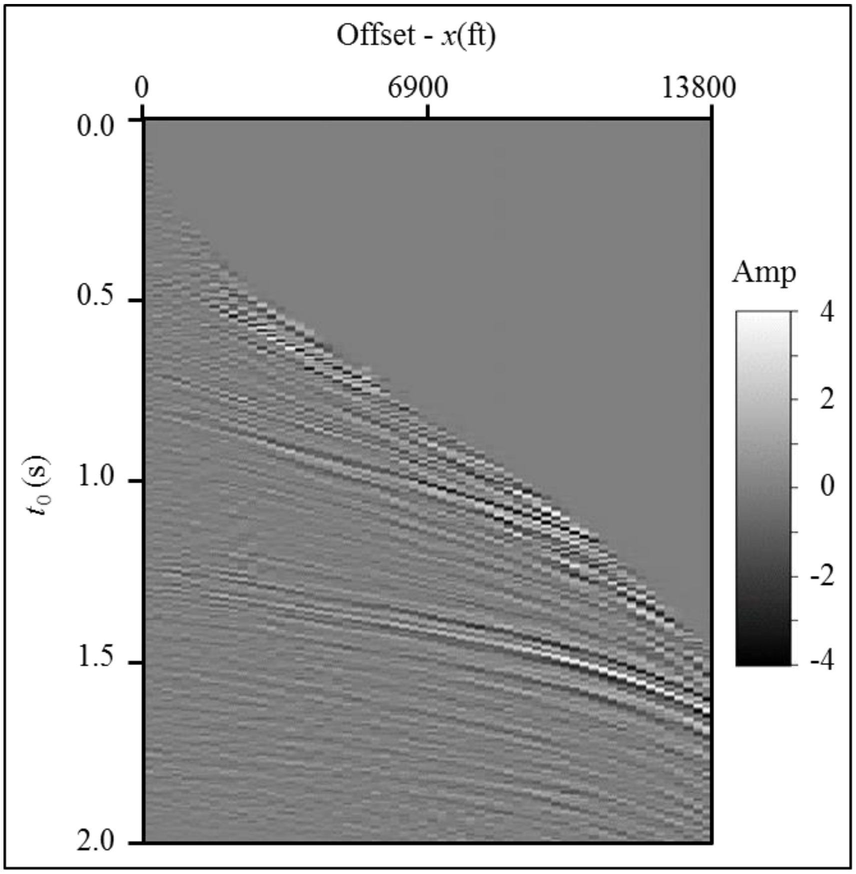

Figure 2.5. The gather shown in Figure 2.3 after applying reverse NMO. This gather server as input to automatic nonhyperbolic velocity analysis.

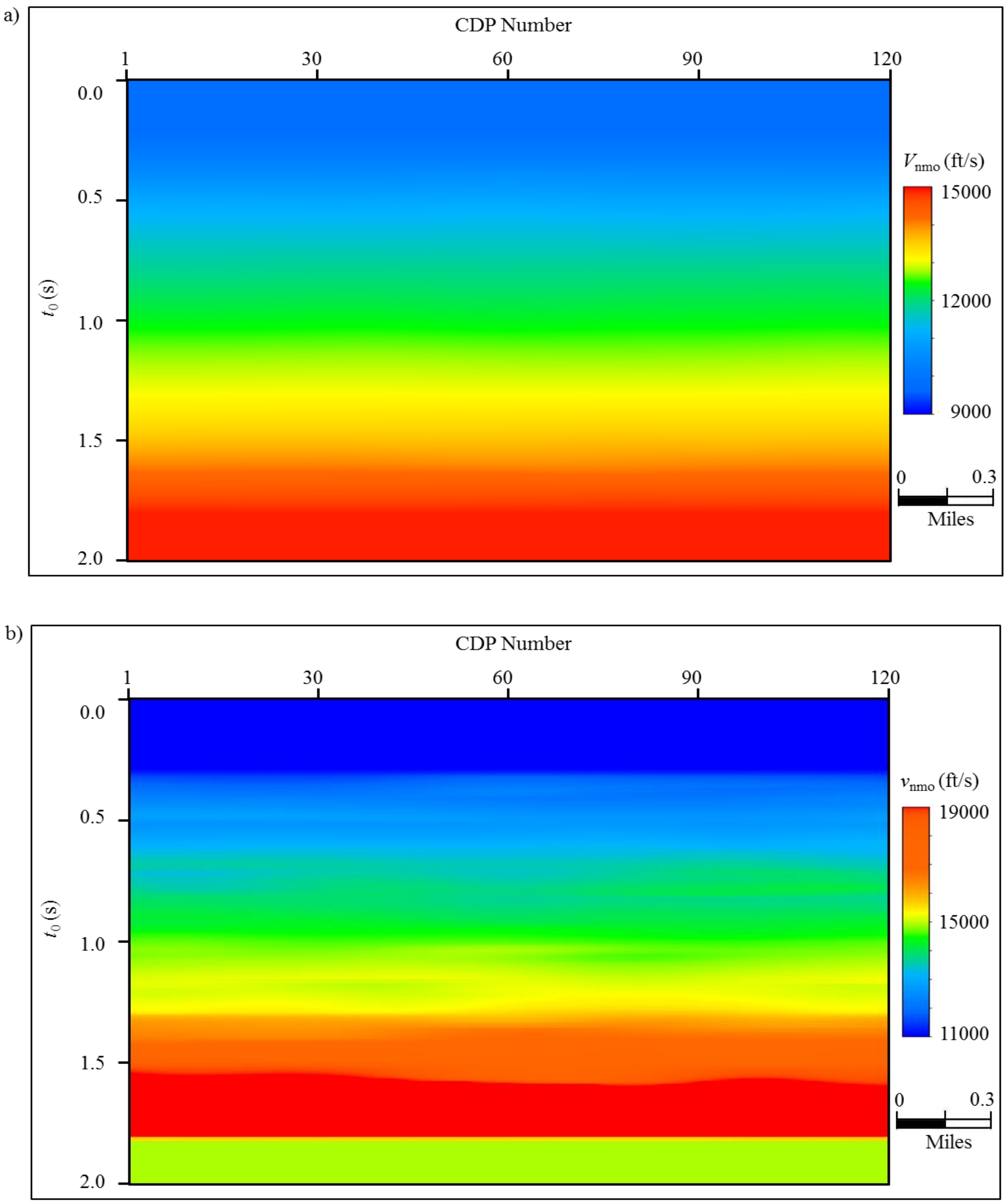

Figure 2.6. Velocity analysis results performed on the coarse grid (20x20) super gathers. (a) RMS velocity from hyperbolic velocity analysis on the offset truncated gathers and (b) interval velocity converted from the RMS velocity. This interval velocity is used for generating the initial target interval velocity. The initial interval anellipticity is set to 0.

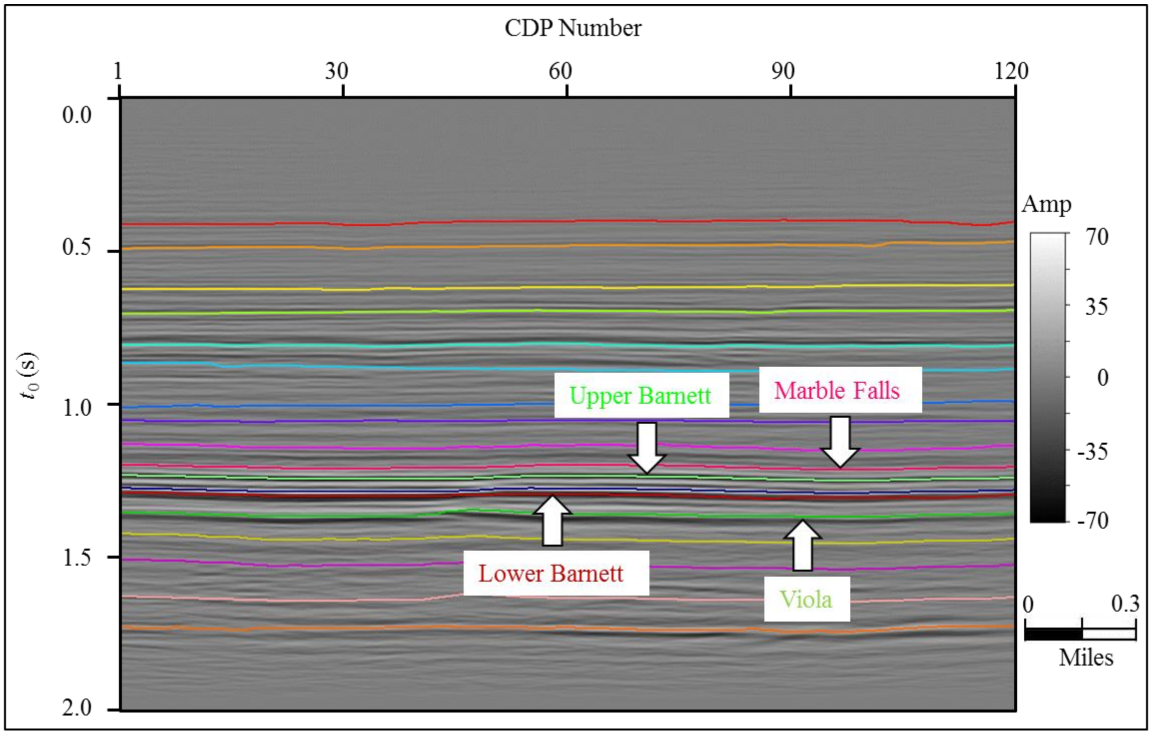

Figure 2.7. Horizons used in parameterizing the model. We interpreted these 18 horizons on the stacked volume of near-offset time migrated gathers (Figure 2.4). The named horizons are tied to wells. Unnamed horizons provide further constraints.

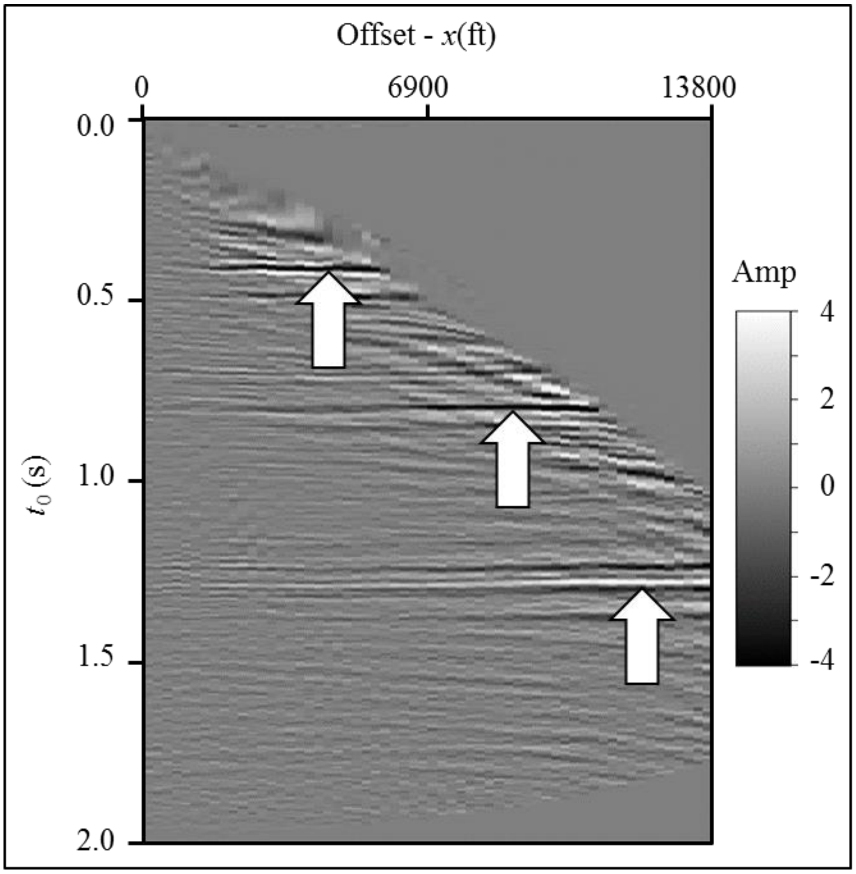

Figure 2.8. Flattened representative gathers using the workflow shown in Figure 2.1. Note the “hockey stick” is gone but not the stretch.

a)

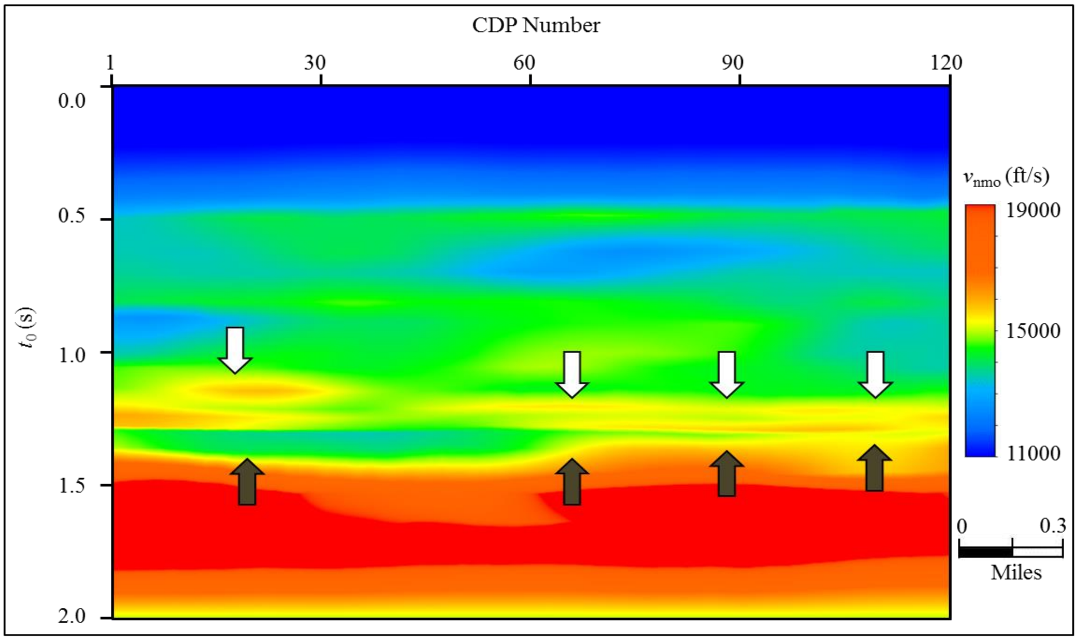
CDP Number
1
30
60
90
120
0.0
0.5
1.0
1.5
2.0
t_0 (s)
v_{nmo} (ft/s)
19000
15000
11000
0
0.3
Miles

b)

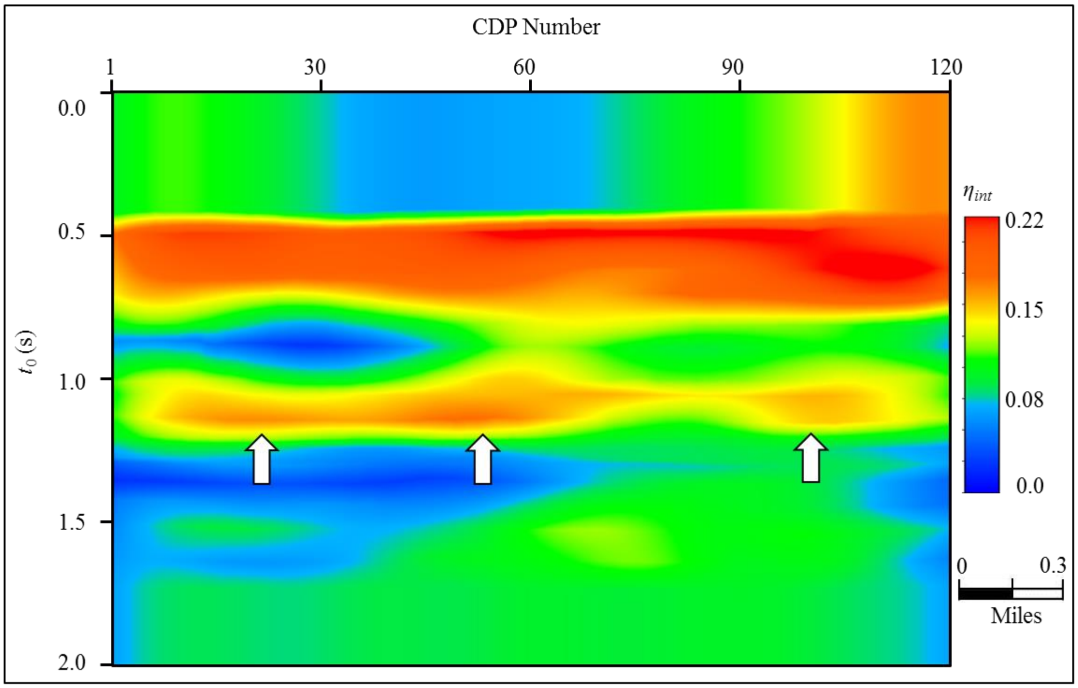
CDP Number
1
30
60
90
120
0.0
0.5
1.0
1.5
2.0
t_0 (s)
η_{int}
0.22
0.15
0.08
0.0
0
0.3
Miles

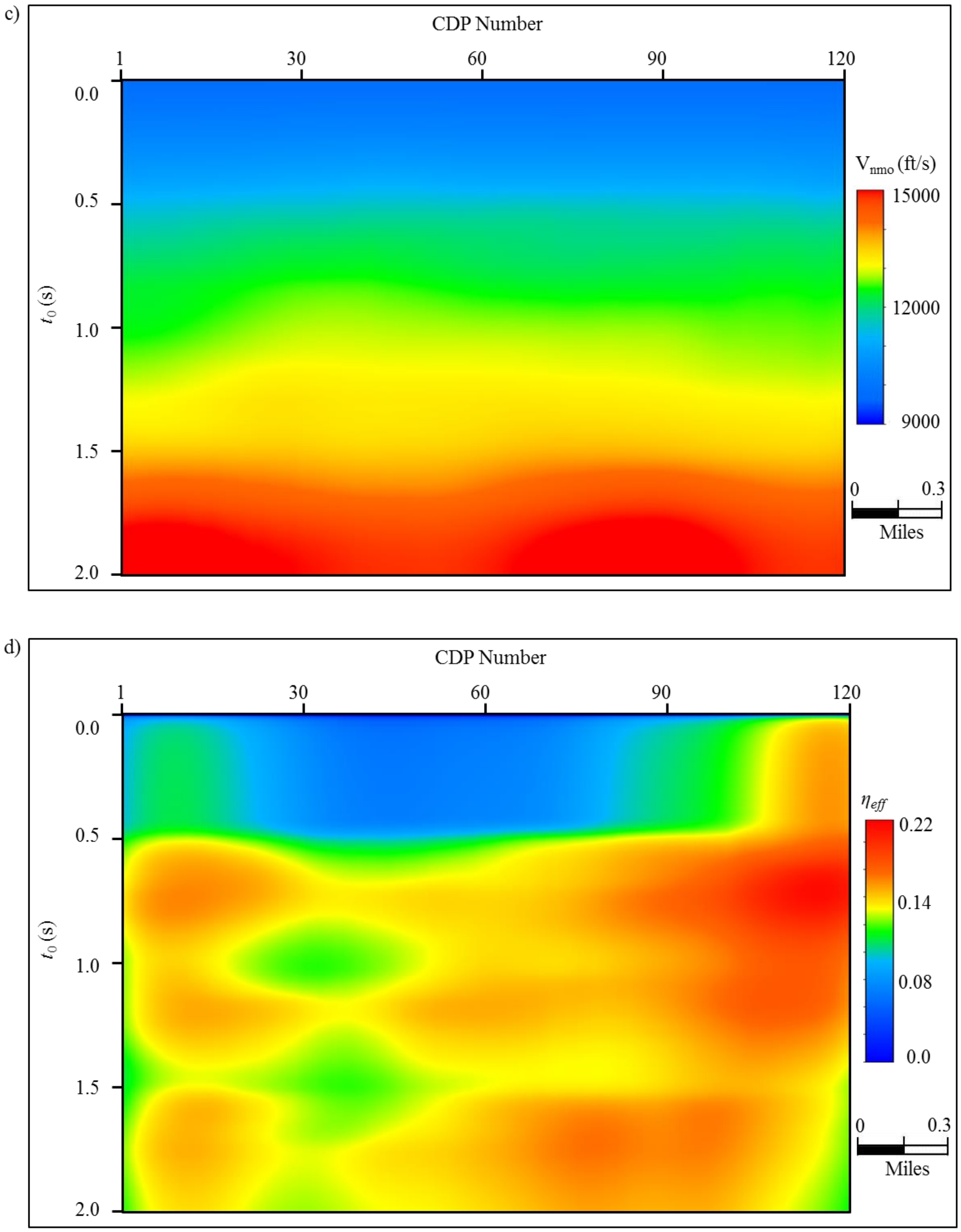

Figure 2.9. Optimized model results using the workflow shown in Figure 2.1. During the optimization procedure, we first the update interval NMO velocity (a) $\boldsymbol{v_{nmo}}$ and (b) $\boldsymbol{\eta_{int}}$, then calculate the corresponding (c) RMS velocity and (d) effective anellipticity. The optimal interval velocity has higher resolution than the initial interval velocity (Figure 2.6b).

a)

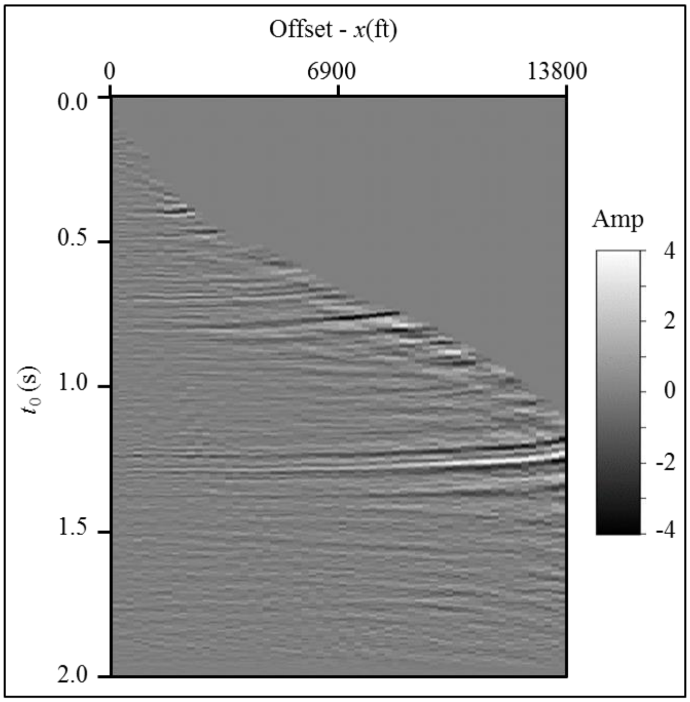
Offset - x(ft)
0
6900
13800
0.0
0.5
1.0
1.5
2.0
t_0 (s)
Amp
4
2
0
-2
-4

b)

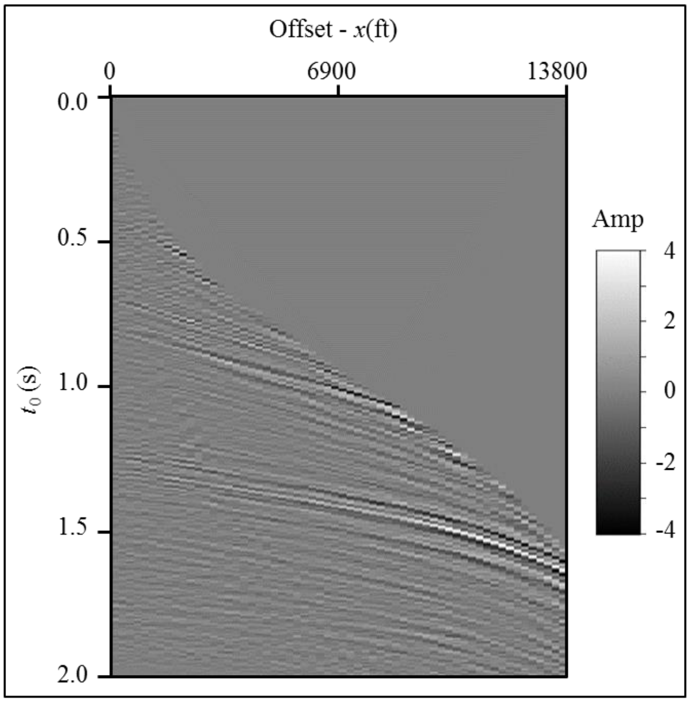
Offset - x(ft)
0
6900
13800
0.0
0.5
1.0
1.5
2.0
t_0 (s)
Amp
4
2
0
-2
-4

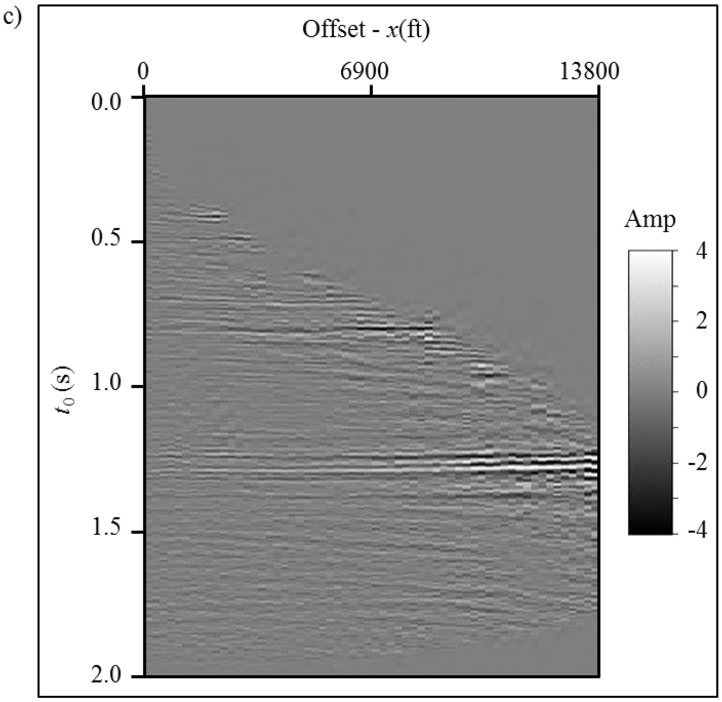

Figure 2.10. Anti-stretch processing applied to prestack gathers. Representative gather after (a) muting and (b) reverse NMO correction. The muting is applied on the time migrated gathers shown in Figure 2.3 where the wavelet is not allowed to stretch more 180%. Reverse NMO is applied to the muted gather. (c) The anti-stretching processed results. Note we minimize the stretch at far offsets.

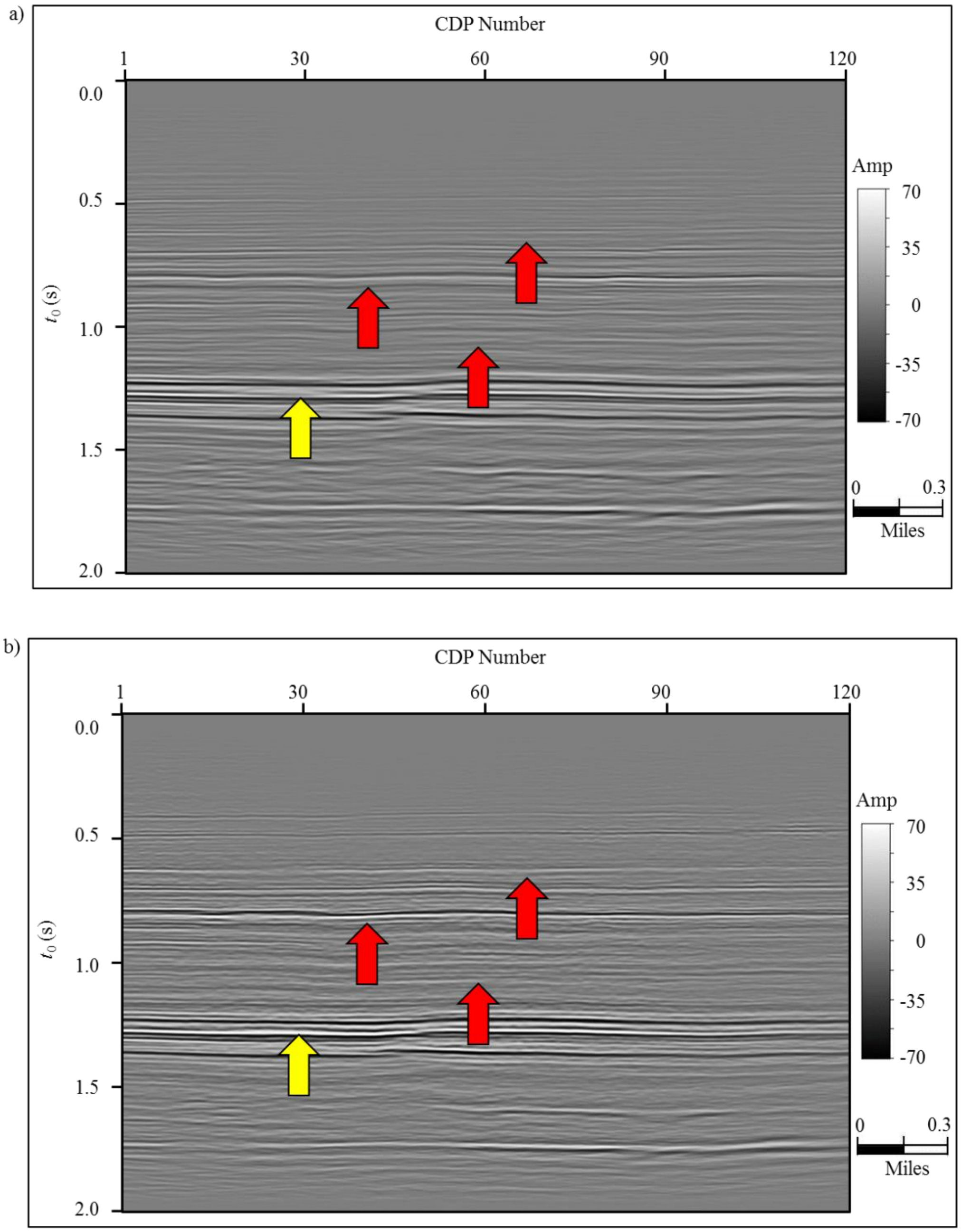

Figure 2.11. Stacked sections after (a) conventional migrated gathers with 130% muting criteria and (b) MPNMO correction gathers with 180% muting criterion. The target Barnett Shale lies between t=1.1*s* and t=1.3*s*. Note the improved stacking power indicated by the red arrows and vertical resolution indicated by yellow arrow.

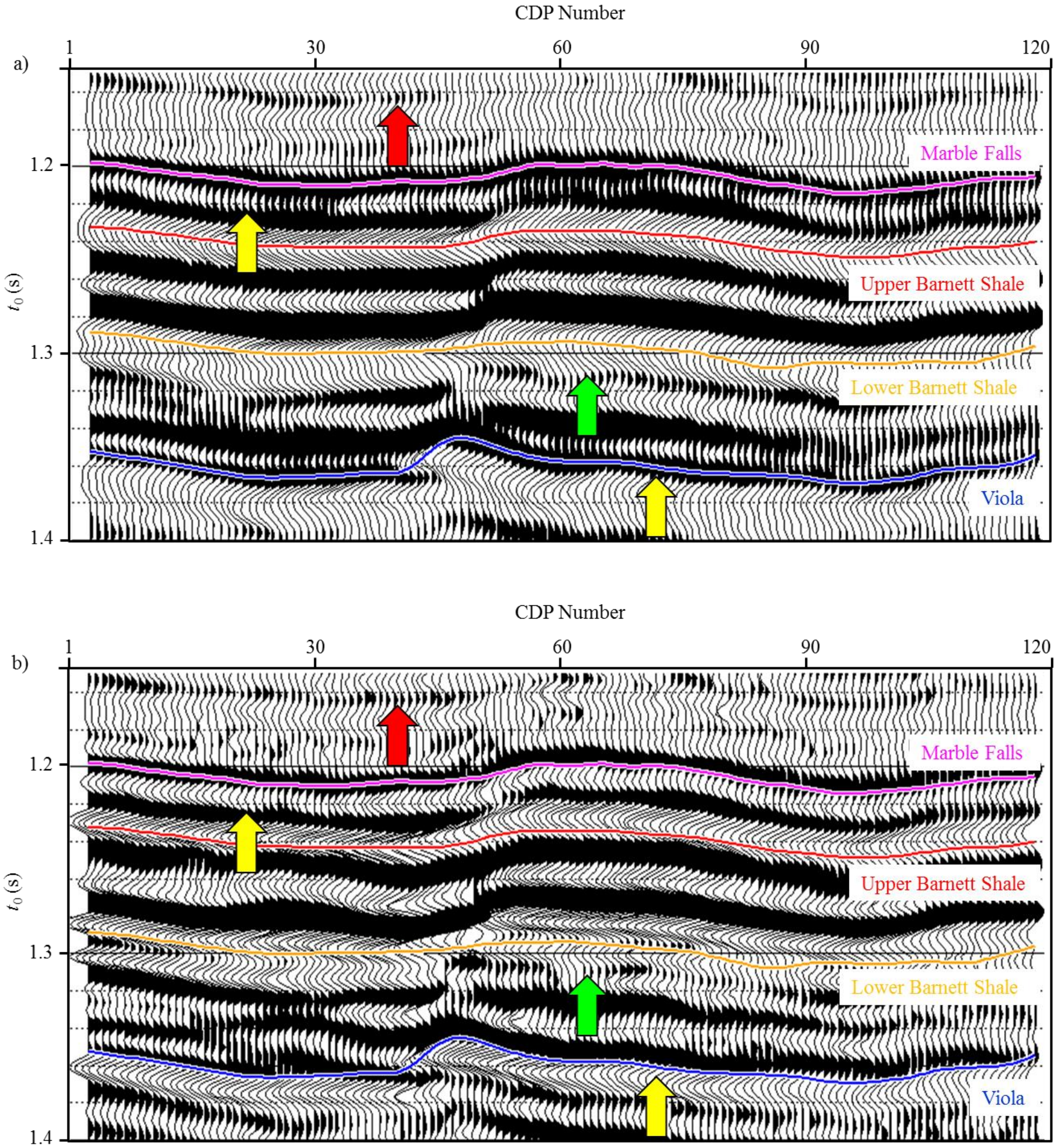

Figure 2.12. Zoom in display the stacked section of target reservoirs from (b) conventional (a) and (b) proposed residual velocity analysis workflow. Note we have more continuous reflection events (red arrows) and improved resolution (yellow arrow).

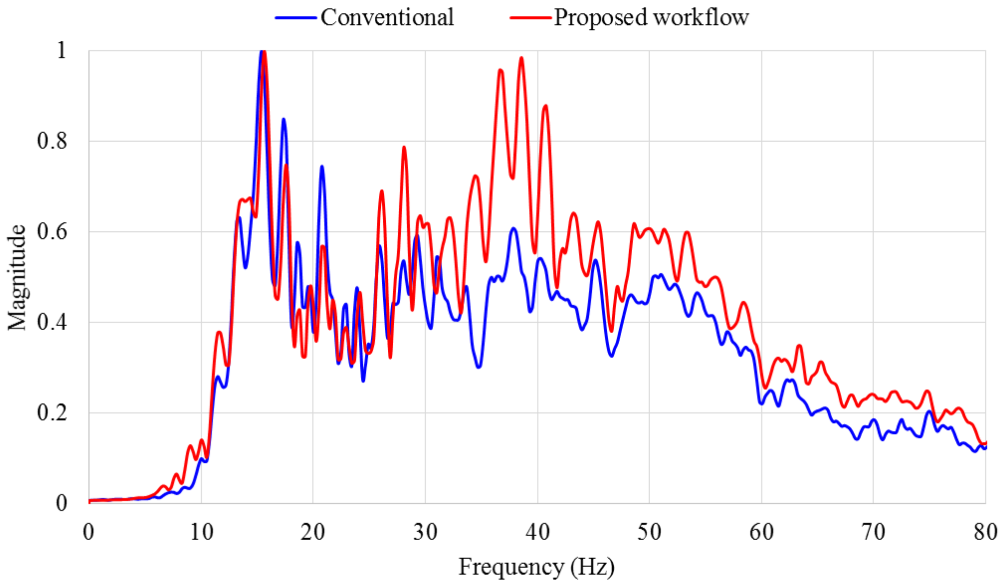

Figure 2.13. Spectra of stacked section from conventional- (blue) and proposed- (rea) processing. Note the spectrum of new stacked section obviously has a greater ratio of high to low frequencies.

REFERENCES

Abbad, B., B. Ursin, and D. Rappin, 2009, Automatic nonhyperbolic velocity analysis: Geophysics, **74**, U1-U12.

Alkhalifah, T., and I. Tsvankin, 1995, Velocity analysis for transversely isotropic media: Geophysics, **60**, 1550-1566.

Alkhalifah, T., 1997, Seismic data processing in vertically inhomogeneous TI media: Geophysics, **62**, 662-675.

Alkhalifah T., 2011, Scanning anisotropy parameters in complex media, Geophysics, **76**, U13-U22.

Biondi, B., and C. Kostov, 1989, High-resolution velocity spectra using eigenstructure methods, Geophysics, **54**, 832-842.

Bolshykh, S. F., 1956, About an approximate representation of the reflected wave traveltime curve in the case of a multi-layered medium: Applied Geophysics (in Russian), **15**, 3-15.

Calderón-Macías, C., M. K. Sen, and P. L. Stoffa, 1998, Automatic NMO correction and velocity estimation by a feed-forward neural network: Geophysics, **63**, 1696-1707.

Castle, R. J., 1994, A theory of normal moveout: Geophysics, **59**, 983-999.

Choi, H., J. Byun, and S. J. Seol, 2010, Automatic velocity analysis using bootstrapped differential semblance and global search methods: Exploration Geophysics, **41**, 31-39.

da Silva, M., 2013, Production correlation to 3D seismic attributes in the Barnett Shale, Texas: M.S. thesis, The University of Oklahoma.

de Bazelaire, E., 1988, Normal moveout revisited: Inhomogeneous media and curved interfaces: Geophysics, **53**, 143-157.

Dix, C. H., 1955, Seismic velocities from surface measurements: Geophysics, **20**, 68-86.

Fomel, S., 2009, Velocity analysis using AB semblance: Geophysical Prospecting, **57**, 311-321.

Fomel, S., and A. Stovas, 2010, Generalized nonhyperbolic moveout approximation: Geophysics, **75**, U9-U18.

Key, S. C., and S. B. Smithson, 1990, New approach to seismic-event detection and velocity determination: Geophysics, **55**, 1057-1069.

Kirlin, R. L., 1992, The relationship between semblance and eigenstructure velocity estimators: Geophysics, **57**, 1027-1033.

Larner, K., and V. Celis, 2007, Selective-correlation velocity analysis: Geophysics, **72**, U11-U19.

Luo, S., and D. Hale, 2012, Velocity analysis using weighted semblance: Geophysics, **77**, U15-U22.

Montgomery, S. L., D. M. Jarvie, K. A. Bowker, and R. M. Pollastro, 2005, Mississippian Barnett Shale, Fort Worth basin, north-central Texas: Gas-shale play with multitrillion cubic foot potential: AAPG Bulletin, **89**, 155-175.

Neidell, N. S., and M. T. Taner, 1971, Semblance and other coherency measures for multichannel data: Geophysics, **36**, 482-497.

Sacchi, M., 1998, A bootstrap procedure for high-resolution velocity analysis, Geophysics: **63**, 1716-1725.

Siliqi, R., D. Le Meur, F. Gamar, L. Smith, J. P. Touré, and P. Herrmann, 2003, High-density moveout parameter fields V and η: Part one: Simultaneous automatic picking: 73rd Annual International Meeting, SEG, Expanded Abstracts, 2088-2091.

Storn R., and K. Price, 1997, Differential evolution – a simple and efficient heuristic for global optimization over continuous space: Journal of Global Optimization, **11**, 341-359.

Swan, H.W., 2001, Velocities from amplitude variations with offset: Geophysics, **66**, 1735-1743.

Taner, M. T., and F. Koehler, 1969, Velocity spectra: digital computer derivation and application of velocity functions: Geophysics, **34**, 859-881.

Thomsen, L., 1986, Weak elastic anisotropy: Geophysics, **51**, 1954-1966.

Toldi, L. T., 1989, Velocity analysis without picking: Geophysics, **54**, 191-199.

van der Baan, M., and J. M. Kendall, 2002, Estimating anisotropy parameters and traveltimes in the *τ-p* domain: Geophysics, **67**, 1076-1086.

Zhang, B., K. Zhang, S. Guo and K. J. Marfurt, 2013, Nonstretching NMO correction of prestack time-migrated gathers using a matching-pursuit algorithm: Geophysics, **78**, U9-U18.

Chapter 3: Improving the confidence of prestack inversion by preserving the data fidelity in long offset

Bo Zhang[1], Deshuang Chang[1, 2], Tengfei Lin[1], and Kurt J. Marfurt[1],

[1]The University of Oklahoma, ConocoPhillips School of Geology and Geophysics,

[2]BGP Inc., China National Petroleum Company,

This paper has been submitted to the SEG/AAPG journal Interpretation in 2014.

Title: Improving the confidence of prestack inversion by preserving the data fidelity in long offset

ABSTRACT

Prestack seismic inversion techniques provide valuable information of rock properties, lithology, and fluid content for reservoir characterization. The confidence of inverted results increases with increasing incident angle of the seismic gathers. The most accurate result of simultaneous prestack inversion of P-wave seismic data is P-impedance. S-impedance estimation become reliable with incident angles approaching 30^o, while density evaluation become reliable with incident angles approaching 45^o. As offset increases we often encounter "hockey sticks" and severe stretch at far offsets. Both "hockey stick" and stretch not only lower the seismic resolution but also hinder long offset prestack seismic inversion analysis. The invention results are also affected by the random noises presented in the prestack gathers. In this paper we present a three-step workflow to perform data conditioning prior to simultaneous prestack inversion. First, we mitigate the "hockey sticks" by using an automatic nonhyperbolic velocity analysis. Then we minimize the stretch at far offset by employing an anti-stretch workflow. Last, we improve the signal-to-noise ratio (SNR) by applying prestack structure oriented filtering. We illustrate our workflow by applying it to a prestack seismic volume acquired over the Fort Worth Basin (FWB), TX. The results inverted from the conditioned prestack gathers have higher resolution and better correlation coefficients with well logs when compared to those inverted from conventional time migrated gathers.

INTRODUCTION

Simultaneous prestack inversion provides estimation of acoustic impedance (Z_p), shear impedance (Z_s), and density. Those estimations represent the intrinsic rock properties and are commonly used for predicting fluid, lithology, and geomechanical properties. Preserving data fidelity in the prestack seismic gathers is key to obtaining reliable impedance and density estimations. The main factors that affects the data fidelity in the restack gathers include 1) "hockey sticks" in the long offset seismic surveys, 2)NMO/migration stretch, and 3) random noise.

"Hockey sticks" arise in the long offset of prestack gathers when we do not accounting for the effects of anisotropy (Alkhalifah, 1997; Fomel and Stovas, 2010) and long-offset (Taner and Koehler, 1969; de Bazelaire, 1988) in seismic processing. To mitigate the "hockey stick" at far offset, we need to perform nonhyperbolic velocity analysis using a proper travel time equation. The conventional nonhyperbolic velocity analysis (CNVA) first estimates the NMO velocity (V_{nmo}) on offset-limited gathers using a hyperbolic NMO correction, then picks effective anellipticity (η_{eff}) using the full-offset gathers. CNVA produces estimated model of V_{nmo} and η_{eff} on coarse grid of super gathers. The model at other common midpoint (CMP) gathers are interpolated from those at manually picked grids. However there is no guarantee that the interpolated velocity model is correct for all CMPs. Another disadvantage is that small aperture V_{nmo} analysis may be inaccurate. Picking errors in V_{nmo} introduce errors into the subsequent analysis of η_{eff}. Unfortunately simultaneously manual picking of V_{nmo} and η_{eff} at every CMP location is time consuming and tedious. In this paper, we extended Toldi's (1989) automatic velocity analysis to mitigate the "hockey stick" in the long offset.

Migration and NMO corrections are conducted sample by sample which results in the well-known decrease of frequency content and amplitude distortion through stretch at far offset. To avoid the effects of serious stretch associated with far offsets, we usually mute the farther offsets based on a user-defined criterion. Muting of far offset not only lowers the stacking power, it also reduces the accuracy and vertical resolution of prestack inversion for shear impedance and density. Zhang et al. (2013) developed a wavelet-based algorithm named MPNMO to minimize the stretch at far offset. Their algorithm first applies reverse NMO correction, which "resqueezes" the migration stretch of the time migrated gathers, and then conducts a wavelet-based NMO correction on the reverse NMO corrected gathers. We apply their algorithm to minimize the stretch after having computed V_{nmo} and η_{eff} using automatic nonhyperbolic velocity analysis.

Seismic signal is almost always contaminated with noise. To mitigate this undesired component of the seismic data, we assume that proper filters have already rejected the coherent noise (such as multiples) and that the remaining "noise" is random prior to applying our data conditioning workflow. If we assume the noise and reflected signals are uncorrelated, then we can decompose the prestack gathers into signal and noise parts by principal component analysis (Key and Smithson, 1990) along the structural dip.

In this paper, we present a three-step workflow to perform prestack seismic data conditioning prior to prestack inversion. First we mitigate the "hockey sticks" by using an automatic nonhyperbolic algorithm. We then minimize the stretch at far offset using an anti-stretch procedure. Finally we improve the SNR by applying a prestack-oriented filtering. The workflow is validated on a seismic data volume acquired over the Fort Worth Basin, TX.

STRATEGIES TO PRESERVE THE DATA FIDELITY AT FAR OFFSET

To use the critical information contained in the long offset data for prestack inversion, we need to 1) flatten the reflections at far offset using a nonhyperbolic travel time equation, 2) minimize the stretch typically associated with far offset, and 3) improve the SNR by prestack structure oriented filtering.

Mitigating the "hockey stick" using automatic nonhyperbolic velocity analysis

To mitigate the "hockey stick" associated with far offset and anisotropy, we employ an automatic nonhyperbolic velocity analysis algorithm (Zhang et al., 2014). The model $\mathbf{m}$ of the algorithm consists of the interval NMO velocity v_{nmo} and instantaneous (interval) anisotropy η_{int} parameters. The workflow employs a genetic differential evolutionary (DE) algorithm to find the best model that can mitigate the "hockey stick" at far offset. Our input data consist of prestack time migrated CMP gathers, the initial migration velocity, and interpreted horizons. The outputs are flattened gathers, and a model of interval velocity and anellipticity that best flatten the gathers. The prestack time-migrated gathers have been subjected to a reverse NMO correction using the migration velocity. The horizons are manually interpreted on an offset-limited stack of the migrated gathers, and are used to parameterize the interval model. The algorithm starts by building an initial interval velocity model from the migration velocity and setting the initial anellipticity model to 0, then generates a suite of alternative models in the decision space. Next, the model undergoes DE mutation and crossover to generate a set of new trial interval models. The algorithm estimates the objective function for each model. Better models survive into the next generation. We repeat generating and evaluating the new models until all the reflection events are flattened, or convergence slows down.

Minimizing the stretch at far offset

The conventional NMO correction which processes the data sample-by-sample results in the well-known decrease of frequency content and amplitude distortion through stretch. The NMO-uncorrected traces, $d(t)$, can be regarded as the convolution of the seismic wavelet with the reflectivity series and added noise

$$d(t) = r(t) * w(t) + n(t),$$

(1)

where $r(t)$ is reflectivity series, $w(t)$ is wavelet, and $n(t)$ is noise. This classic theory suggests that the NMO correction can be implemented on a wavelet-by-wavelet basis, with the moveout applied to the reflection events, $r(t)$, rather than to the data samples, $d(t)$. Zhang et al. (2013) achieved this goal by using an algorithm named MPNMO. Our input data consist of pre-stack time migrated seismic gathers, $d(t, x_n)$, after performing reverse NMO correction using the migration velocity function. The output is the non-stretch NMO corrected gathers.

Improving SNR

By assuming that 1) coherent noise have been filtered using proper filters, 2) noise and reflected signals are uncorrelated with zero mean, and 3) noise is uncorrelated from trace to trace and sample to sample, Key and Smithson (1990) concluded that the first few eigenvalues and eigenvectors of the covariance matrix of prestack seismic gathers represent the coherent reflection signals. Based on this assumption, we apply a prestack structure oriented filter (PSOF) based on principal component analysis (PCA) to the seismic gathers to improve the SNR. The workflow begins by calculating the reflectors dip in a running window on all traces of the stacked volume (Marfurt, 2006). Then we estimate the correlation coefficients for the stack volume along the local reflection dip (Gersztenkorn and Marfurt, 1999). Next we extract the reflection signal whose correlation coefficients are greater than a user defined threshold through the first eigenvalue and eigenvector of seismic covariance matrix. The signals whose correlation coefficients are less than the threshold do not undergo any processing, thereby preserving potential discontinuities.

Prestack seismic data conditioning workflow

Figure 3.1 summarizes the proposed workflow for preserving the data fidelity contained the far offset. Our input data consist of prestack time migrated gathers and the initial migration velocity $V_{\mathrm{nmo\_0}}$. The initial effective anisotropy η_{eff} is set to 0. We obtain the initial migration velocity by performing hyperbolic velocity analysis on coarse grid super gathers. The workflow begins by performing reverse NMO on the time migrated gathers using the initial migration velocity. Then we obtain the optimal velocity and anellipticity model using our automatic algorithm. Next we apply MPNMO to the time migrated gathers using new velocity and anellipticity model resulting in flattened nonstretched prestack gathers. Lastly we apply PSOF to further improve the SNR. In this manner, both stacking power and vertical resolution are improved first by aligning the data and second by avoiding stretch.

APPLICATION

To evaluate the data quality processed by our workflow, we first apply it to pre-stack time-migrated gathers acquired in the Fort Worth Basin (FWB), USA. We then compare the prestack inversion results computed from migrated gathers using conventional (muting) analysis and our proposed data conditioning workflow. The FWB is a foreland basin and covers approximately 54000 mi^2 in north-central Texas. The target is the Mississippian Barnett Shale which is one of the largest unconventional reservoir in the world and spreads approximately 28000 mi^2 across the FWB. In our survey the “core” or main production area is the Barnett Shale formation lies between 1.2s and 1.4s. The maximum offset is around 14000 ft while the target Barnett Shale lies at approximately 7000 ft depth, implying a maximum incidence angle of about 45^o.

Figure 3.2a shows a representative time migrated CMP gather using a two term hyperbolic travel time equation. Note the “hockey stick” and stretch indicated by white arrows at far offset. To avoid the effect of serious stretch, we usually the mute those serious stretched data according to a user defined criterion. Figure 3.2b shows the muted gather where the wavelet is not allowed to stretch more than 130%. By combining NMO velocity (V_{nmo}) and effective anellipticity (η_{eff}), nonhyperbolic velocity analysis can mitigate the “hockey stick” but not the stretch at far offset (Figure 3.2c). Figure 3.2d shows the flattened nonstretch gather. Note that MPNMO minimizes the stretch that occurs at the far offset data when compared to the original time-migrated gathers. Figures 3.2e and f show the same gather after apply PSOF and the rejected random noise, respectively.

P-impedance is the most reliable result from prestack inversion. S-impedance estimation become reliable when the incidence angle reaches 30^o, while density become reliable when the angle approaching to 45^o. By applying the proposed workflow, more far offset data (Figure 3.2e) are available for the subsequent processing and inversion. We apply simultaneous prestack inversion to the gathers from both the conventional (Figure 3.2b) and the long offset preservation (Figure 3.2e) processing. We first extract the angle dependent statistical wavelets for both the conventional migrated (Figure 3.3a) and the conditioned (Figure 3.3b) data after the seismic-well tie. The red, blue, and green lines show the extracted small (0^o-12^o), intermediate (12^o-24^o), and large angle wavelets (24^o-36^o), respectively. Note that the large angle wavelet extracted from time migration is distorted to some extent. To better compare the improvements, we show the amplitude spectrum of the extracted wavelets from time migrated and conditioned gathers in Figures 3.3c and d. Due to the increasing stretch with increasing incidence angle in the time migrated gathers, the spectral bandwidth (the blue and green lines in Figure 3.3c) of the intermediate and large angle wavelets are distorted and narrower than that of the small angle wavelet (the red line in Figure 3.3c). However the proposed conditioning workflow preserves the spectral bandwidth of the intermediated and large angle (the blue and green lines in Figure 3.3d). Another factor responsible for the narrower bandwidth of large angle wavelet is that we applied a low pass antialiasing filters to the far offset data internal to the time migration algorithms (Biondi, 2001). Figures 3.4, 3.5, and 3.6 compare the inverted P-impedance, S-impedance, and density from the conventional and long offset preservation gathers. The vertical black curve in those figures are the well tract that used to quality control the inversion results. We observe an overall improvement by including the long offsets, especially for the inverted S-impedance. For example, the formations indicated by the white arrow in the new inverted results from conditioned data are more laterally continuous compared to those from of conventional data. The zone indicated by dark arrows in the new data have higher resolution compared to that of conventional data. These improvement are due to our ability to preserve the frequency content for wavelet in the mid- and far-offset in particular. To better see the improvement, we quality control our inverted results from (Figure 3.7a) time migrated and (Figure 3.7b) conditioned gathers with well logs at the target zone. The left, middle, and right tracks show the P-impedance, S-impedance, and density panels. The black, blue, and red curves indicate the initial model, the original well logs, and the inverted results. The blue curves are the inverted result from conventional processed gathers while the red curves are the inverted result from the conditioned gathers. Note we have obvious improvements in the zone indicated by the red arrows. The new inverted results show a better correlation to the original well logs. The improvement of density is not as good as those of P- and S-impedance. This is due to that the maximum incidence angle of our gather is approximately 36^o and it is beyond the inversion algorithm's capability to generate a reliable result.

CONCLUSION

Preserving the data fidelity in the prestack gathers, especially the information contained in the far offsets is critical to obtaining a reliable prestack inverted results. The main tasks include 1) mitigating the "hockey stick" using high resolution automatic nonhyperbolic velocity analysis, 2) minimizing the stretch introduced by conventional NMO correction/migration, and 3) improving the SNR by applying proper filters. By combining all of the processing, the proposed workflow maintains the frequency content of wavelets and rejects unwanted random noise through the small- intermediate- and large- angles. Thus the more information is available for subsequent inversion, the more accurate the inverted results. The prestack inverted results based on the new conditioned gathers not only show higher resolution but also exhibit a better match to the original well logs due to critical information contained in the far offset.

ACKNOWLEDGEMENTS

The authors would like to thank Devon Energy in providing the data and CGG in providing the licenses for Hampson-Russell for use in research and education. We also thank the sponsors of Attribute-Assisted Seismic Processing and Interpretation Consortium (AASPI) for their guidance and financial support.

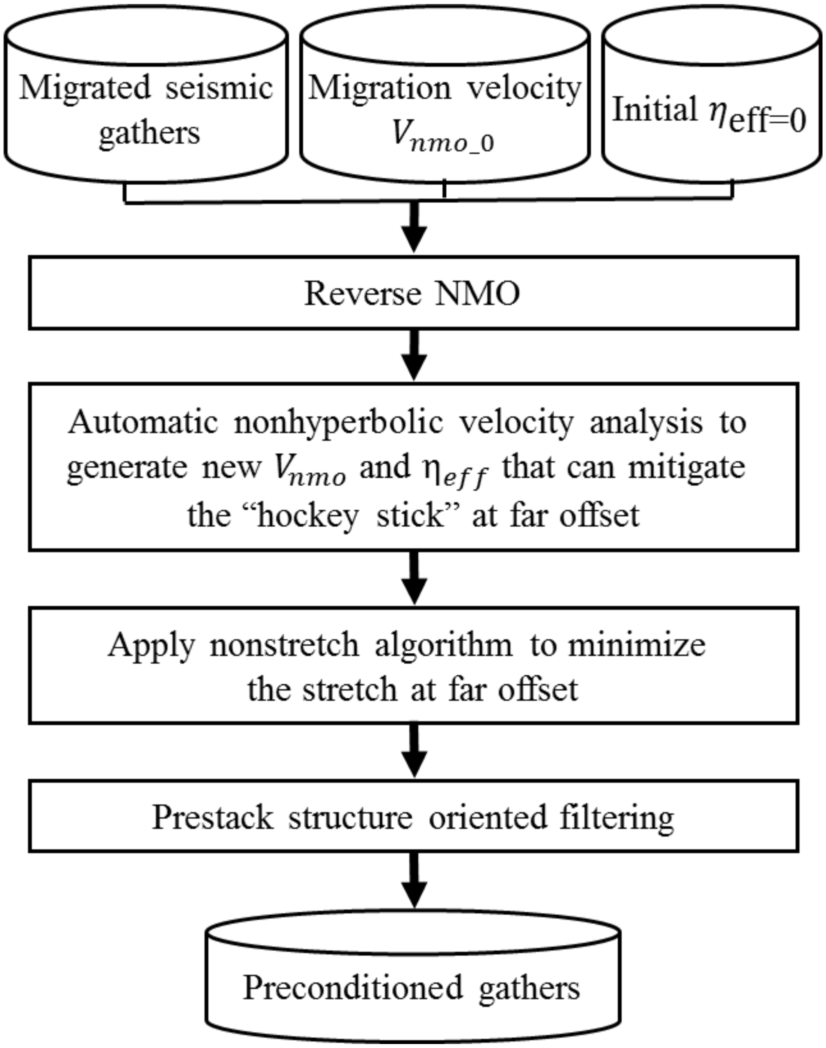

Figure 3.1. Flowchart showing the three data conditioning steps to preserve the data fidelity at far offset: 1) automatic nonhyperbolic velocity analysis, 2) applying anti-stretch processing on the time migrated gathers, and 3) prestack structure oriented filtering.

b)

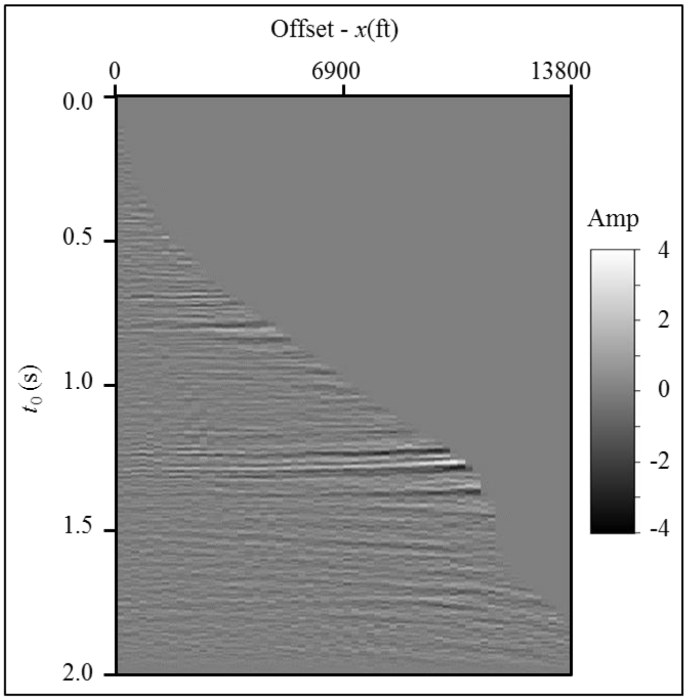
Offset - x(ft)
0
6900
13800
0.0
0.5
1.0
1.5
2.0
t_0 (s)
Amp
4
2
0
-2
-4

a)

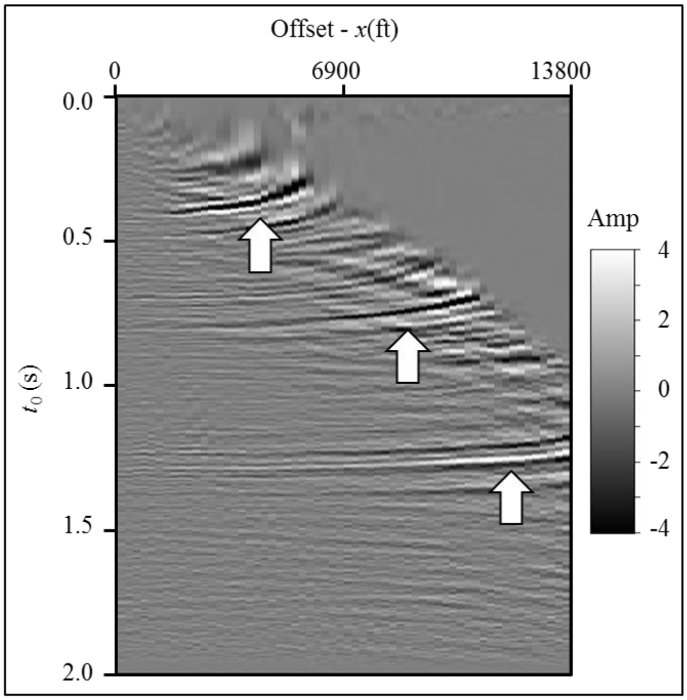
Offset - x(ft)
0
6900
13800
0.0
0.5
1.0
1.5
2.0
t_0 (s)
Amp
4
2
0
-2
-4

c)

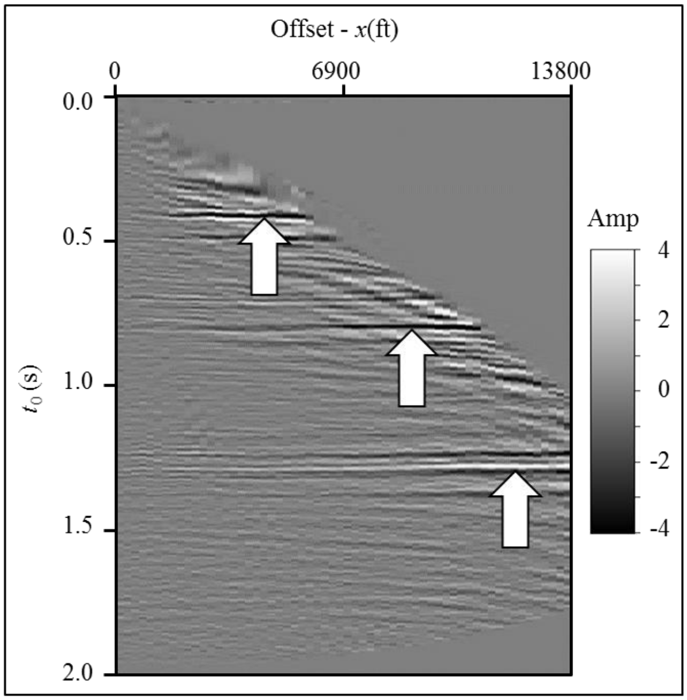
Offset - x(ft)
0
6900
13800
0.0
0.5
1.0
1.5
2.0
t_0 (s)
Amp
4
2
0
-2
-4

d)

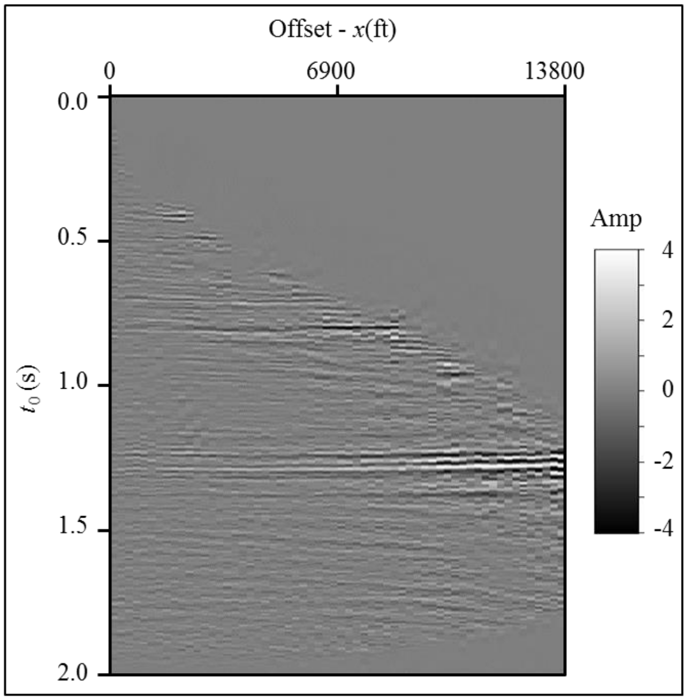
Offset - x(ft)
0
6900
13800
0.0
0.5
1.0
1.5
2.0
t_0 (s)
Amp
4
2
0
-2
-4

e)

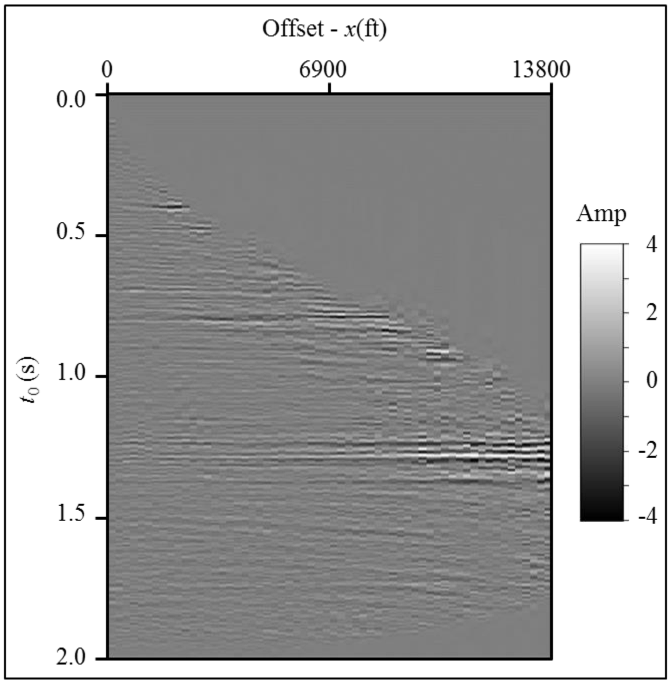

f)

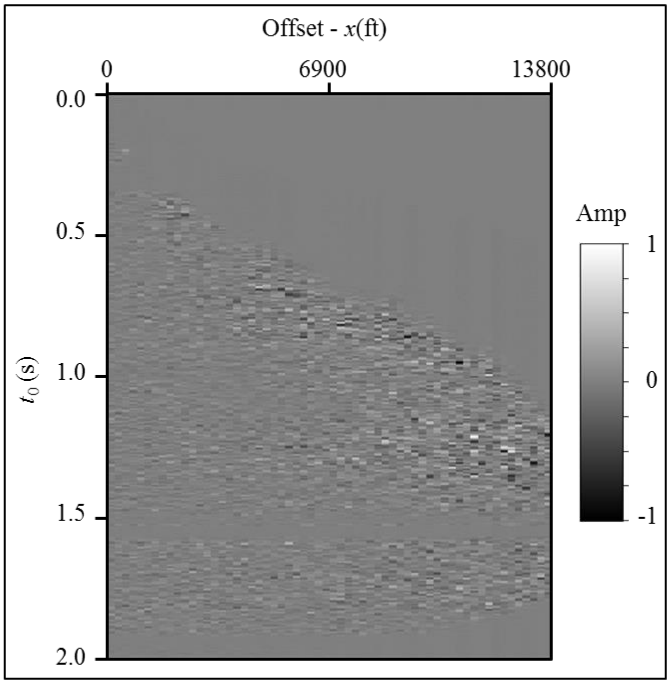

Figure 3.2. Representative gather showing the processing steps shown in Figure 3.1. (a) The time migrated gather from the conventional processing. (b) The same gather after applying 130% stretch mute. (c) The corrected gather using RMS velocity and effective anisotropy obtained from automatic nonhyperbolic velocity analysis. (d) The anti-stretch processing result applied to (a) using the new RMS velocity and effective anisotropy. (e) The SNR improved gather applied to (d) using the prestack structure oriented filter. (f) The rejected random noise.

a)

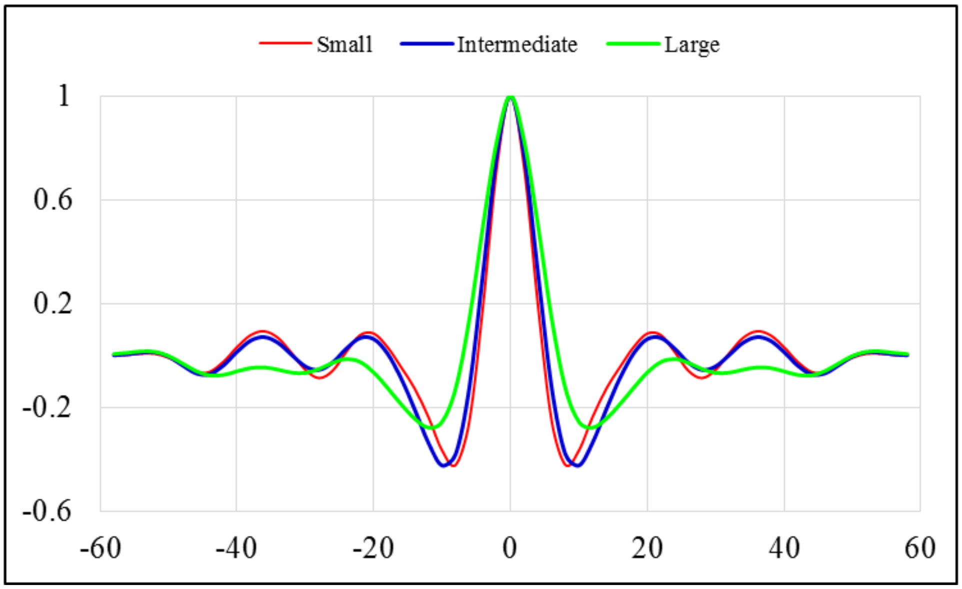
Small
Intermediate
Large
1
0.6
0.2
-0.2
-0.6
-60
-40
-20
0
20
40
60

b)

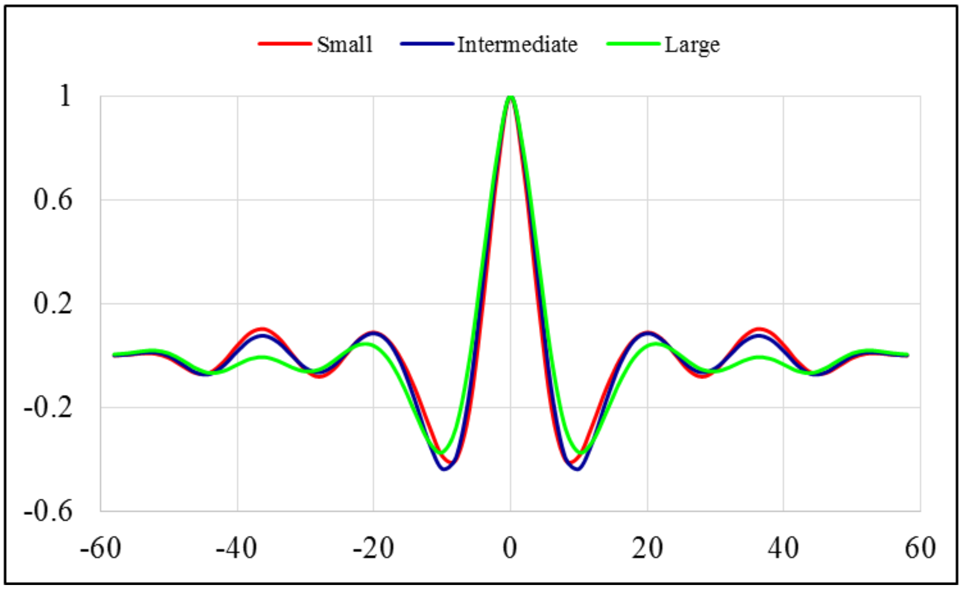
Small
Intermediate
Large
1
0.6
0.2
-0.2
-0.6
-60
-40
-20
0
20
40
60

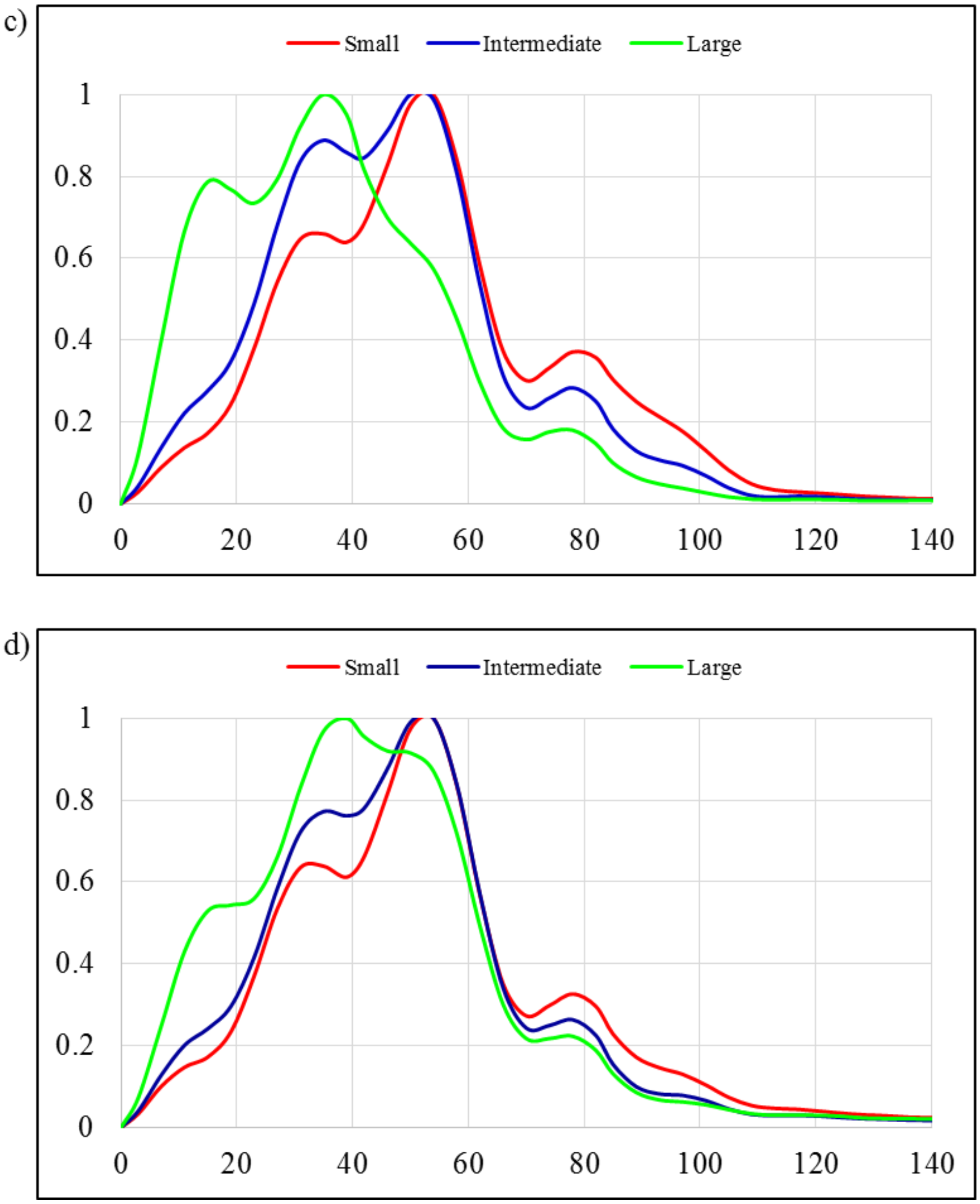

Figure 3.3. Statistical extracted wavelets from (a) the time migrated and (b) the conditioned angle gathers. The corresponding amplitude spectra (c) and (d) of wavelets shown in Figures 3.3a and 3.3b. The red, blue, and green curves indicate the small, intermediate, and large angle wavelets and spectra.

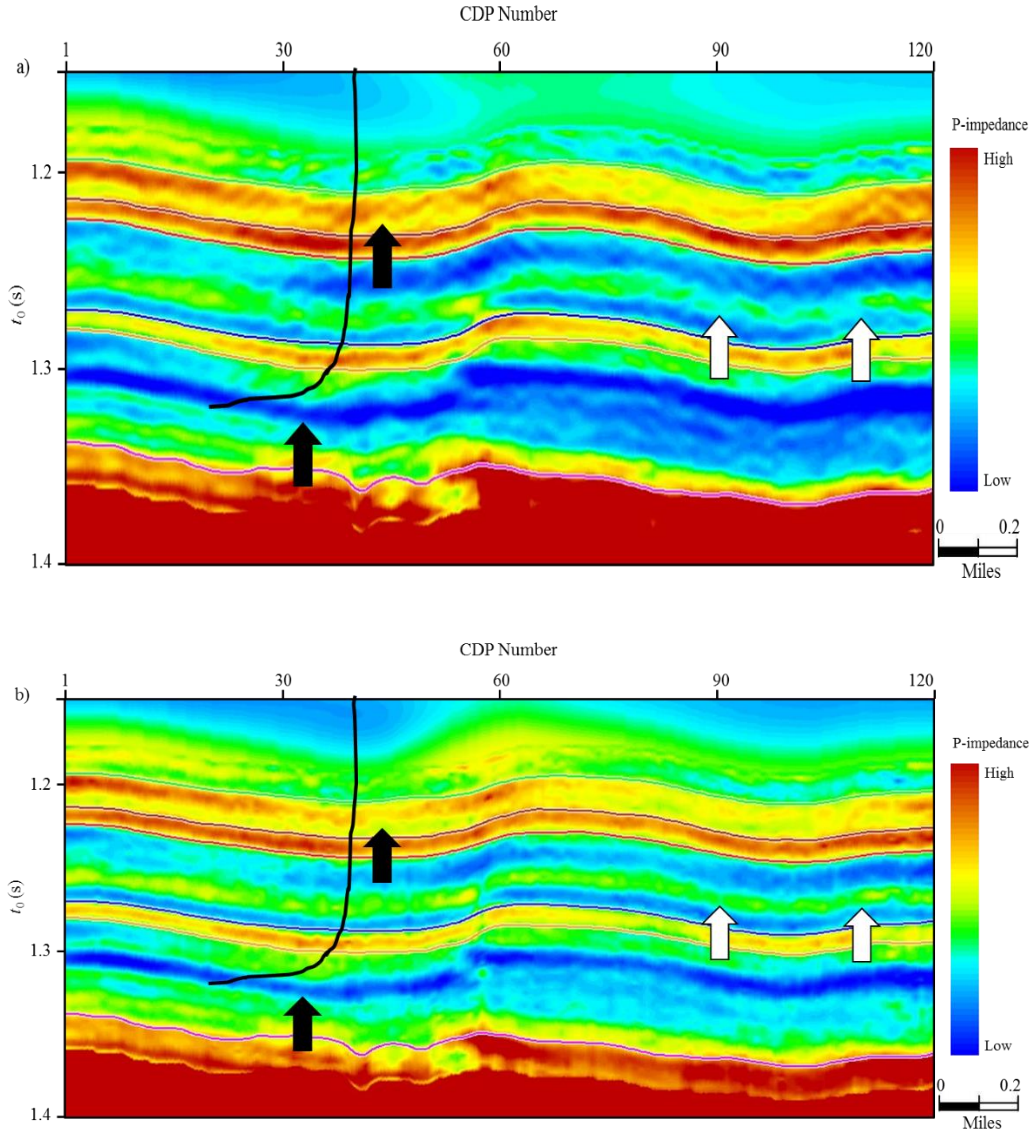

Figure 3.4. Comparison of inverted P-impedance from (a) conventional and (b) preconditioned gathers.

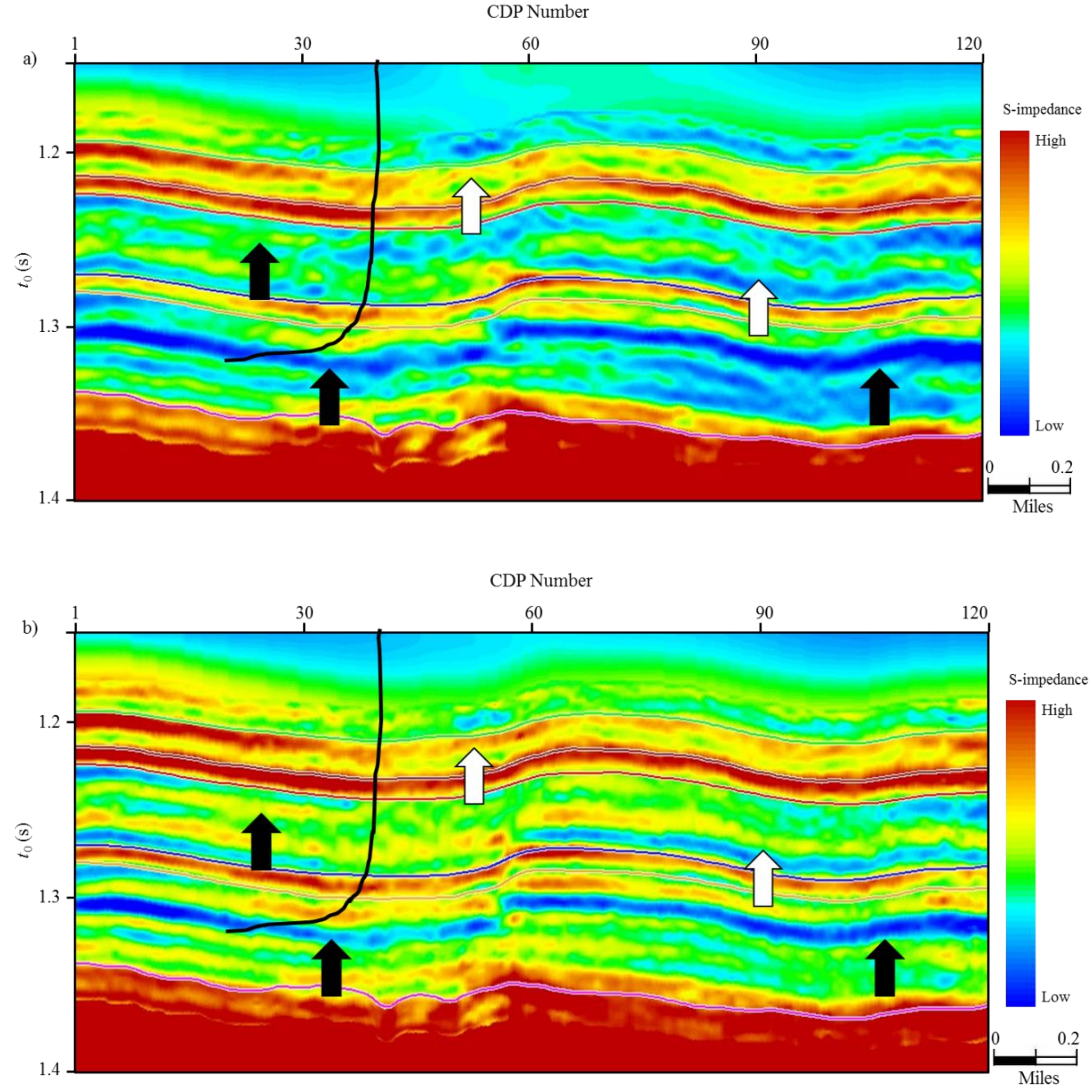

Figure 3.5. Comparison of inverted S-impedance from (a) conventional and (b) preconditioned gathers.

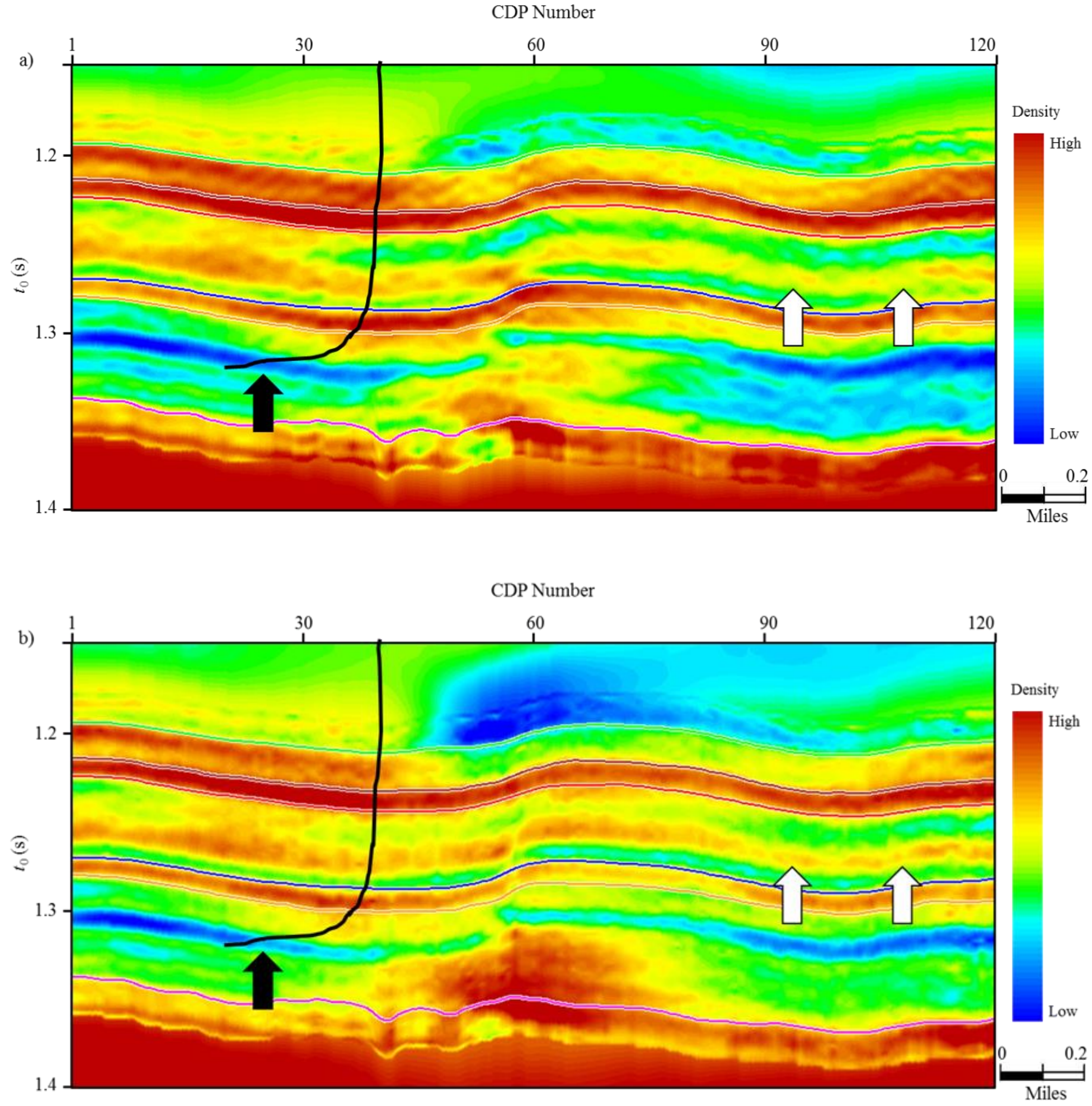

Figure 3.6. Comparison of inverted density form (a) conventional and (b) preconditioned gathers.

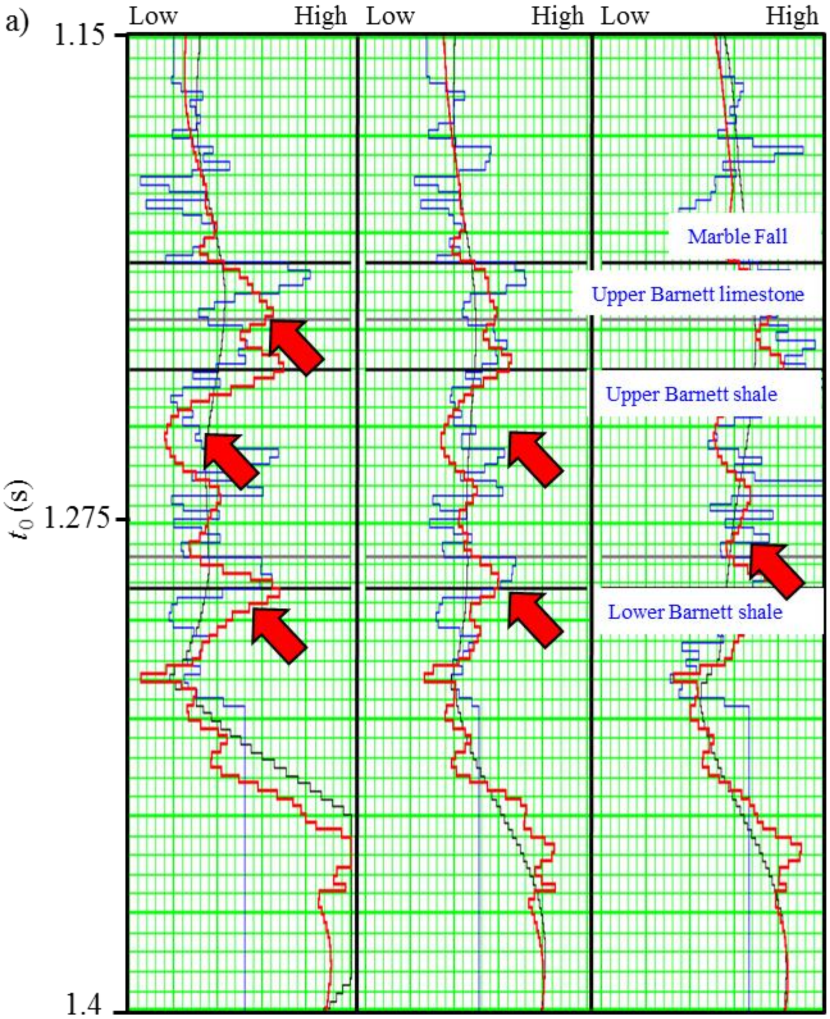
a)
Low
High
Low
High
Low
High
1.15
1.275
1.4
t_0 (s)
Marble Fall
Upper Barnett limestone
Upper Barnett shale
Lower Barnett shale

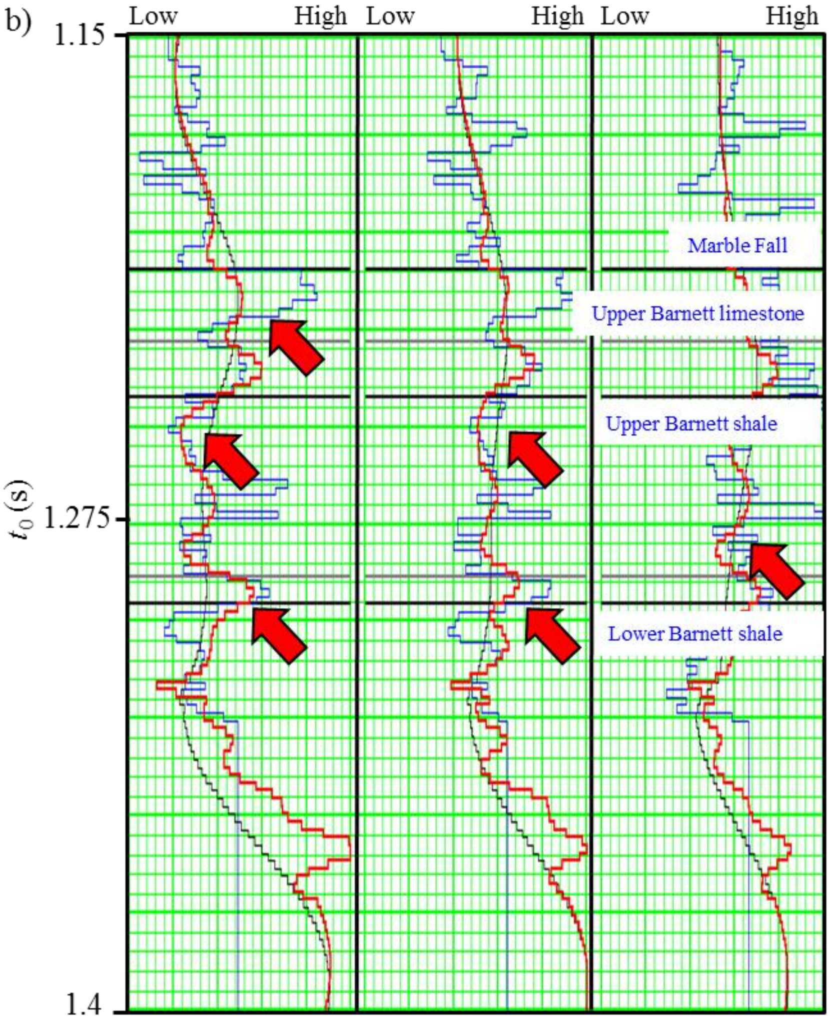

Figure 3.7. Quality control of the inverted results using original well logs. The left, middle, and right panels shows the P-impedance, S-impedance, and density logs. The black, blue, green, and red curves shows the original logs, initial model, and inverted results from conventional and preconditioned gathers.

REFERENCES

Alkhalifah, T., 1997, Seismic data processing in vertically inhomogeneous TI media: Geophysics, **62**, 662-675.

Biondi, 2001, Kirchhoff imaging beyong aliasing: Geophysics, **66**, 654-66.

de Bazelaire, E., 1988, Normal moveout revisited: Inhomogeneous media and curved interfaces: Geophysics, **53**, 143-157.

Fomel, S., and A. Stovas, 2010, Generalized nonhyperbolic moveout approximation: Geophysics, **75**, U9-U18.

Gersztenkorn and Marfurt, 1999, Eigenstructure-based coherence computations as an aid to 3-D structural and stratigraphic mapping, **64**, 1468-1479.

Key, S., and S. B. Smithson, 1990, New approach to seismic-reflection event detection and velocity determination: Geophysics, **55**, 1057-1069.

Marfurt, K. J., 2006, Robust estimates of 3D reflector dip: Geophysics, **71**, P29-P40.

Taner, M. T., and F. Koehler, 1969, Velocity spectra: digital computer derivation and application of velocity functions: Geophysics, **34**, 859-881.

Toldi L.T., 1989, Velocity analysis without picking: Geophysics, **54**, 191-199.

Zhang, B., K. Zhang, S. Guo and K. J. Marfurt, 2013, Nonstretching NMO correction of prestack time-migrated gathers using a matching-pursuit algorithm: Geophysics, **78**, U9-U18.

Zhang, B., T. Zhao, J. Qi, and K. J. Marfurt, 2014, Horizon-based semi-automated nonhyperbolic velocity analysis: Geophysics, under reviewing.

Chapter 4: Brittleness evaluation of resource plays by integrating petrophysics and seismic data analysis

Bo Zhang[1], Tao Zhao[1], Xiaochun Jin[2], and Kurt J. Marfurt[1],

[1]The University of Oklahoma, ConocoPhillips School of Geology and Geophysics,

[2]The University of Oklahoma, the Mewbourne School of Petroleum and Geological Engineering,

This paper has been submitted to the SEG/AAPG journal Interpretation in 2014.

Title: Brittleness evaluation of resource plays by integrating petrophysics and seismic data analysis

ABSTRACT

The main considerations for well planning and hydraulic fracturing in unconventional resources plays include the amount of total organic carbon (TOC) and how much hydrocarbon can be extracted. Brittleness is the direct measurement of a formation about the ability to create avenues for hydrocarbons when suffering to hydraulic fracturing. Brittleness can be directly estimated from laboratory stress-strain measurements, rock properties, and mineral content analysis using petrophysics well logs. However the brittleness from these methods only provides “cylinder” estimates near the borehole. In this paper, we proposed a workflow to estimate brittleness of resource plays in three dimension by integrating the petrophysics and seismic data analysis. The workflow begins by brittleness evaluation using mineral well logs at the borehole location. Then we employ a proximal support vector machine (PSVM) algorithm to construct a classification pattern between rock elastic properties and brittleness from the selected benchmark wells. Then we prestack invert the fidelity preserved seismic gathers to generate a suite of rock properties volumes. Finally, we evaluate the brittleness of target formations by applying the trained classification pattern to the inverted rock properties volumes from seismic data, validating the results to wells not used in the construction of the classification pattern.

INTRODUCTION

Brittleness and ductileness are used to describe deformation behavior under stress. A rock is considered to be ductile if it absorbs a high amount of energy before fracturing. Brittle rocks are unable to accommodate significant strain before fracturing, opening pathways for fluid flow. In conventional reservoirs brittleness is mainly used to evaluate the “drillability” in drilling, “sawability” in rock cutting, and mechanical “winning” of coal rocks (Jin et al., 2014). Brittleness is one of the most important rock parameters in shale reservoirs. Wells completed in brittle rock will develop more fractures. Furthermore, these fractures will close more slowly against the proppant than in more ductile rocks. Thus differentiating brittle from ductile rocks has been the key to archive success in shale gas reservoirs.

The methods of evaluating brittleness of rocks are mainly divided into three categories: (1) direct laboratory stress-strain measurements, (2) mineral content, and (3) empirical methods based on elastic module. Brittleness based on laboratory stress-strain testing (Honda and Sanada, 1956; Hucka and Das, 1974; Altindag, 2010) does not provide a direct link to seismic data. Thus, we concentrate on the last two methods in this paper. In the Barnett Shale, it is widely accepted that brittleness is mainly controlled by quartz content while ductility is related to clay minerals and TOC. Jarvie et al. (2007) proposed a brittleness equation based on the amount of quartz, calcite, and clay minerals where quartz is considered to be the brittle mineral while calcite and clay minerals are regarded to be ductile minerals. Wang and Gale (2009) improved Jarvie’s et al. (2007) equation by considering dolomite as one of the brittle minerals and TOC as one of the ductile mineral. The disadvantage of these two approach is that determination of mineral content requires either core or an elemental capture spectroscopy (ECS) log that are not available for most of wells. Furthermore the brittle-ductile behavior of rock is related to but not fully controlled by the statistical content of brittle minerals. Other factors such as diagenesis and the distribution (such as layering) of mineral may also influence the brittle-ductile behaviors. Rickman et al. (2008) proposed an average brittleness equation based on the elastic parameters of Poisson's ratio and Young's modulus. Their equation assumes that more brittle rocks show relative high Young's modulus and low Poisson's ratio while more ductile rocks exhibit low Young's modulus and high Poisson's ratio. Brittleness estimation based on elastic parameters is more popular in the geomechanics field than that based on mineral content. This is due to the fact that they are easily derived from wire line logs where elastic parameters directly describe rocks ability to fail under stress and maintain an open fracture once the rock fractures (Pickman et al., 2008). Perez (2013) compared brittleness index estimated from mineral content and brittleness average estimated from elastic parameters. He observed inconsistencies between these two methodologies. Therefore he constructed brittleness template based on the Lamda-rho ($\lambda\rho$) and Mu-rho ($\mu\rho$) analysis from selected benchmark wells that had both mineral content (ECS) and rock parameters (sonic, dipole sonic, and density) logs. At last he estimated the brittleness of shale reservoirs by applying his template to inverted $\lambda\rho$ and $\mu\rho$ from prestack seismic inversion. Da Silva (2013) found that the brittleness index (BI) computed from mineral content is positively correlated to $\mu\rho$ and negatively correlated to $\lambda\rho$. Jin et al. (2014) reviewed several based brittleness estimation from geomechanical and petrophysics. They proposed a fracability index equation by considering the elastic parameters and mineral content together where feldspar, mica, as well as the carbonate minerals (limestone, dolomite, and calcite) are regarded as the brittleness contributors. They found a very good correlation between fracability index and mineral content based brittleness evaluation.

Elastic parameters inverted from seismic are commonly used for reservoir characterization after calibration with well logs. The accuracy of elastic parameters derived from seismic inversion mainly depends on whether we can preserve the data fidelity at far offsets in the prestack gathers. Stretch and “hockey sticks” are the two main factors that affect the data fidelity at far offset. We apply a workflow to mitigate these two phenomena at far offset (Zhang et al., 2014) beginning by mitigating the “hockey stick” using automatic nonhyperbolic velocity and followed by a wavelet based correction to minimize the stretch at far offset. Zhang et al. (2014) found that inverted results from conditioned gathers have better resolution and higher correlation coefficients with well logs.

In this paper, we propose a workflow to evaluate the brittleness of shale reservoirs by integrating petrophysics and seismic analysis. By employing a supervised classification algorithm, we obtain a classification pattern between multiple rock elastic properties and BI computed from mineral logs for the benchmark well. We then obtain the rock elastic properties volumes by performing prestack inversion on the fidelity preserved gathers. Finally, we evaluate the brittleness of target reservoirs by applying the classification pattern to the inverted rock properties volumes.

BRITTLENESS DEFINITION

Brittleness is used to describe the deformation behavior when the rocks are subject to stress in the laboratory. The brittleness index (BI) is commonly used to evaluate the degree of brittleness of rocks. The higher the magnitude of BI, the more brittle of the rock. One common BI measurement is the ratio of compressive strength, σ_c to tensile strength σ_t (Coates and Parsons, 1966):

$$BI = \frac{\sigma_c}{\sigma_t}. \tag{1}$$

However BI measurements based on compressive strength and tensile strength are only available in the laboratory. In practice it is expensive and therefore unrealistic to extract reservoir cores for all wells, limiting the use of such direct measurements to reservoir characterization. Several researchers have proposed BI definitions based on either mineral content logs or on rock elastic parameters for reservoir characterization. Jarvie et al. (2007) and Wang and Gale (2009) proposed BI definitions based on mineral content of rocks. They first classified the minerals as ductile or brittle by considering their deformation behavior. Then they computed BI as the ratio of the brittle mineral content to the sum of constituent minerals. Jarvie et al. (2007) considered quartz as the brittle mineral:

$$BI_J = \frac{Qz}{Qz + Cal + Cly}. \tag{2}$$

Wang and Gale (2009) further improved Jarvie's definition by including dolomite as a brittle mineral and TOC as a ductile component

$$BI_W = \frac{Qz + Dol}{Qz + Cal + TOC + Cly + Dol} \tag{3}$$

where Qz is the fractional quartz content, Dol is the dolomite content, Cal is the calcite content, TOC is the total organic carbon content, and Cly is the clay content by weight in the rock.

Rickman et al. (2008) proposed a brittleness average estimation using Young's Modulus E and Poisson's ratio σ.

$$BI = \frac{E_n + \sigma_n}{2}, \qquad (4)$$

where E_n and σ are the normalized Young's Modulus and Poisson's Ratio

$$E_n = \frac{E_{\max} - E}{E_{\max} - E_{\min}}, \qquad (5)$$

$$\sigma_n = \frac{\sigma - \sigma_{\max}}{\sigma_{\max} - \sigma_{\min}}, \qquad (6)$$

where E_{max}, E_{min} are maximum and minimum Young's Modulus; σ_{max}, σ_{min} are the maximum and minimum Poisson's Ratio.

The BI evaluation based on mineral content is widely used for shale reservoir characterization. Unfortunately it is expensive to obtain the mineral content logs and this evaluation is only available for the formations at the borehole location. While it is easier and cheaper to compute the average brittleness but it fails when there are limestone stringers (Perez, 2013). In this paper we employ Wang and Gale's (2009) definition to evaluate the brittleness of formations.

PRESTACK SEISMIC DATA CONDITIONING

Simultaneous prestack seismic inversion provides a 3D estimation of reservoir properties such as acoustic impedance (Z_P), shear impedance (Z_S), and density (ρ). These estimates represent intrinsic rock properties and are commonly used to predict fluid, lithology, and geomechanical properties (Goodway et al., 1997). The reliability of inverted results increases with increasing angle of incidence. However information contained in the far offsets (large incidence angle) are usually distorted to some extent after conventional processing. Thus preserving the data fidelity in prestack seismic gathers is one of the key factors to obtain reliable estimations of Z_P, Z_S, and ρ. The main factors that affects the data fidelity in the prestack gathers include 1) “hockey sticks” at far offset in the long offset seismic surveys, 2) NMO/migration stretch, and 3) random noise. To use the critical information contained in the long offset data for prestack inversion, we need to 1) flatten the reflections at far offset using a proper nonhyperbolic travel time equation, 2) minimize the stretch typically associated with far offset, and 3) improve the signal-to-noise ratio (SNR) by prestack structure oriented filtering (PSOF).

Figure 4.1 summarizes the workflow for preserving the data fidelity contained in the far offset. Our input data consist of prestack time migrated gathers and the initial migration velocity $V_{\mathrm{nmo\_0}}$. The initial effective anisotropy η_{eff} is set to 0. We obtain the initial migration velocity by performing hyperbolic velocity analysis on coarse grid super gathers. The workflow begins by performing reverse NMO on the time migrated gathers using the initial migration velocity. Then we obtain the optimal velocity and anellipticity model using our automatic algorithm (Zhang et al., 2014). Next we apply nonstretch NMO correction (Zhang et al., 2013) to the time migrated gathers using new velocity and anellipticity model resulting in flattened nonstretched prestack gathers. Lastly we apply PSOF algorithm to further improve the SNR. In this manner, both stacking power and vertical resolution are improved first by aligning the data and second by avoiding stretch.

BRITTLENESS EVALUAITON BY INTEGRATING PETROPHYSICS AND SEISMIC DATA ANALYSIS

BI estimation based on mineral logs is widely used to evaluate the brittleness of resources plays reservoirs (Jarvie et al., 2007; Wang and Gale, 2009). However, mineral content logs are expensive to acquire, therefore limiting direct brittleness estimates to only a few wells. Different minerals exhibit different rock elastic properties such as acoustic impedance, shear impedance, Poisson's ratio (σ), incompressibility lambda (λ), and shear modulus mu (μ). For example λ of quartz is lower than those of clay and calcite, while the μ of quartz is higher than those of clay and calcite (Mavko et al., 2009). This observation of elastic properties to minerals provides a mean to evaluate the brittleness of resource play by multiple rock elastic properties analysis (Goodway et al., 1997; Perez, 2013; Da Silva, 2013). In this paper we employ an advanced classification algorithm named proximal support vector machine (PSVM) (Fung and Mangasarian, 2001) to find the pattern between multiple rock properties and BI. PSVM is a supervised learning procedure which uses associated learning algorithms to analyze data and recognize patterns. It is widely used for classification and regression analysis (Fung and Mangasarian, 2005). The details of PSVM are described in Appendix A.

We proposed a workflow of Figure 4.2 to obtain a 3D brittleness estimates for resource plays by integrating petrophysics and seismic data. Our workflow contains two parts 1) obtaining the classification pattern between elastic properties and BI, and 2) applying the recognized pattern to the elastic volumes from seismic data to generate a BI volume. Our algorithm starts by computing rock elastic properties from sonic and density logs and BI from mineral content logs. Next we obtain a classification pattern between these elastic properties and BI by performing PSVM training on randomly selected well log samples (the training subset). The recognized pattern is then tested on the remaining well log samples (the testing subset) to validate the mapping. The seismic inversion begins by applying PSOF (Figure 4.1). Then we obtain the 3D elastic property volumes by performing simultaneous prestack inversion using commercial software. Finally, we generate a 3D brittleness estimates for the target reservoir by applying the recognized PSVM pattern to the inverted elastic properties volumes.

APPLICATION

The Barnett Shale of Fort Worth Basin (FWB), TX, USA is one of the largest unconventional shale reservoirs in the world. The FWB is a foreland basin and covers approximately 54000 mi^2 in north-central Texas (Da Silva, 2013). A high quality long offset surface seismic survey (Figure 4.3) was acquired in 1990s over “core” production area of FWB. In our survey, the Barnett Shale formation lies between 1.2 s and 1.4 s. The maximum offset is around 14000 ft while the target Barnett Shale lies at approximately 7000 ft depth. Well A, which lies approximately 5 miles to the northeast of seismic survey (Figure 4.3), serves as the bench mark well to build the classification pattern between selected elastic properties and BI.

Classification training between rock properties and BI for the benchmark well

Figure 4.4 illustrates gamma ray, percent weight clay, percent weight TOC, percent weight quartz, percent weight calcite and BI logs computed using equation 3 for well A. Note that zones with high quartz content are more brittle than zones with high clay, calcite, and TOC content which are less brittle. Figure 4.4 also shows that the shale formation (Upper and Lower Barnett Shale) exhibits moderate to high brittleness index values while the limestone formations (Marble Falls Limestone, Forestburg Limestone, and Viola Limestone) show low GR and low BI values. Considering the reliability of inverted rock properties from seismic inversion, we choose Z_P, Z_S, σ, and μ/λ as the elastic properties (Figure 4.5) used in training with BI. First we break the continuous BI logs into 10 equal petro-type to obtain a normalize BI (BI_N) (Figure 4.6). Next we assign a value between 1 and 10 to BI_N corresponding to its petro-type number. The sixth track in Figure 4.6 shows the normalized results. A rating of 1 denotes the most ductile rock while a rate of 10 denotes the most brittle rock. Figure 4.5 illustrates a positive correlation between μ/λ and BI_N. We also observe a negative correlation between σ and BI_N. Then we randomly select 30% of total samples as the training subset used in PSVM classification. The remaining 70% samples are used as the testing subset to validate our classification pattern. The seventh track in Figure 4.5 shows the new classified BI (BI_C) logs by applying the classification pattern on selected rock properties. Note the strong agreement between the original normalized (the sixth track in Figure 4.5) and new classified BI (the seventh track in Figure 4.5). We obtain a very high correlation coefficient (0.9) between original and new BI logs.

Simultaneous prestack inversion and 3D brittleness evaluation

P-impedance is the most reliable result from prestack inversion. S-impedance estimation become reliable when the incidence angle reaches 30^o, while density become reliable when the angle approaches to 45^o). The maximum incident angle of our prestack gathers used for inversion is approximate 36^o in our survey. Thus preserving the fidelity of far offset data is one of the main targets in processing and is the key to obtain reliable estimation of rock properties form prestack seismic inversion. Figure 4.7a shows a representative time-migrated CMP gather using a two term hyperbolic travel time equation. Note the “hockey sticks” and stretch indicated by the white arrows at far offsets. The “hockey sticks” blur the reflection events while the stretch lowers the resolution in the stacked volume. Usually, seriously stretched data are muted out based on a user-defined muting criterion. However muting the far offset data rejects the critical information contained in the far offset. Figure 4.7b shows the flattened nonstretch gather. Note that the “hockey sticks” and stretch at far offset are gone when compared to the original time-migrated gather. Figures 4.6c and d show the same gather after applying PSOF and the rejected noise, respectively. Figure 4.7d illustrates that the noise rejected by PSOF is incoherent noise. By applying the pre-conditioning workflow (Figure 4.1), more far offset data (Figure 4.7c) are available for the subsequent processing and inversion.

We use eight wells located in our seismic survey for prestack seismic inversion. All the wells have P-wave sonic and density logs. S-wave sonic logs are available for three of the wells. By using a nonlinear regression, we derive S-wave sonic logs for other wells using P-wave sonic. First, six interpreted horizons and eight wells are used to build the background P-impedance, S-impedance and density models. Next we apply simultaneous prestack inversion to the conditioned gathers (Figure 4.7c) to obtain rock properties. The inversion window ranges from 50 ms above the first horizon (Marble Falls limestone) to 50 ms below the last horizons (Viola limestone). Figures 4.8a, 4.8b, 4.8c, and 4.8d show the inverted P-impedance, S-impedance, Poisson’s ratio, and Mu-Lambda ratio, respectively. The vertical black curves in figures are the well tract that used for quality control of the inverted results (Figure 4.9). The first, second, third, and fourth tracks in Figure 4.9 show the comparison of P-, S- impedance, density, and Poisson’s ratio. The blue, black, and red curves are respectively the original logs, initial model, and inverted results from the prestack seismic gathers. Note that the inverted results from seismic do not have the high vertical resolution of the well logs, but they bear an excellent trend matching with the initial low frequency models derived from well logs at the seismic scale. Figure 4.10 shows the predicted brittleness by applying the classification trained from the benchmark well to the inverted rock properties. Note that the Upper and Lower Barnett Shale are generally more brittle than limestone which agree with the conclusions derived from well data analysis. The brittleness degree varies horizontally within the Upper and Lower Barnett Shale formation. Figure 4.9 also shows that a ductile zone exist in the Upper Barnett Shale and the brittle zone in Lower Barnett Shale is more continuous than that of Upper Barnett Shale. This phenomenon indicates that Lower Barnett Shale may more easily produce factures than the Upper Barnett Shale when completed with hydraulic fracturing. Microseismic data (Perez, 2013) indicate that the amount of microseismic events happened in Lower Barnett Shale is much larger than that in the Upper Barnett Shale.

CONCLUSION

The proposed workflow provides a 3D Brittleness estimates for unconventional resource plays by integrating petrophysics and seismic data analysis. The key algorithm of this workflow is to obtain the classification pattern between rock elastic properties that can be estimated from surface seismic data and BI from petrophysical data. The prestack seismic data conditioning preserve more far offset data for seismic data and improve the reliability of the inverted rock elastic parameters. The increasing reliability of inverted results further stabilize the brittleness estimation of reservoirs when applying the classification pattern on inverted rock properties volumes.

ACKNOWLEDGEMENTS

The authors would like to thank Devon Energy in providing the data and CGG for providing the license for Hampson-Russell. We also thank the sponsors of Attribute-Assisted Seismic Processing and Interpretation Consortium (AASPI) for their guidance and financial support.

APPENDIX A

The proximal support vector machine (PSVM) used in this paper was initially proposed by Fung and Mangasarian (2005). The algorithm of PSVM is an evolutionary variant of support vector machine algorithm (SVM) (Cortes and Vapnik, 1995). The SVM is a powerful supervised machine learning technique widely used in text detection, image recognition and protein classification. It has been found that PSVM provides comparable classification correctness to standard SVM but at considerable computational savings (Fung and Mangasarian, 2005; Mangasarian and Wild, 2006). We show a binary (two cluster) classification problem in this appendix for simplicity.

The PSVM decision is defined as

$$\boldsymbol{x}^T\boldsymbol{\omega} - \gamma \begin{cases} > 0 & \boldsymbol{x} \in A^+ \\ = 0 & \boldsymbol{x} \in A^+ \ or \ A^- \\ < 0 & \boldsymbol{x} \in A^- \ , \end{cases} \tag{A1}$$

where $\boldsymbol{x} \in R^{\boldsymbol{n}}$ is a n dimensional vector data point that needs to be classified, T denotes the vector transpose, $\boldsymbol{\omega} \in R^{\boldsymbol{n}}$ implicitly defines the normal vector to the decision-boundary, $\gamma \in R$ defines the location of the decision-boundary, and A^+ and A^- are two classes of the binary classification. We estimate $\boldsymbol{\omega}$ and γ by solving the following constrained optimization problem by using the training sample set (Fung and Mangasarian, 2005):

$$\min_{\boldsymbol{\omega},\gamma,\boldsymbol{y}} \nu \frac{1}{2} \|\boldsymbol{y}\|^2 + \frac{1}{2}(\boldsymbol{\omega}^T\boldsymbol{\omega} + \gamma^2), \tag{A2}$$

subject to

$$\boldsymbol{D}(\boldsymbol{A\omega} - \boldsymbol{e}\gamma) + \boldsymbol{y} = \boldsymbol{e}, \tag{A3}$$

where $\boldsymbol{A} \in R^{m\times n}$ is the sample matrix composed of m samples which can be divided into two classes, A^+ and A^-. $\boldsymbol{A}$ was used for supervised training to obtain $\boldsymbol{\omega}$ and γ; $\boldsymbol{y} \in R^m$ is the training error vector; $\boldsymbol{D} \in R^{m\times m}$ is a diagonal matrix of labels with a diagonal composed of $+1$ for A^{+} and -1 for A^{-} , ν is a non-negative parameter, and $\boldsymbol{e} \in R^{m}$ is a column vector of ones. This optimization problem can be solved by using a Lagrangian multiplier (Fung and Mangasarian, 2005). If we employ the Gaussian kernel function, then the decision condition for the testing samples can be expressed as

$$\boldsymbol{K}(\boldsymbol{x}^{T},\boldsymbol{A}^{T})\boldsymbol{Du}-\gamma\begin{cases} >0 & \boldsymbol{x} \in A^{+} \\ =0 & \boldsymbol{x} \in A^{+}\ or\ \ A^{-} \\ <0 & \boldsymbol{x} \in A^{-}\ , \end{cases} \qquad \text{(A4)}$$

where

$$\boldsymbol{K}(\boldsymbol{x}',\boldsymbol{A}')_{ij} = \exp(-\sigma\|\boldsymbol{x}-\boldsymbol{A}'_{i\cdot}\|^{2})\,, i \in [1,m]. \qquad \text{(A5)}$$

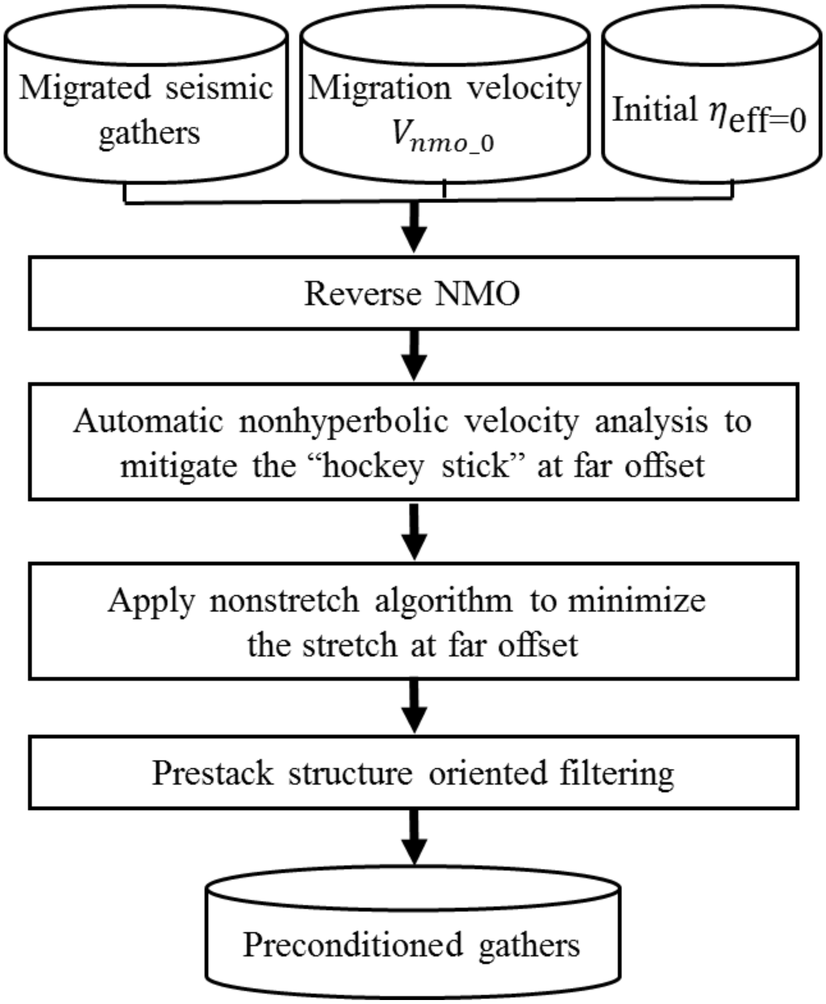

Figure 4.1. Flowchart showing steps to preserve the data fidelity at far offset. It contains three main steps 1) automatic nonhyperbolic velocity analysis, 2) applying anti-stretch processing on the time migrated gathers, 3) prestack structure oriented filtering.

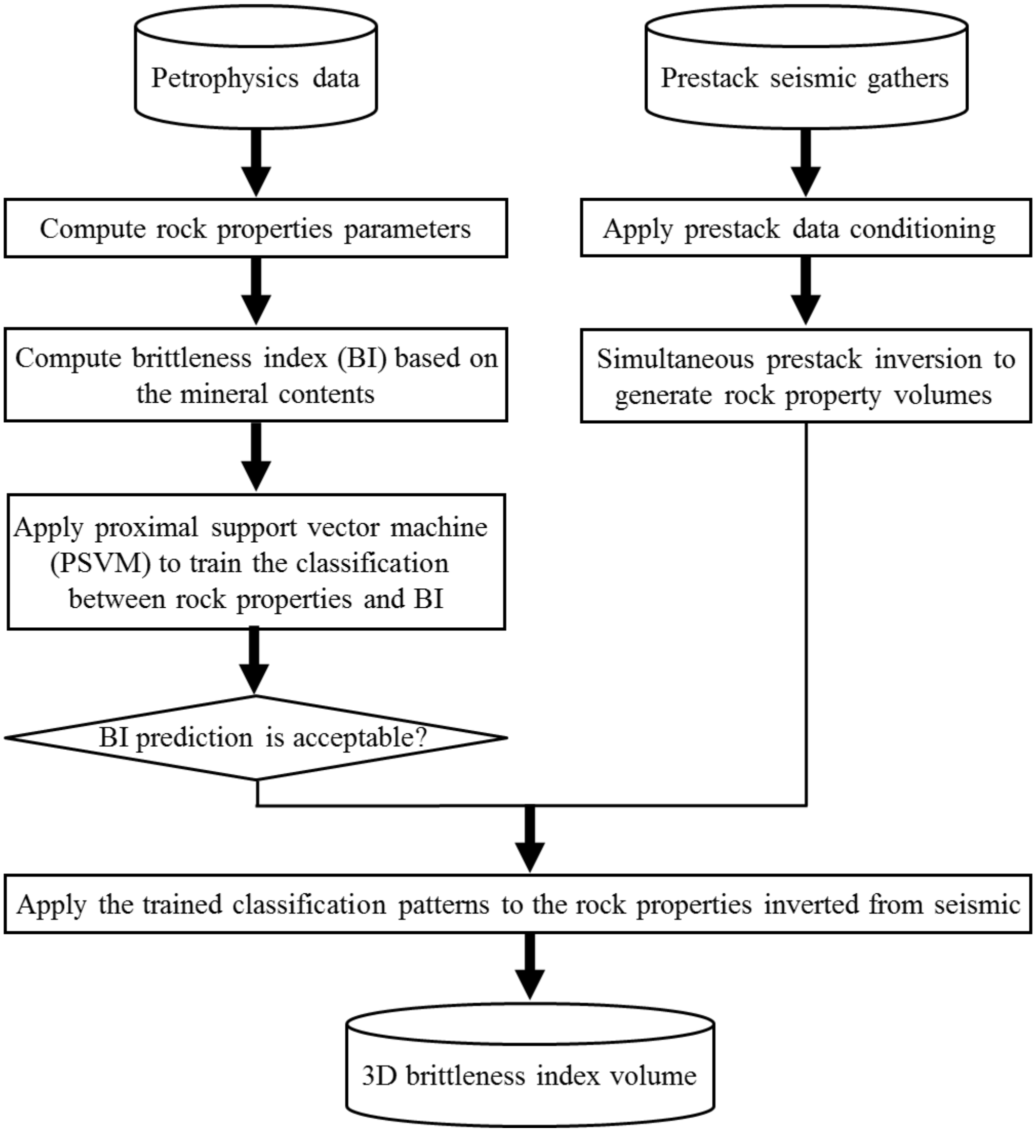

Figure 4.2. Flowchart showing steps to estimate the brittleness of resources reservoirs containing two main parts 1) obtaining the classification pattern between rock properties and BI from bench mark wells and 2) inverting rock parameters from seismic and obtain 3D BI by applying the classification pattern on inverted volumes.

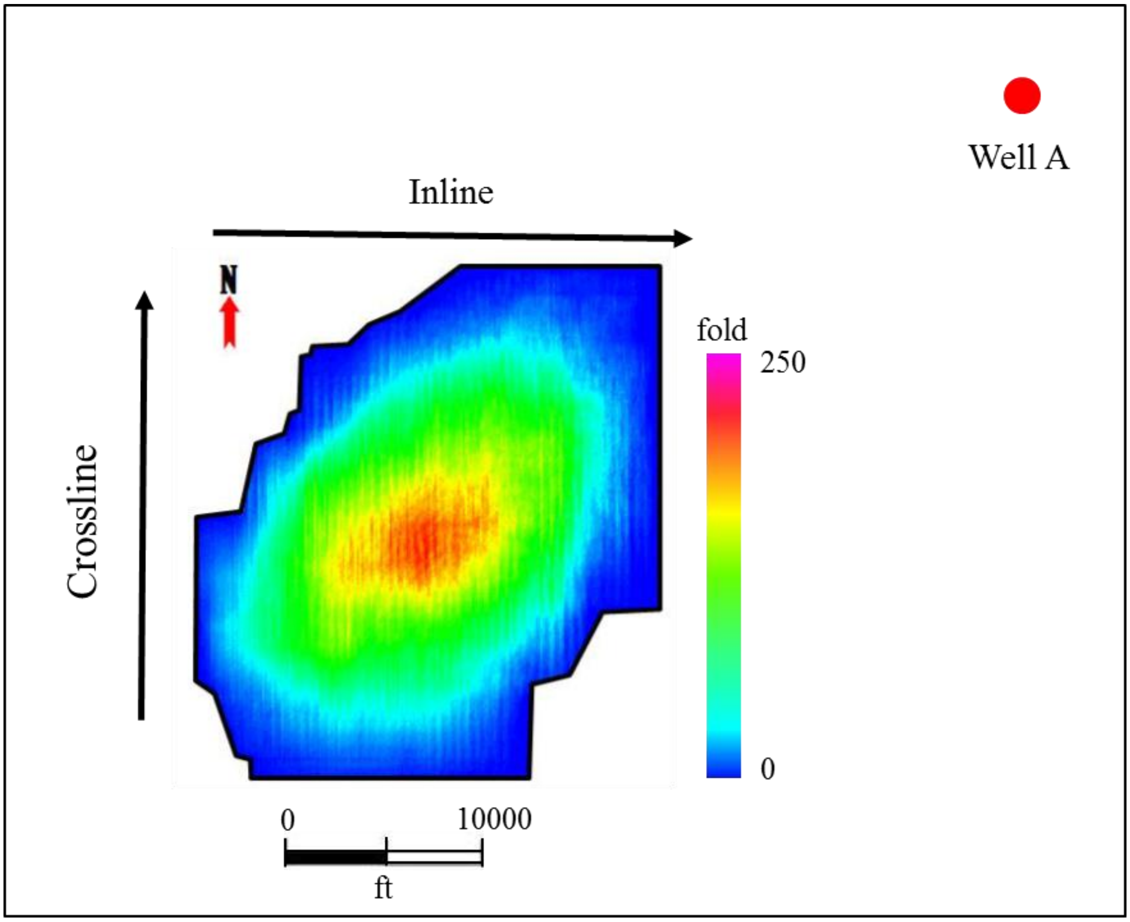

Figure 4.3. Outline of seismic survey located in Wise County including the fold map resulting from 3D seismic acquisition. Survey boundaries are highlighted in black and the bench mark well used in this paper is located approximately 5 miles to the northeast of seismic survey.

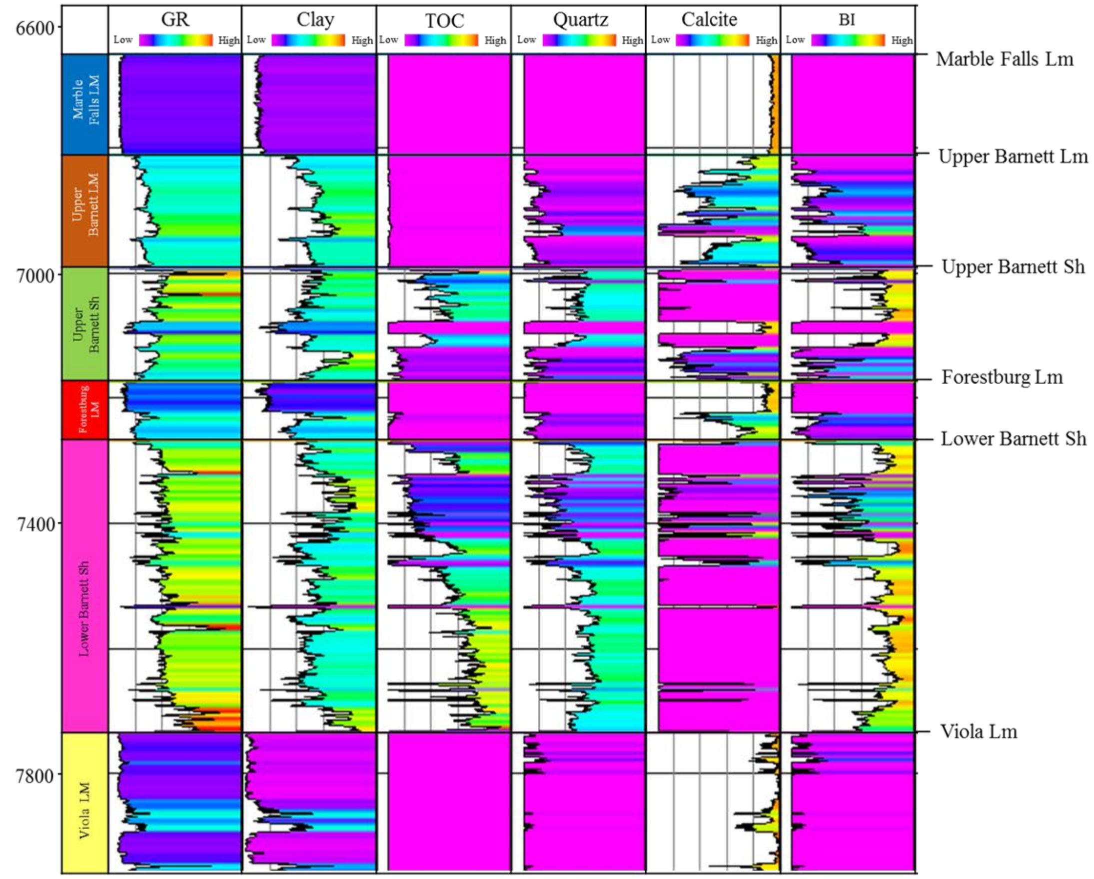

Figure 4.4. Gamma Ray, clay mineral, TOC, quartz mineral, calcite mineral, and brittleness index logs corresponding to Well A. Brittleness index values were calculated using Wang and Gale's equation (2009).

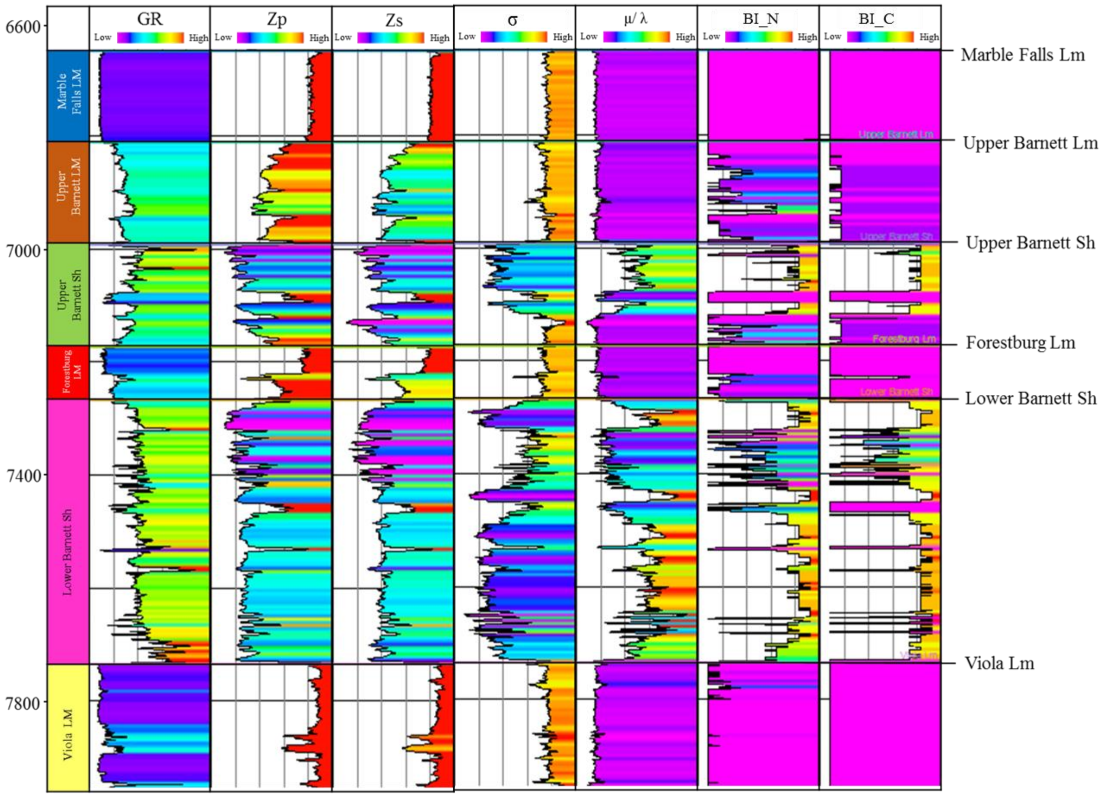

Figure 4.5. Gamma Ray, P- and S- impedance, Possion's ratio, Mu-Lambda ratio, normalized BI and new classified BI corresponding to Well A.

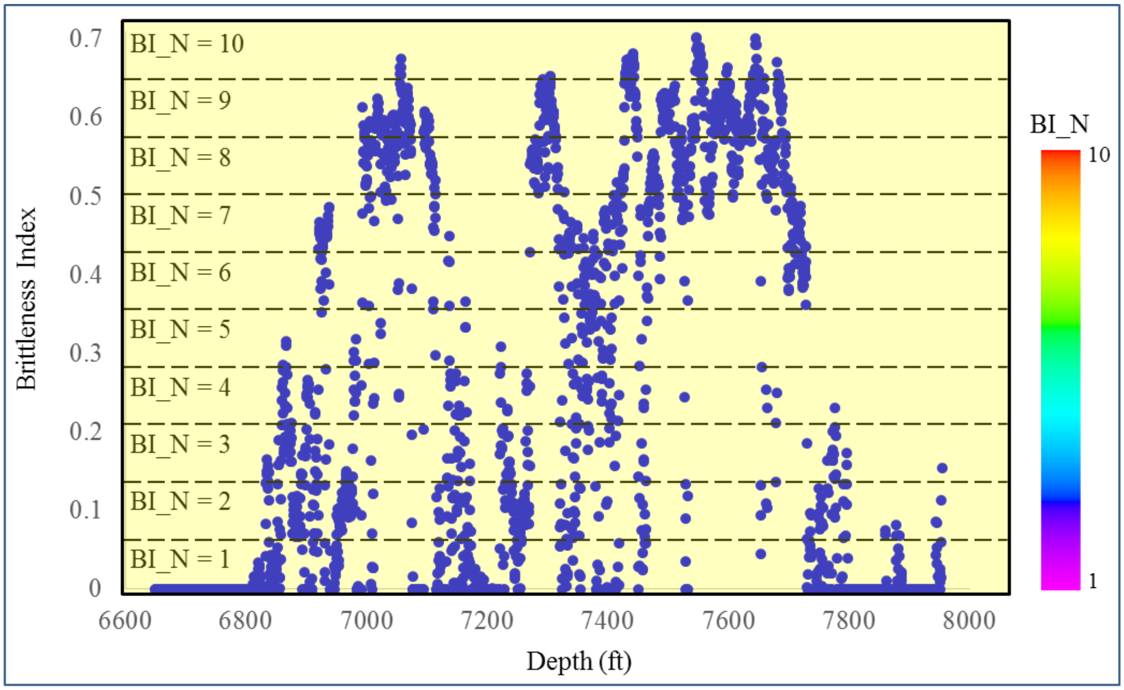

Figure 4.6. Cartoon illustrating the strategy to normalize the BI logs computed from mineral content using Wang and Gale's equation (2009).

a)

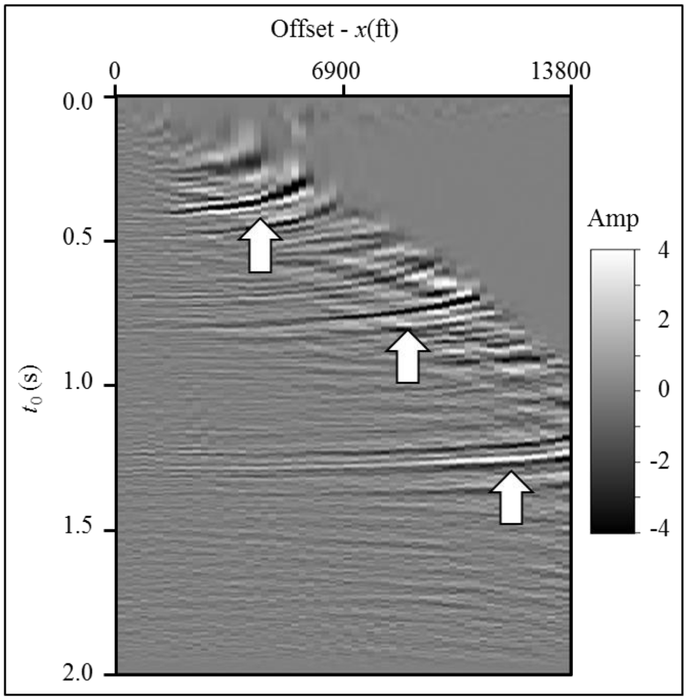
Offset - x(ft)
0
6900
13800
0.0
0.5
1.0
1.5
2.0
t0 (s)
Amp
4
2
0
-2
-4

b)

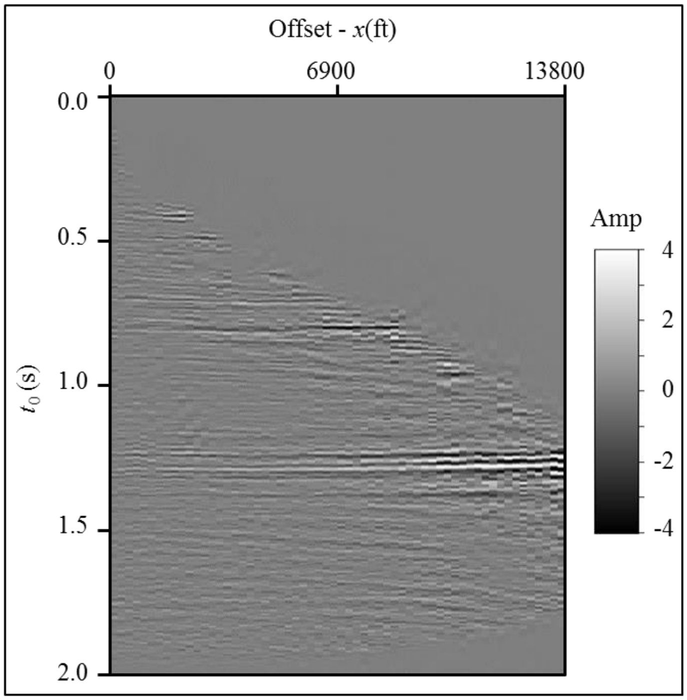
Offset - x(ft)
0
6900
13800
0.0
0.5
1.0
1.5
2.0
t0 (s)
Amp
4
2
0
-2
-4

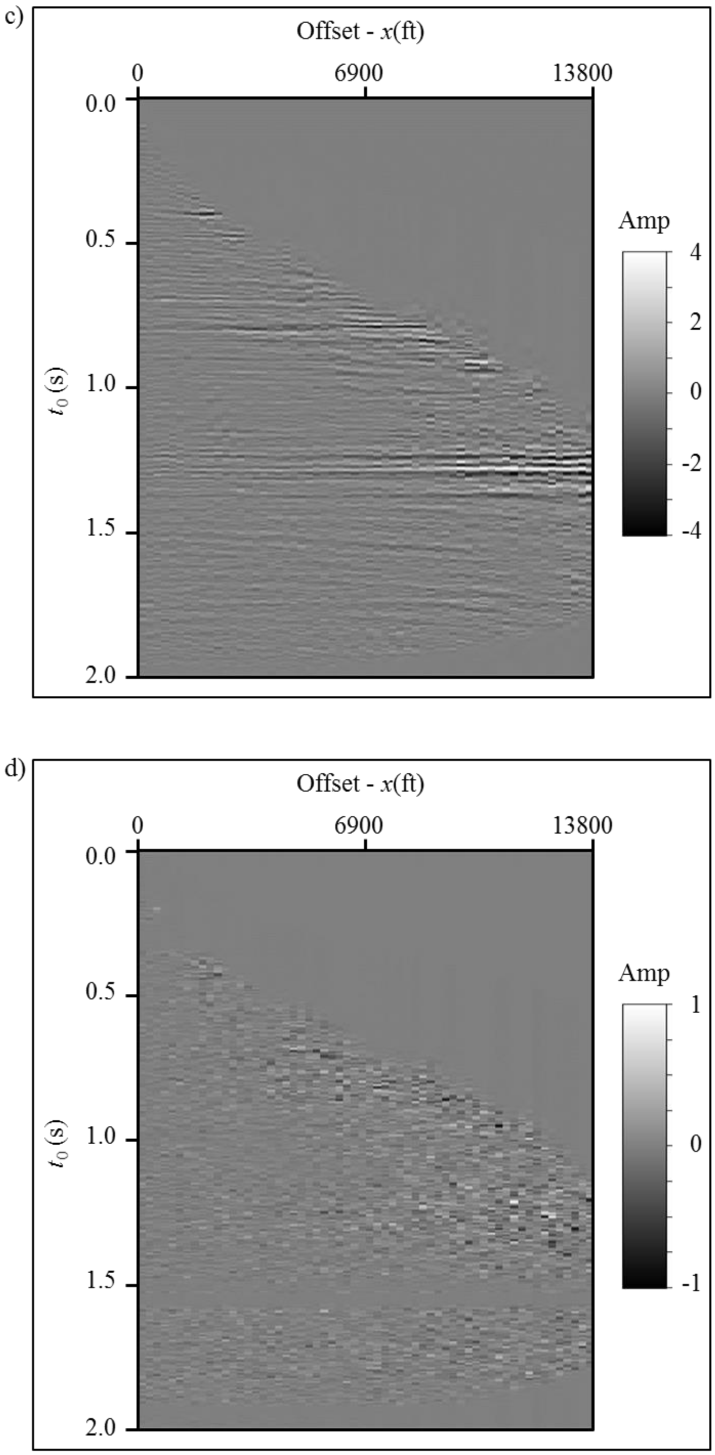

Figure 4.7. Representative gather showing the processing steps shown in Figure 4.1. Normally, we need to mute the serious stretch appearing at far offset in (a) the time migrated gather in the conventional processing. (b) The stretch free and flattened gather after applying automatic nonhyperbolic velocity analysis and anti-stretching processing. (c) The SNR improved gather applied to (c) using the prestack structure oriented filter. (d) The rejected noise.

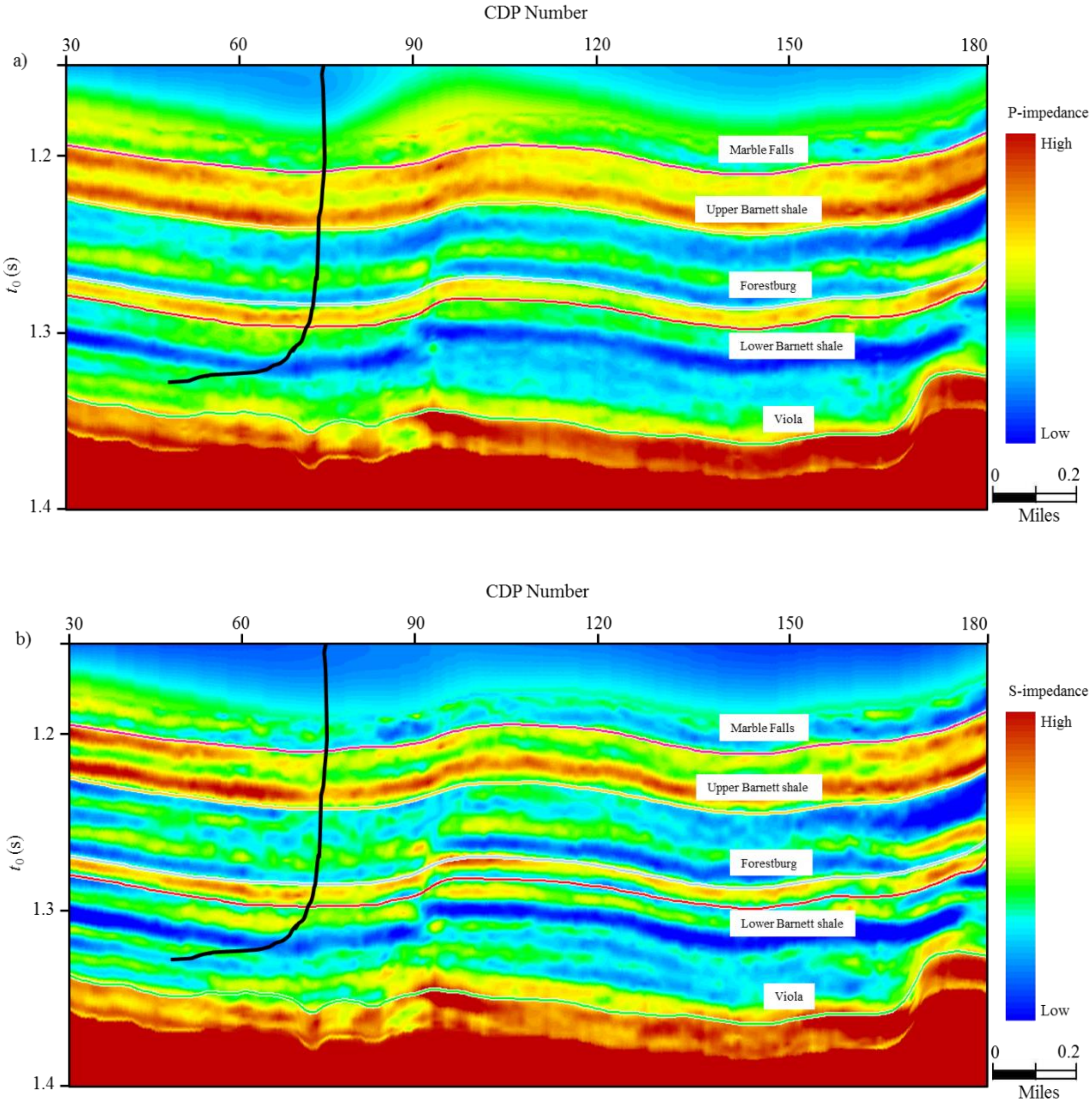
a)
CDP Number
30
60
90
120
150
180
t_0 (s)
1.2
1.3
1.4
Marble Falls
Upper Barnett shale
Forestburg
Lower Barnett shale
Viola
P-impedance
High
Low
0
0.2
Miles
b)
CDP Number
30
60
90
120
150
180
t_0 (s)
1.2
1.3
1.4
Marble Falls
Upper Barnett shale
Forestburg
Lower Barnett shale
Viola
S-impedance
High
Low
0
0.2
Miles

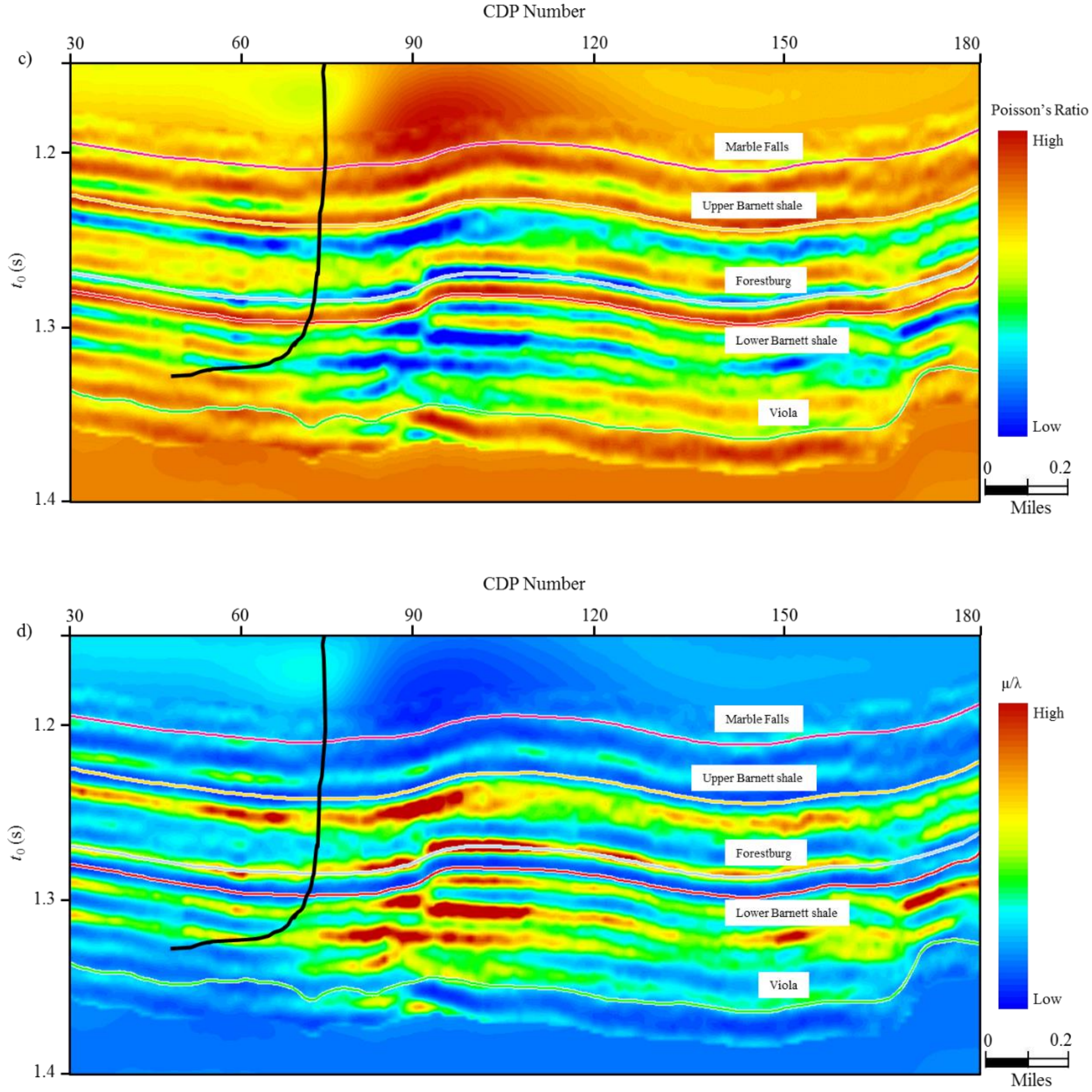

Figure 4.8. Simultaneous prestack inverted (a) P-impedance, (b) S-impedance, (d) Poisson's ratio, and (d) Mu-Lambda ratio.

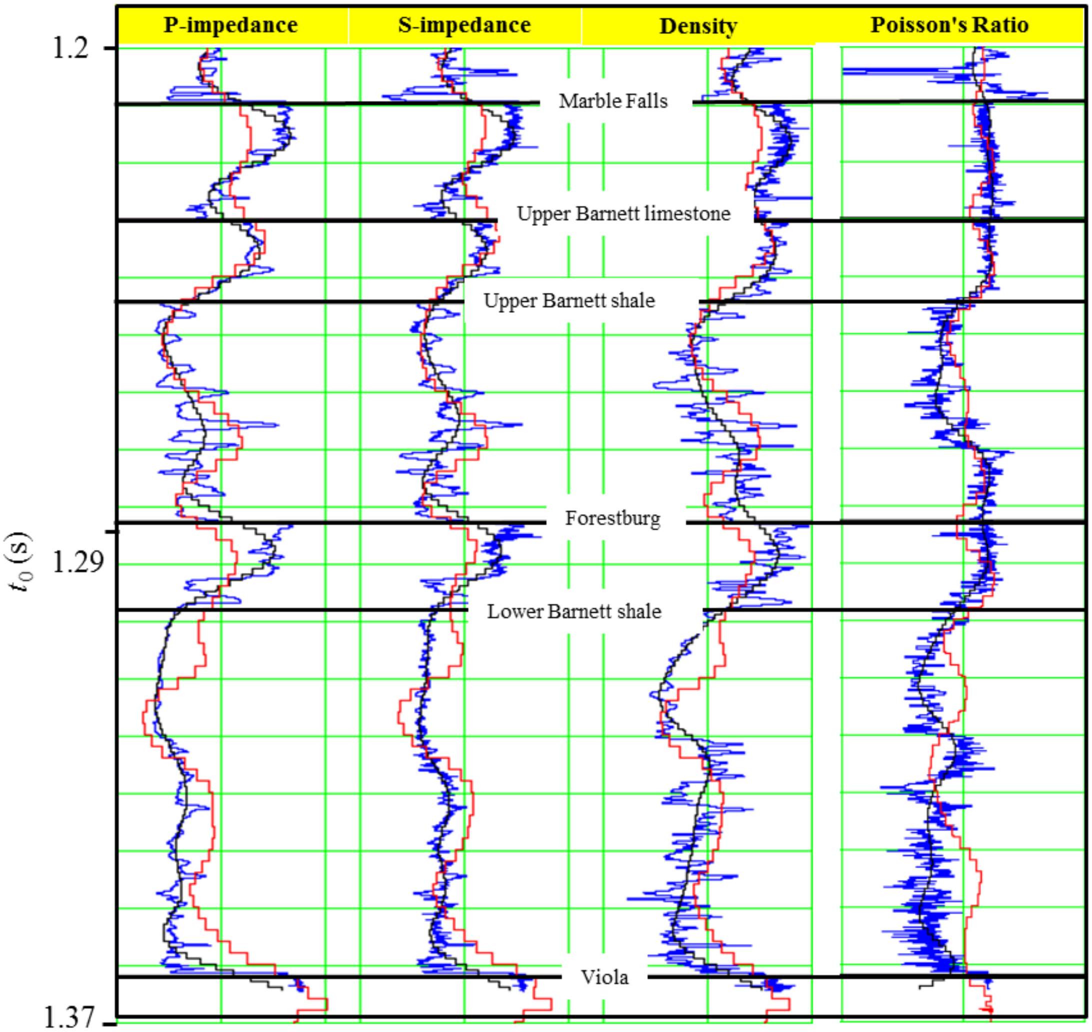

Figure 4.9. Quality control the inverted results with original well logs. The first, second, third, and fourth panels are respective the P-impedance, S-impedance, density logs, and Poisson's ratio. The blue, black, and red curves are respectively the original logs, initial model, and inverted results from seismic gathers.

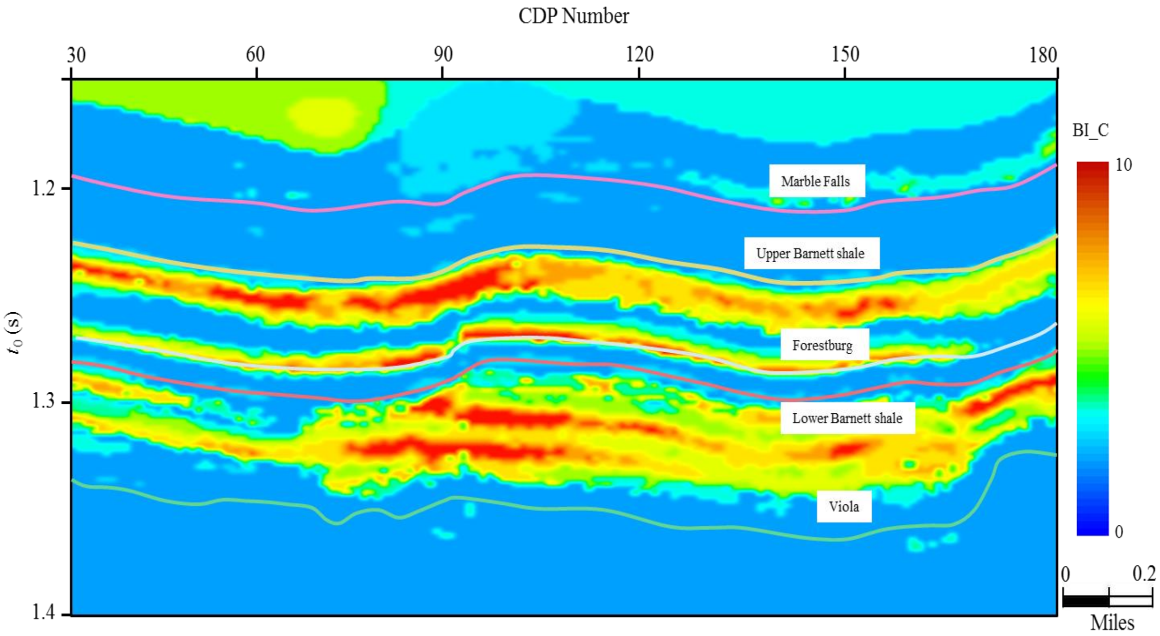

Figure 4.10. Brittleness estimation by applying the classification pattern on the inverted rock properties volumes. We obtained the classification pattern by training the rock properties and BI from bench mark wells using PSVM.

REFERENCES

Altindag, R., and A. Guney, 2010, Predicting the relationships between brittleness and mechanical properties (UCS, TS and SH) of rocks: Scientific Research Essays, **5**, 2107 - 2118.

Coates, D. F., and R. C. Parsons, 1966, Experimental criteria for classification of rock substances: International Journal of Rock Mechanics and Mining Sciences, **3**, 181-189.

Cortes, C. and V. Vapnik, 1995, Support-vector networks: Machine Learning, **20**, 273-297.

Da Silva, M., 2013, Production correlation to 3D seismic attributes in the Barnett Shale, Texas: M.S. thesis, The University of Oklahoma.

Fung, G. M. and O. L. Mangasarian, 2005, Multicategory proximal support vector machine classifiers: Machine Learning, **59**, 77-97.

Goodway, B., T. Chen, and J. Downton, 1997, Improved AVO fluid detection and lithology discrimination using Lamé parameters $\lambda\rho$, $\mu\rho$, and $\frac{\lambda}{\mu}$ fluid stack from P- and S-inversion: 67th Annual International Meeting, SEG Expanded Abstracts, 183-186.

Honda, H., and Y. Sanada, 1956, Hardness of coal: Fuel, **35**, 451-461.

Hucka, V., and B. Das, 1974, Brittleness determination of rocks by different methods: International Journal of Rock Mechanics and Mining Sciences & Geomechanics Abstracts, 389-392.

Jarvie, D. M., R. J. Hill, T. E. Ruble, and R. M. Pollastro, 2007, Unconventional shale-gas systems: the Mississippian Barnett Shale of North-Central Texas as one model for thermogenic shale-gas assessment: AAPG Bulletin, **91**, 475 - 499.

Jin, X., S. Shah, J. C. Roegiers, and B. Zhang, 2014, Fracability Evaluation in Shale Reservoirs - An Integrated Petrophysics and Geomechanics Approach: SPE Annual Technical Conference and Exhibition.

Mangasarian, O. L. and E. W. Wild, 2006, Multisurface proximal support vector machine classification via generalized eigenvalues: IEEE Transactions on Pattern Analysis and Machine Intelligence, **28**, 69-74.

Perez Altamar, R., 2013, Brittleness estimation from seismic measurements in unconventional reservoirs: Application to the Barnett Shale: The University of Oklahoma Ph.D. dissertation.

Rickman, R., M. Mullen, J. Petre, W. Grieser, and D. Kundert, 2008, A practical use of shale petrophysics for stimulation design optimization: All shale plays are not clones of the Barnett shale: SPE Annual Technical Conference and Exhibition.

Wang, F.P., and J. F. W. Gale, 2009, Screening criteria for shale-gas systems: GCAGS Transactions, **59**, 779 - 793.

Zhang, B., K. Zhang, S. Guo, and K. J. Marfurt, 2013, Nonstretching NMO correction of prestack time-migrated gathers using a matching-pursuit algorithm: Geophysics, **78**, U9-U18.

Zhang, B., T. Zhao, J. Qi, and K. J. Marfurt, 2014, Strategies to preserve the data fidelity at far offset: 84th Annual International Meeting, SEG Expanded Abstracts.

Zhang, B., D. Chang, T. Lin, and K. J. Marfurt, 2014, Improving the confidence of prestack inversion by preserving the data fidelity in long offset: Interpretation, under reviewing.

Zhang, B., T. Zhao, J. Qi, and K. J. Marfurt, 2014, Horizon-based semi-automated nonhyperbolic velocity analysis: Geophysics, under reviewing.

Chapter 5: Semi-automated fault interpretation based on seismic attributes

Bo Zhang[1], Yuancheng Liu[2], Michael Pelissier[3], and Nanne Hemstra[2],

[1]The University of Oklahoma, ConocoPhillips School of Geology and Geophysics,

[2]dGB Earth Sciences,

[3]formerly at Marathon Oil Corporation, currently with Roc Oil (Bohai) Company

This paper was published by SEG/AAPG journal Interpretation in 2014.

Title: Semi-automated fault interpretation based on seismic attributes

ABSTRACT

3D fault interpretation is a time consuming and tedious task. Huge efforts have been invested in attempts to accelerate this procedure. We present a novel workflow to perform semi-automated fault illumination that uses a discontinuity attribute as input and provides labeled fault surfaces as output. The procedure is modeled after a biometric algorithm to recognize capillary vein patterns in human fingers. First, a coherence or discontinuity volume is converted to binary form indicating possible fault locations. This binary volume is then skeletonized to produce a suite of fault sticks. Finally, the fault sticks are grouped to construct fault surfaces using a classic triangulation method. The processing in the first two steps is applied time slice by time slice, thereby minimizing the influence of staircase artifacts seen in discontinuity volumes. We illustrate this technique by applying it to a seismic volume acquired over the Netherlands Sector of the North Sea Basin and find that the proposed strategy can produce highly precise fault surfaces.

INTRODUCTION

Faults in the subsurface can act as barriers or efficient avenues for hydrocarbon migration and flow, and often form hydrocarbon traps. Identifying the fault system is one of first steps in seismic interpretation and a key component in developing both exploration and development strategies. However, careful fault interpretation is a highly time-consuming task. Algorithms that facilitate fault interpretation fall into two categories. The first category deals with development and application of attributes that highlight fault locations. The algorithms in the second category are for generating fault surfaces from these attributes volumes.

Coherence/similarity (Bahorich and Farmer, 1995; Marfurt et al., 1998; Gersztenkorn and Marfurt, 1999; Randen et al., 2001), reflector dip (Marfurt, 2006), and curvature (Stewart and Wynn, 2000; Roberts, 2001; Al-Dossary and Marfurt, 2006) are the most popular seismic attributes routinely used to assist in fault interpretation. Unfortunately, attributes in their native form are not generally amenable to semi-automated fault system extraction. Rather, we need to apply additional edge enhancement technology to these attributes to better illuminate faults and minimize human labor. There are a variety of image processing techniques which can enhance fault visualization and detection. AlBinHassan and Marfurt (2003) employed the Hough transforms to enhance faults appearing on time slices. Aarre and Wallet (2011) generalized this workflow to 3D using an efficient add-drop algorithm. Barnes (2006) designed a filter to pass steeply dipping discontinuities which can serve as the first step in automating fault interpretation. Lavialle et al. (2006) proposed a nonlinear filtering approach based on 3D GST analysis that de-noises and preserves faults prior to automatic fault extraction. Image processing techniques applied to seismic attributes usually require a suitable window size. Larger window size not only smears the fault information but also increases the computational cost, while smaller window sizes introduces less smearing but are sensitive to noise.

Almost all automated fault extraction strategies need human intervention from time to time and include three main steps. First, the interpreter selects an appropriate fault-sensitive seismic attribute (e.g., coherence or reflector dip magnitude) to highlight the fault location. Next, the interpreter employs different technologies to transform the attribute volume into a fault likelihood/confidence volume. Finally, the interpreter generates a localized surface to fit a cloud of fault points. Randen et al. (2001) presented a four-step workflow to automatically extract fault surface from an attribute cube. Unfortunately this workflow does not handle X-pattern faults properly. Gibson et al (2003) proposed a two-step strategy to automatically detect the fault surface in 3D seismic data. The first step was to generate a confidence cube based on the coherence attribute. They then generated small patches and least-squares fit those patches to generate a fault surface. In both the Randen et al. (2001) and Gibson et al. (2003) workflows, the challenge lies in how to define a suitable threshold to generate the confidence volume as well as a proper window size to generate the fault surface. Silva et al. (2005) provided greater insight into the ant tracking algorithm proposed by Randen et al. (2001). They reported that this strategy can reduce human interaction from 10 days to 3 days in their testing. Jacquemin and Mallet (2005) proposed a method based on a cascade of two Hough transforms to automatically extract fault surfaces. Cohen et al. (2006) proposed a workflow, which contains four steps to detect and extract fault surfaces in 3D volumes, resulting in a set of one-pixel-thick labeled fault surfaces. Kadlec et al. (2008) presented a method to model faults surface using a growing surface strategy while Dorn et al. (2012) generated fault surfaces through azimuth scanning on horizontal slices, and dip scanning on vertical slices.

In this paper, we present a semi-automated strategy to extract fault surfaces from seismic attributes volumes that requires minimum human intervention. We start by introducing an edge-detection algorithm successfully used in the biometric field. We then use these edges to construct a fault system. Finally we apply our algorithm to a seismic data volume acquired over the Netherlands Sector of the North Sea Basin.

METHOD

Coherence-like attributes typically highlight faults quite well on time/depth slices (Dorn et al., 2012) but usually exhibit a staircase behavior on the vertical sections. Based on this observation, we produce our fault sticks time slice by time slice prior to constructing the fault surfaces in the vertical direction.

Seismic Attribute Conditioning

The fault patterns shown on the time slices (Figure 5.1a) share similar characteristics with capillary vein images of fingers (Figure 5.1b) acquired using infrared light. Based on this observation, we borrow an effective method of extracting vein patterns (Miura et al., 2007) to recognize the fault elements on time slices. In the experiments, Miura et al. (2007) reduced the equal error rate (EER), which evaluates the mismatch ratios of personal identification, to 0.0009%. While the EER in other reported methods ranges from 0.2% to 4%. By calculating the local maximum curvature in cross-sectional profiles of discontinuity attribute on time slices, the algorithm can extract the centerlines of possible fault locations. The output is a binarized volume where 1 indicates possible fault locations and 0 the absence of faults.

Assume that P is an attribute slice and $P(x, y)$ is the value at grid (x, y). We define $P[\xi^{(j)}]$ as a cross-sectional profile acquired from $P(x, y)$ along azimuth j, where $\xi^{(j)}$ is the position sequence number in the profile and (x, y) are respectively the index of inline and crossline number. For a given point of discontinuity attribute on time slice, our method checks the curvature, $k[\xi^{(j)}]$, of cross-sectional profiles, $P[\xi^{(j)}]$, as a function of $\xi^{(j)}$ along azimuth j. The curvature, $k[\xi^{(j)}]$, can be expressed as

$$k\left[\xi^{(j)}\right]=\frac{d^2P\left[\xi^{(j)}\right]/d\left[\xi^{(j)}\right]^2}{\left\{1+\left\{dP\left[\xi^{(j)}\right]/d\left[\xi^{(j)}\right]\right\}^2\right\}^{\frac{3}{2}}}. \tag{1}$$

The shape of the attribute profile, $P[\xi^{(j)}]$, is determined by the type of attribute. For example coherence appears as a low coherence dent (Figure 5.2a) and exhibits negative curvature using equation 1. To simplify the following processing, if the attribute shows low values at the fault location, we reverse the sign of equation 1.

Note that the discontinuity attributes should theoretically reach minimum/maximum value at the fault location and increase/decrease abruptly (Figure 5.2b). We assume that the local maxima, $k[\xi^{(j)}]$, in each profile, $P[\xi^{(j)}]$, indicate the possible fault positions. Those points are defined as center positions $U^{(j)}(x, y)$. To determine whether a center position, $U^{(j)}(x, y)$, has the possibility to lie on the fault location, we compute scores, $S[U^{(j)}(x, y)]$ (Figure 5.2c), defined as

$$S\left[U^{(j)}(x,y)\right]=k\left[U^{(j)}(x,y)\right]\times W\left[U^{(j)}(x,y)\right], \tag{2}$$

where $W[U^{(j)}(x, y)]$ is the local width of the profile where $k(\xi^{(j)})$ is positive (Figure 5.2b), and $k[U^{(j)}(x, y)]$ is valued directly from $k[\xi^{(j)}]$ from location mapping between

(x, y) and $\xi^{(j)}$. The score parameter, $S[U^{(j)}(x,y)]$, considers the width and changing rate of the attribute at the same time. If the score is large, the probability that there is a fault is also high. To obtain the fault pattern development along all azimuths in the entire time slice, the scores are accumulated and assigned to a capability plane (Figure 5.3), $V(x,y)$, which has the same size as the attribute time slice,

$$V(x,y)=\sum_{j}^{J} S\left[U^{(j)}(x,y)\right], \tag{3}$$

where j the index of azimuth direction, J is the number of azimuth and set as 8 in this paper, and (x, y) is the horizontal coordinate pair.

If $V(x, y)$ is large and has large values nearby, we consider this point lying on a fault system. Even if $V(x, y)$ is large but has small values nearby, a dot of noise is interpreted to occur at (x, y). By applying equations 4a to 4d on the capability slice shown in Figure 5.3, Figures 5.4 show the confidence slice, $C(x, y)$, of encountering a fault at 0^{o}, 45^{o}, 90^{o}, and 135^{o} using a strategy described by Miura et al. (2007).

$$C_0(x,y)=\min\{\max[V(x,y+1),V(x,y+2)],\max[V(x,y-1),V(x,y-2)]\},$$

(4a)

$$C_{45}(x,y)=\min\{\max[V(x+1,y+1),V(x+2,y+2)],\max[V(x-1,y-1),V(x-2,y-2)]\},$$

(4b)

$$C_{90}(x,y)=\min\{\max[V(x+1,y),V(x+2,y)],\max[V(x-1,y),V(x-2,y)]\},$$

(4c)

$$C_{135}(x,y)=\min\{\max[V(x+1,y-1),V(x+2,y-2)],\max[V(x-1,y+1),V(x-2,y+2)]\},$$

and (4d).

The final confidence estimate is given by

$$C(x,y)=\max\left[C_0(x,y),C_{45}(x,y),C_{90}(x,y),C_{135}(x,y)\right].$$

(5)

Note fault confidence attributes indicated by the green arrows in Figure 5.5 is more continuous compare to that of Figure 5.3. The improvement is critical in generating the binary slice.

The confidence slice is binarized according to a user-defined threshold (C_{thd} in Figure 5.7). Only those points with values greater than or equal to the threshold are set to 1 and considered as candidate points for the following processing and fault surface construction. All other points are treated as background with a value of 0 (Figure 5.6a).

The above workflow is designed and set to highlight the faults and is applied to the whole seismic attribute cube time slice by time slice. The final result is a binarized cube where the points with value 1 indicate possible fault locations.

Thinning and Connected Component Analysis

Thinning algorithms (e.g., Bag and Harit, 2011) applied to the binarized time slices can approximate the medial lines of the connected candidate points. The results are one-pixel thick lineaments that can also be used to separate different fault surfaces (Cohen et al., 2006). However thinning may generate undesired bifurcation branches (indicated by blue arrows in Figure 5.6b) due to its sensitivity to noise and complex boundaries. Crossing fault surfaces also appear as bifurcated branches (indicated by the red arrows in Figure 5.6b) on the thinned slices. To determine whether a thinned stick has bifurcated branches, we examine the number of connected neighbor pixels (NCNP) for each pixel of current stick. A pixel is considered as the bifurcated point if its NCNP is greater than three and the stick has branches. We use the following criteria to preserve or trim the branches. If the length of the branches is much larger (e.g. three times for the examples shown in this paper) than the local width of the hypothesized binarized result at bifurcated point (e.g. the limb indicated by red arrow in Figure 5.6c), we assume the branches belong to some other fault surface. Otherwise we simply trim the limbs and archive the maximum length of the current element (e.g. the limbs indicated by the blue arrows in Figure 5.6b). The length of the branches is determined by the number of pixel from bifurcated point till the end pixel of current limb (e.g. the length of branches indicated by the red arrow is 19 in Figure 5.6b). To determine the local width for binarized slice at the bifurcated point, we first draw a circle with a diameter of 1 pixel centered at the bifurcated point, and then increase the diameter until a pixel on circle has value of 0 (Figure 5.6a). At last the local width is set as the diameter of the circle (e.g. the width labeled by red arrow is 5 in Figure 5.6a).

Faults, stratigraphic edges, and acquisition footprint all give rise to elongated features on the trimmed time slice. To preserve the fault sticks only, we first use connected component analysis (e.g., Dillencourt et al., 1992) to label all the connected elements. Then we only keep those components whose lengths are greater than or equal to a user-defined value (L_{min} in Figure 5.7). For example the components indicated by yellow arrows in Figure 5.6b are deleted due to their limited length. This threshold also serves as the smallest length of the fault sticks we detect on each time slice. Figure 5.6c is the last output fault stick used for the following fault-generating surface.

Thinning, trimming, and component analysis are applied on the entire binarized cube time slice by time slice, resulting in a suite of linear fault elements on each slice ready for the final fault system construction. Channels often exhibit long linear elements on time slices and survive the initial fault sticks winnowing process. However, channels are stratigraphically limited and will in general only exhibit a few sticks vertically, which provides a means of rejecting them through the use of a vertical continuity threshold.

Interactive Fault Surface Generation

The fault surface projected on the time slice is a suite of curves called fault sticks. Fault sticks on adjacent time slices having similar size and shape are assumed to define the same geologic feature. Based on this assumption, we group the sticks by comparing their size and shape (e.g., Bribiesca and Aguilar, 2006). Starting with a given (source) stick, we search vertically ±4 samples over target sticks that share similar features with the source stick. Once a target stick is joined to the current fault surface, it is deleted from the sticks set and serves as the source stick to determine whether the next target stick is suitable for the current fault system. Once the stick grouping is done, we triangulate (e.g., Hartmann, 1998) the stick groups whose size is greater than or equal to a user defined value (G_{min} in Figure 5.7) to generate a smooth fault surface. The suitable group size can reject not only the single noisy sticks but also the channel-like long sticks. Interactive editing (e.g. merging) to ensure the fidelity of the extracted results is the final process in our workflow.

Figure 5.7 shows workflow which summarizes fault surface extraction strategy in this paper. The input is seismic amplitude cube and outputs are labeled fault surfaces. We need three parameters to control the extraction procedure. The first parameter, C_{thd}, influences the generating of binary cube. The bigger value of C_{thd}, the fewer pixels survive in the following processing. The second parameter, L_{min}, constrains the minimum length of fault sticks on horizontal slice while the third parameter, G_{min}, controls fault surface size on vertical section.

APPLICATION

To demonstrate the capability and efficiency of our algorithm, we apply it to a subvolume of a seismic survey acquired in the Dutch portion of the North Sea Basin. Detailed mapping of the faults is critical to this survey because some of the faults may act as pathways for gas or fluids (Schroot and Schüttenhelm, 2003). The tested volume contains 250 by 200 traces and ranges from 300 ms to 700 ms with a sample interval of 4 ms.

Figure 5.8a shows the seismic cube with a major fault cutting data along one of the vertical faces. We choose coherence (Figure 5.8b) as the fault sensitive attribute. Note that the meandering channel indicated by the green arrow is shown in Figure 5.8b. We generate a capability cube C (Figure 5.9a) from coherence (Figure 5.8b) using the proposed conditioning strategy and scale it to range between 0 and 1. The binary cube is shown in Figure 5.9b with values 1, for $C>0.95$ and 0 for $C<0.95$. Fault sticks generated from thinning and trimming are shown in the Figure 5.10. The previously described trimming successfully removes unwanted branches introduced by the thinning algorithm. Note that we still have unwanted sticks in Figure 5.10 such as noise sticks indicated by the red arrow and the channels sticks indicated by the green arrow. We choose a threshold value of 10 slices (40 ms) for the size of stick group to reject stratigraphic features. Figure 5.11a shows the final automated extracted fault surfaces labeled by different colors. Note that by setting a threshold value of 10 (40 ms) for the size of stick group, the algorithm also deletes sticks belonging to two small faults indicated by the yellow arrows in Figure

5.10. Figure 5.11b is the manually interpreted fault surfaces based on coherence attribute shown in Figure 5.8b. We can see that there is good agreement between the automated and manually interpreted results. To better quality control the results, we respectively show vertical sections (indicated by green arrows in the Figure 5.11a and 5.11b) with automated extracted and manually interpreted faults in Figures 5.11c and 5.11d. The yellow arrows in the Figures 5.11c and 5.11d state our algorithm locate the fault surface better than that of manually interpreted results. Reducing time cost of human is the bright spot of our method. The whole procedure only requires about 5 minutes human intervention to generate all the fault surfaces. However, attribute-based manually interpretation needs about 20 minutes.

DISCUSSION

The size of our subvolume is about 20 Megabytes and whole computational cost is around 15 minutes on a single processor. And the most time consuming step is the generating of confidence cube and it account for about 80% in our example. Through the parallelization of our algorithm, we can heavily speed up the whole extraction procedure. Parameter, C_{thd}, controls whether we can successfully generate desired faults surfaces. Since the cost of binary generating is negligible, our suggestion is that produces several binary cubes by setting different values of C_{thd} and uses the one that has connected pixels (pixels with value 1) at the possible fault locations.

CONCLUSIONS

Understanding the fault system is a critical objective for any structural interpretation. The proposed algorithm and workflow facilitates this procedure by automatically generating fault surfaces from a discontinuity volume. There is no need for the tedious window size testing for attributes conditioning and the whole procedure only needs three threshold values which simplify the fault conditioning process. The first threshold value is used for generating the binary cube. And the second and third threshold values are respectively the lateral length of the fault stick and vertical size of the fault. The lateral length of the sticks controls the fault size apparent on time sections while the vertical size of the stick group determines the size of the fault on the vertical sections. Increasing the size of the stick group required to define a valid fault surface can reject noisy sticks but may reject small faults. Note that the accuracy of our results is highly dependent on the quality of the seismic data. If the seismic data are so noisy that the coherence or other geometric attributes do not approximate faults, or if acquisition footprint is very strong, we do not recommend using an automated interpretation method.

ACKNOWLEDGEMENTS

The authors would like to thank TNO in providing the data and dGB Earth Sciences for the permission to publish this work. We also thank associated editor Arthus Barnes, reviewer Richard Dalley, reviewer Nasher M. AlBinHassanand, and the third anonymous referee. The final version of this paper benefitted tremendously from the comments and suggestions of Dr. Kurt J. Marfurt.

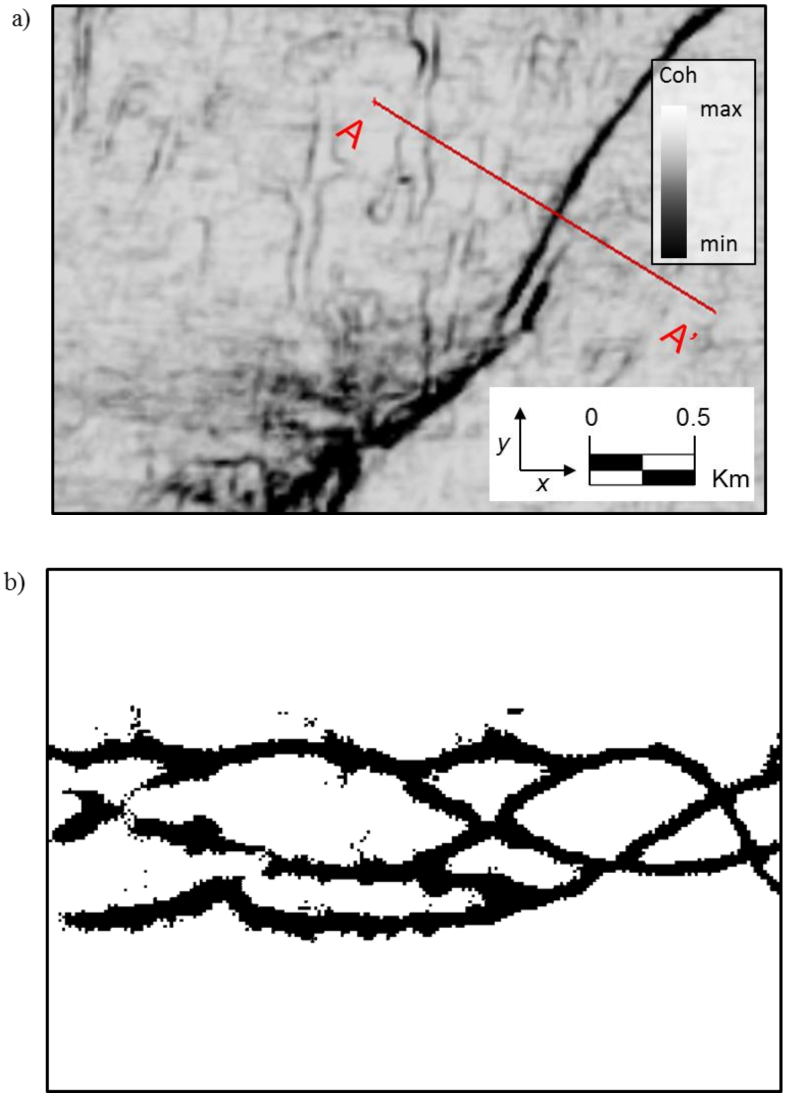

Figure 5.1. Patterns comparison between (a) seismic discontinuity attribute on time slice and (b) binarized vein plane (Modified from Miura et al., 2007). Those two objectives from different field show similar features in the plane.

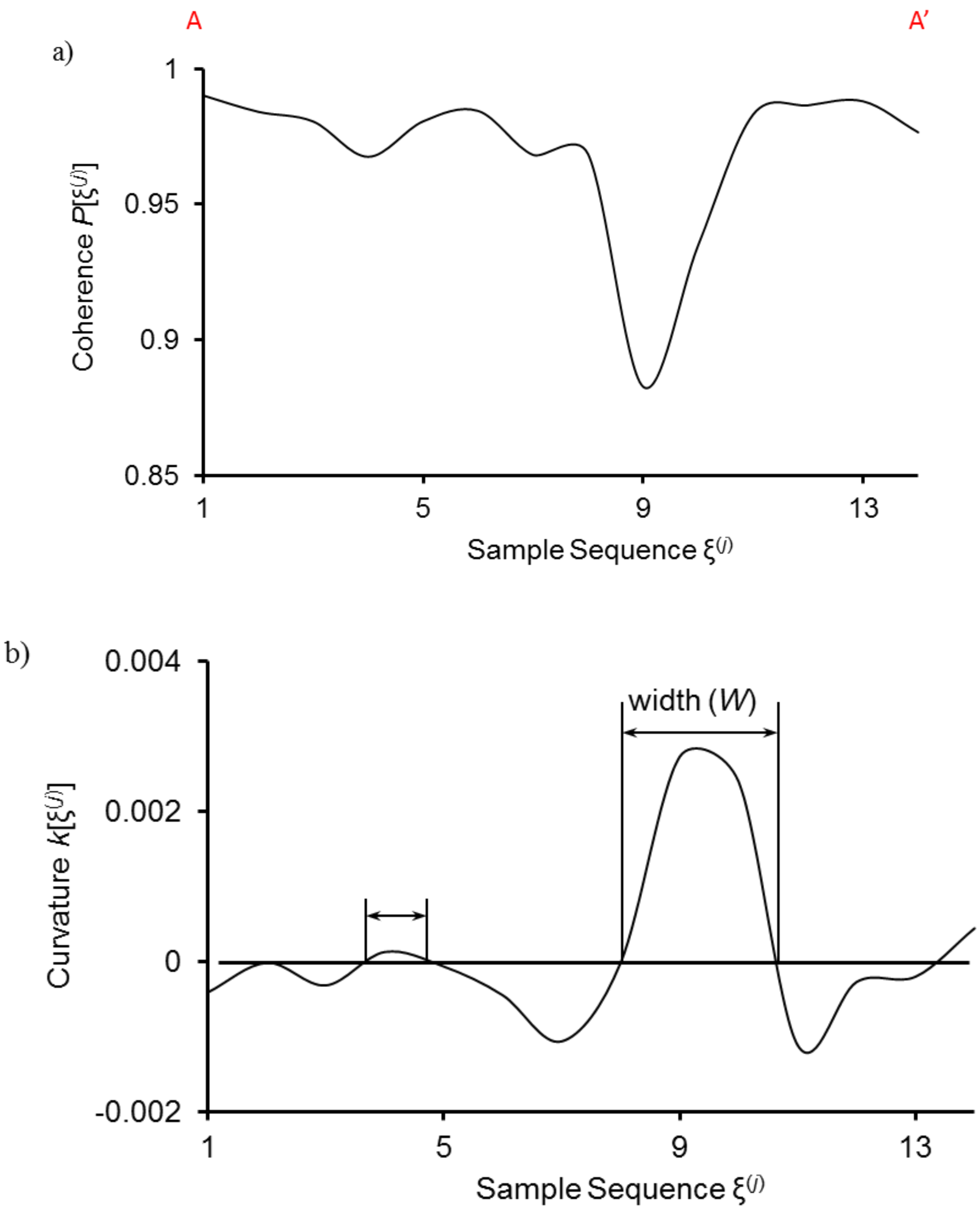
A
A’
a)
1
0.95
0.9
0.85
Coherence $P[\xi^{(j)}]$
1
5
9
13
Sample Sequence $\xi^{(j)}$
b)
0.004
0.002
0
-0.002
Curvature $k[\xi^{(j)}]$
width (*W*)
1
5
9
13
Sample Sequence $\xi^{(j)}$

c)

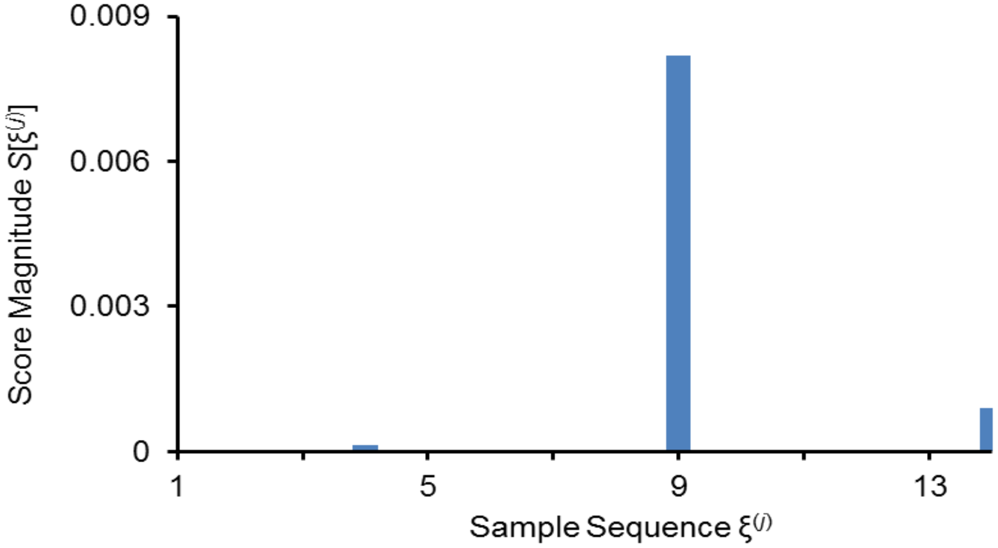

Figure 5.2. Diagrams showing the procedure of seismic attribute conditioning. The attributes value comes from the red line shown in Figure 5.1a. (a) Coherence serves as the input for the fault sensitive attribute. (b) The curvature computed from coherence attribute. (c) The score values used to output binary fault sticks.

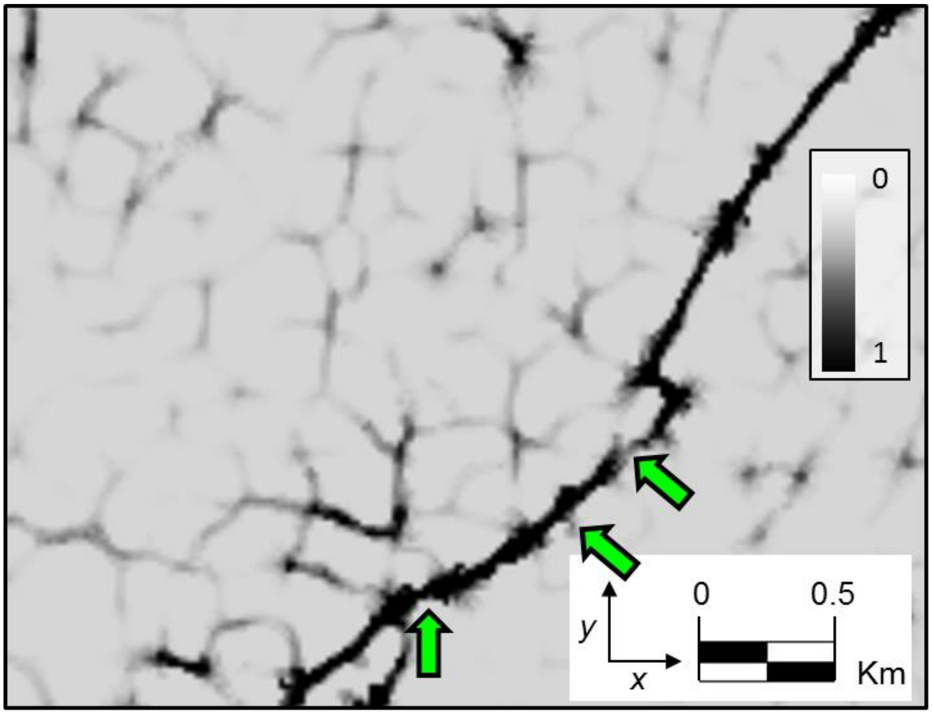

Figure 5.3. Capability time slice computed from the attribute slice shown in Figure 5.1a using the strategy of equation 3.

a)

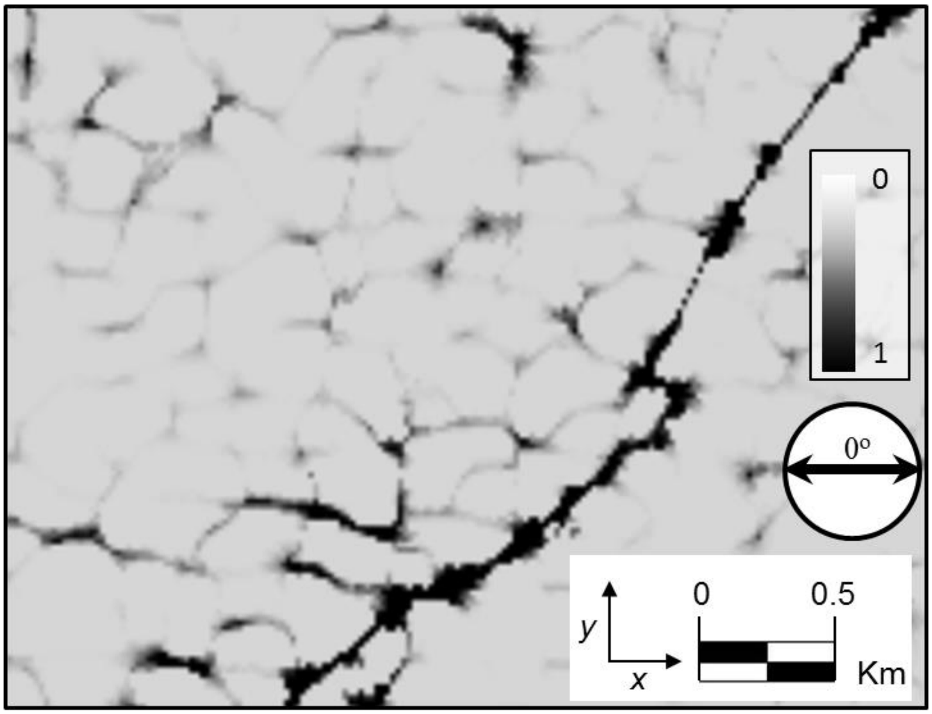

b)

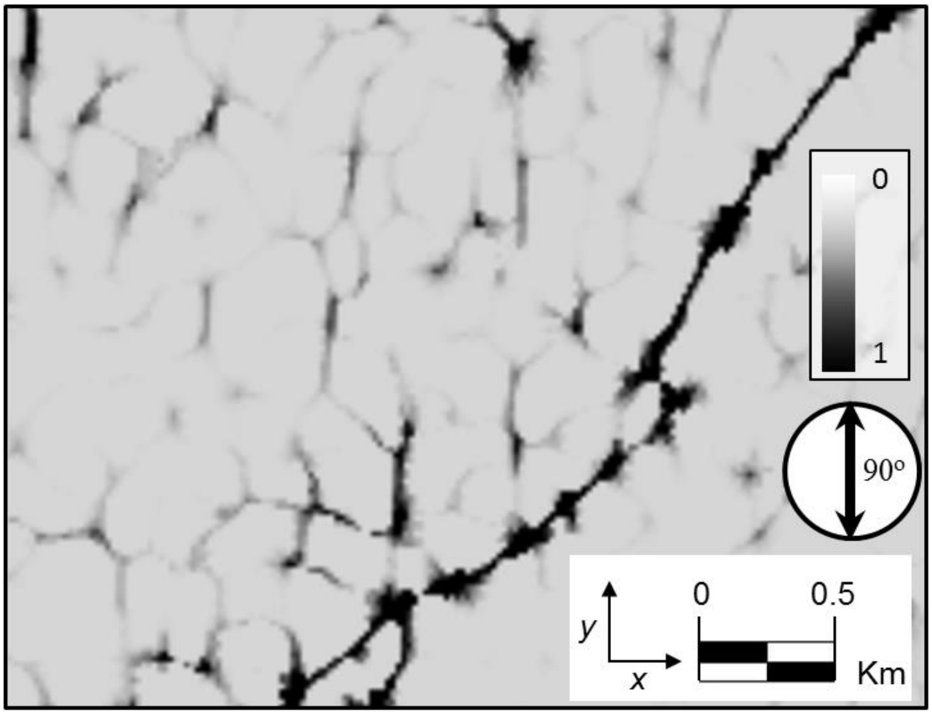

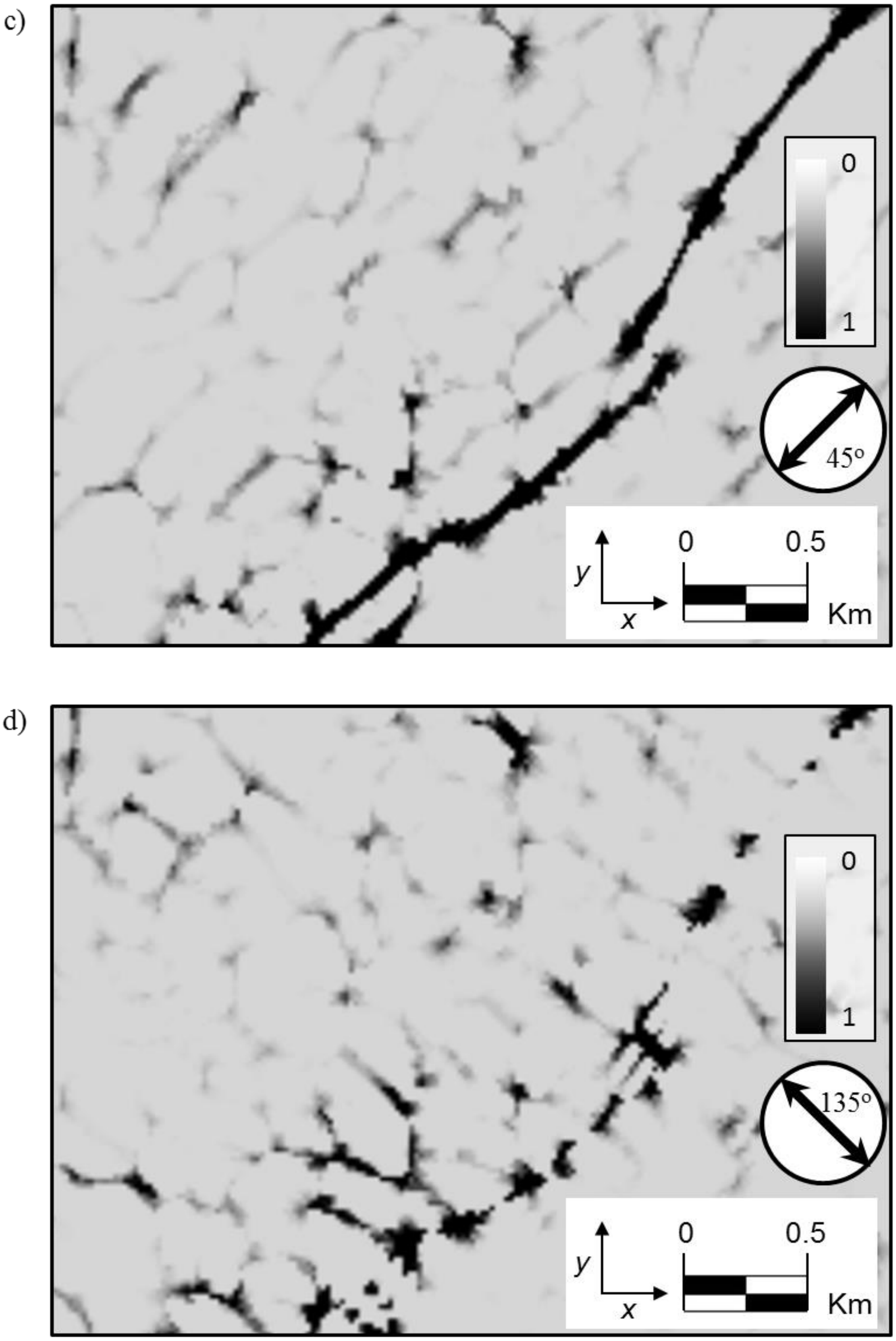

Figure 5.4. Confidence time slices encountering a fault at (a) 0°, (b) 90°, (c) 45° and (d) 135° using equations 4a to 4d applying on the capability time slice shown in Figure 5.3.

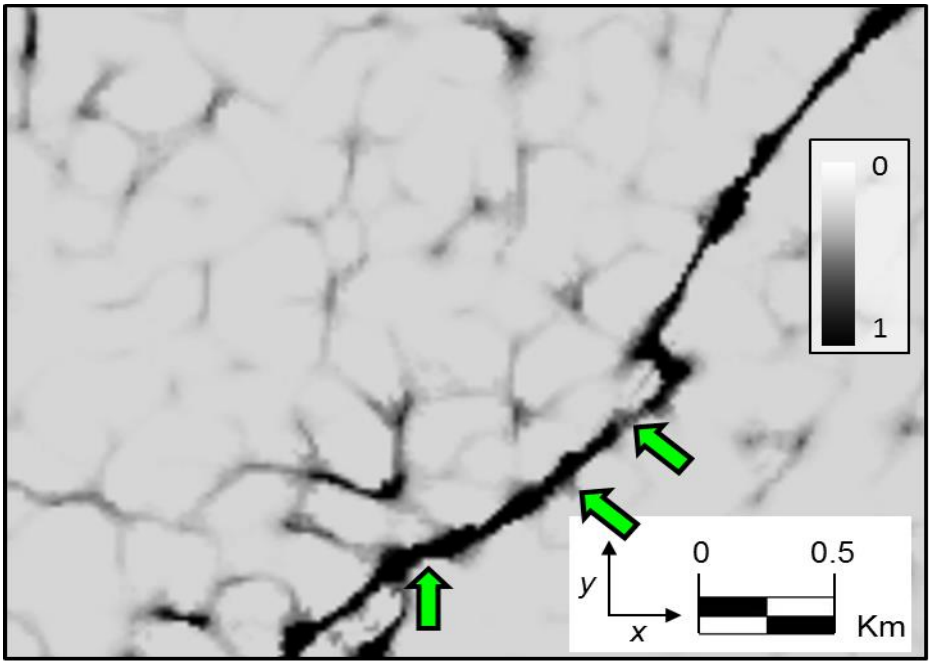

Figure 5.5. The final confidence estimated from Figures 5.4 using equation 5. We scale it to range between 0 and 1.

a)

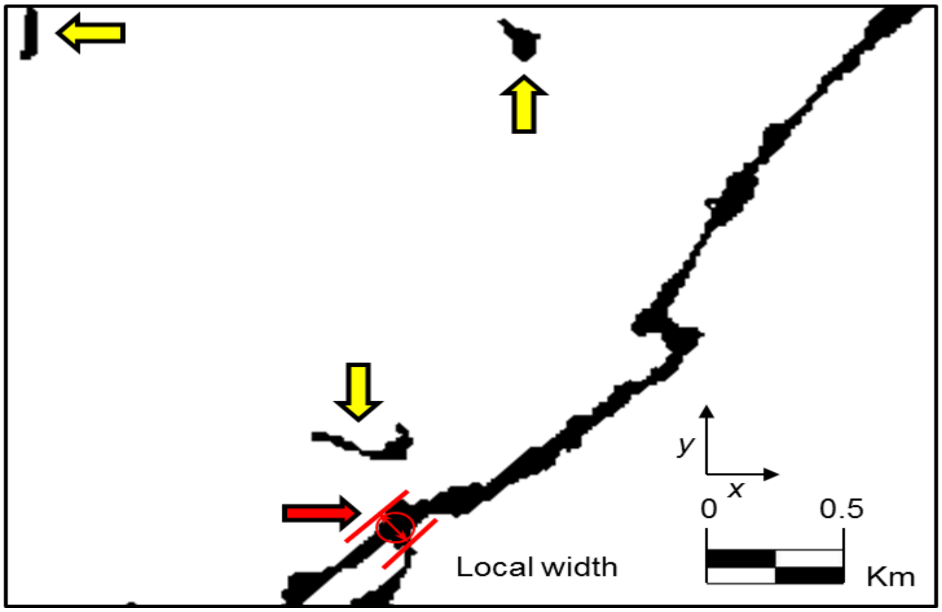

b)

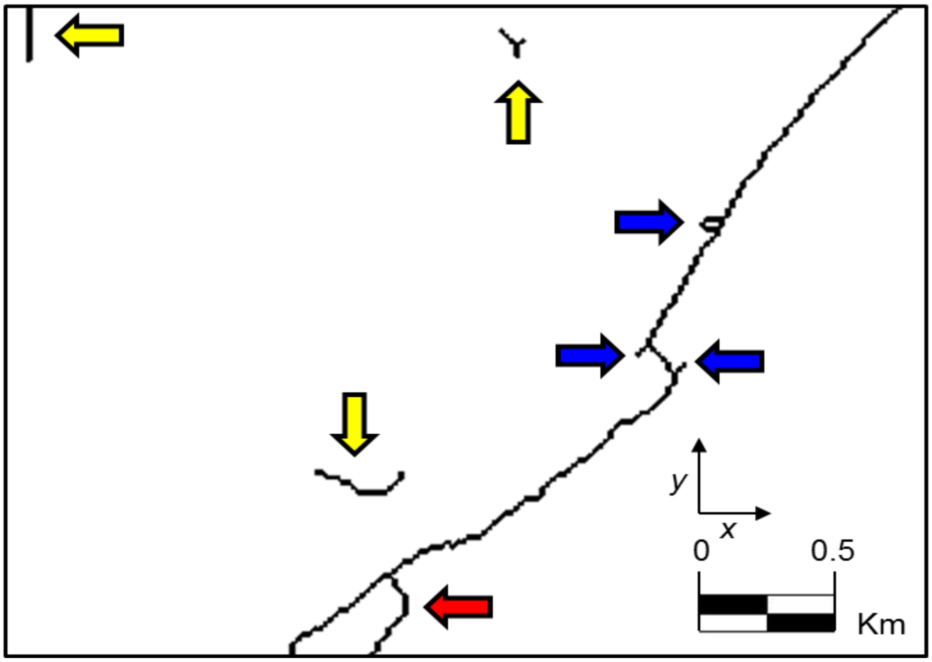

c)

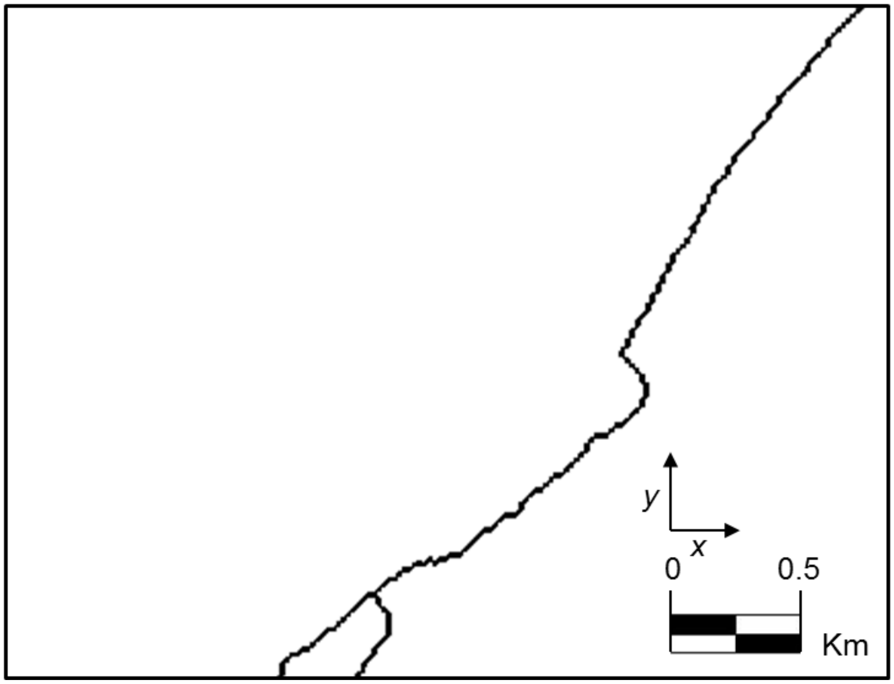

Figure 5.6. (a) Binarized slice after (b) thinning, and (c) trimming processes. The binarization processing is applied on the time slice shown in Figure 5.5. The threshold value used in generating Figure 5.6a is 0.95.

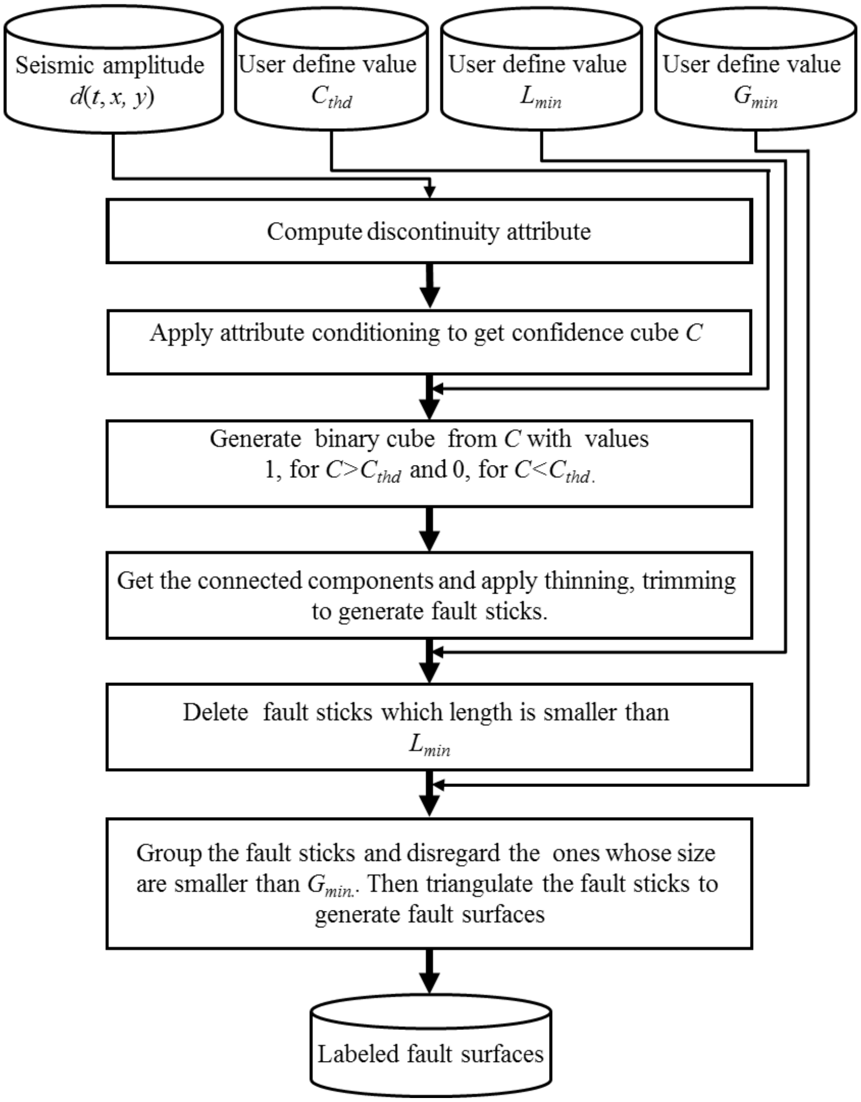

Figure 5.7. Flowchart showing the semi-automated fault interpretation based on seismic attributes. The whole procedure only requires three parameters which simplify the extraction processing.

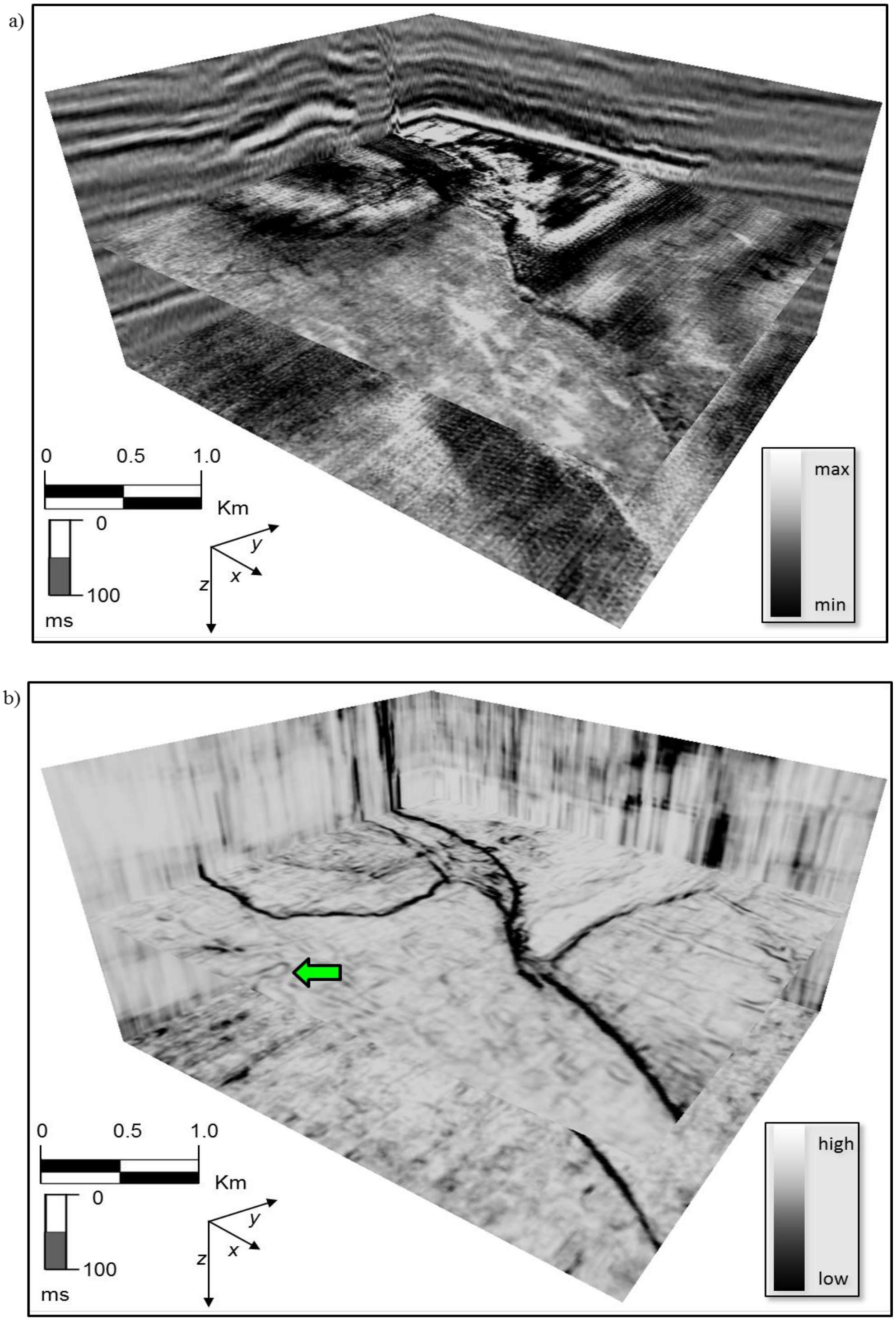

Figure 5.8. (a) Seismic amplitude and (b) coherence cube used for the algorithm testing.

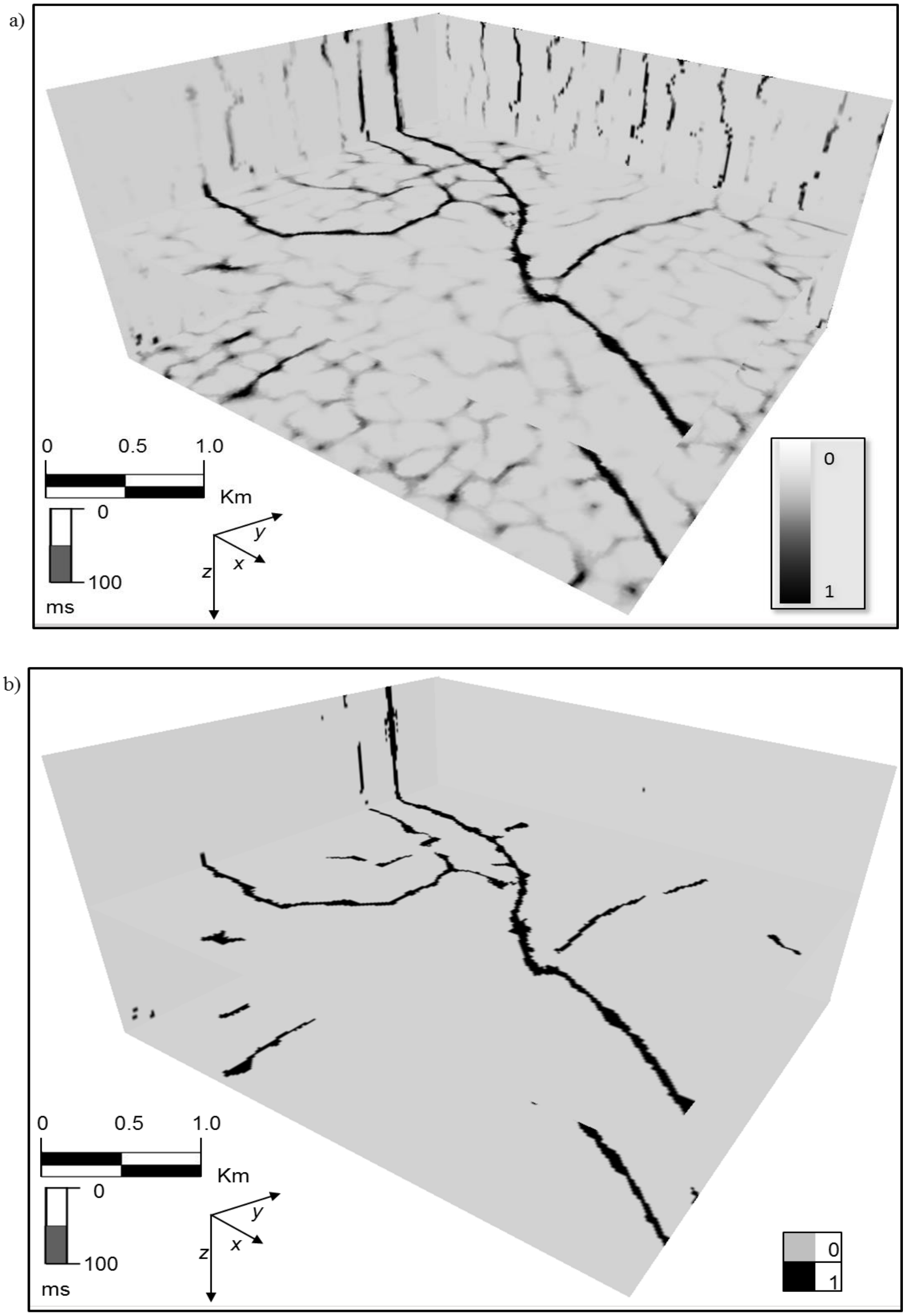

Figure 5.9. (a) Capability and (b) binarized cube computed from coherence attribute shown in Figure 5.8b.

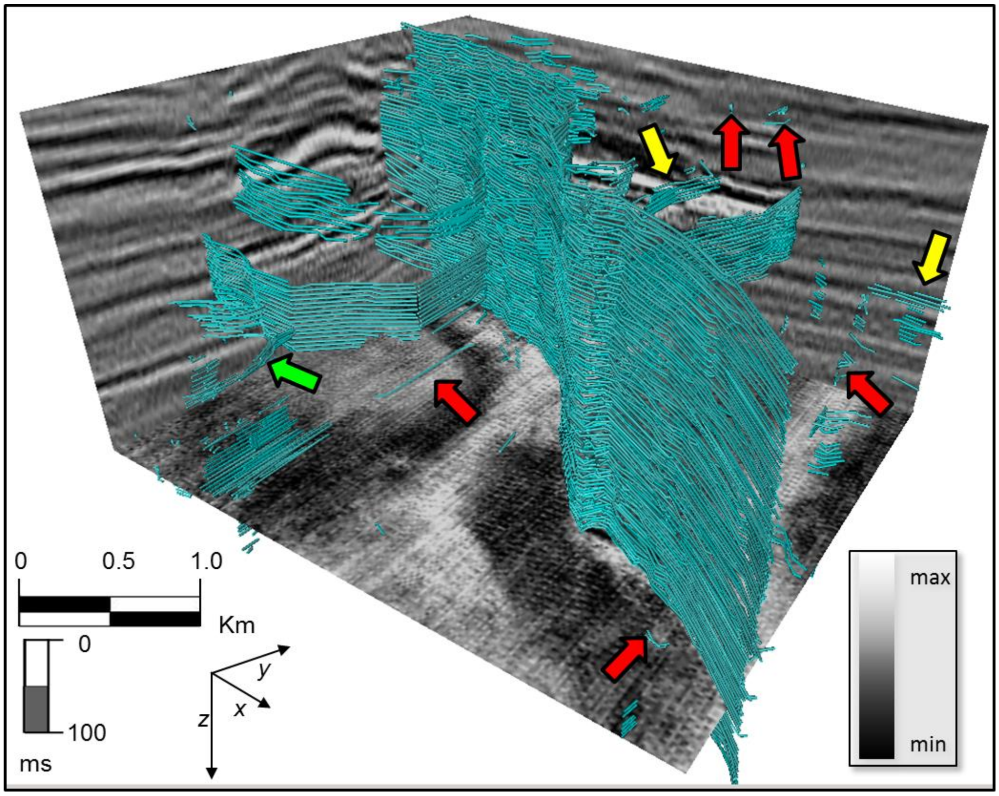

Figure 5.10. 3D view of trimmed fault sticks and original seismic data.

a)

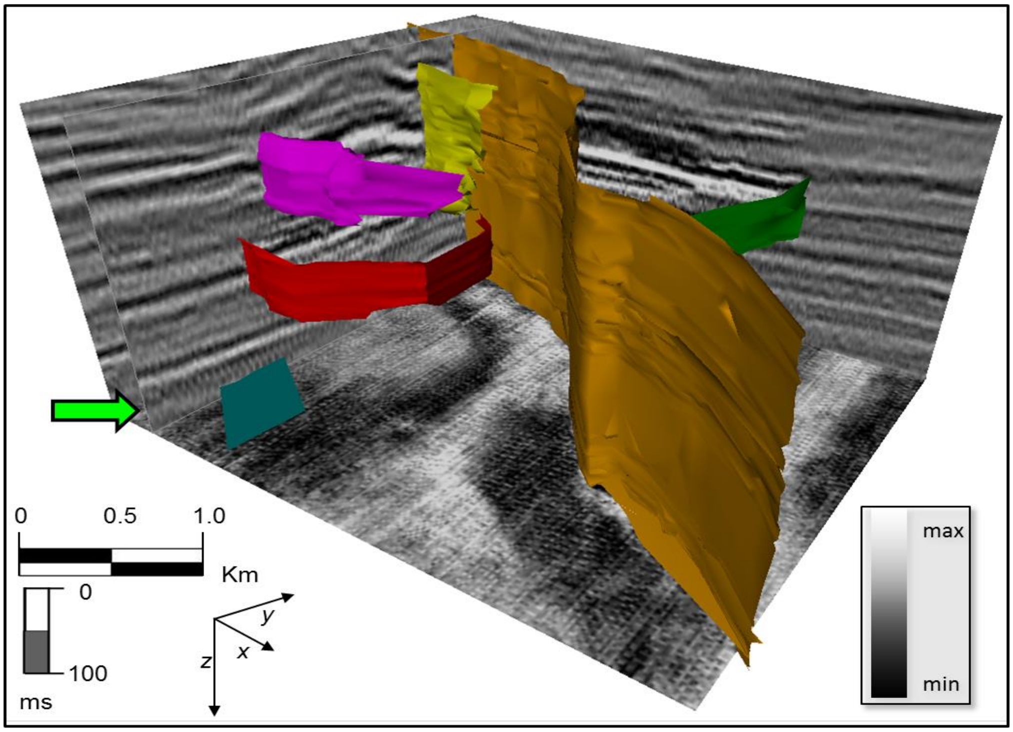

b)

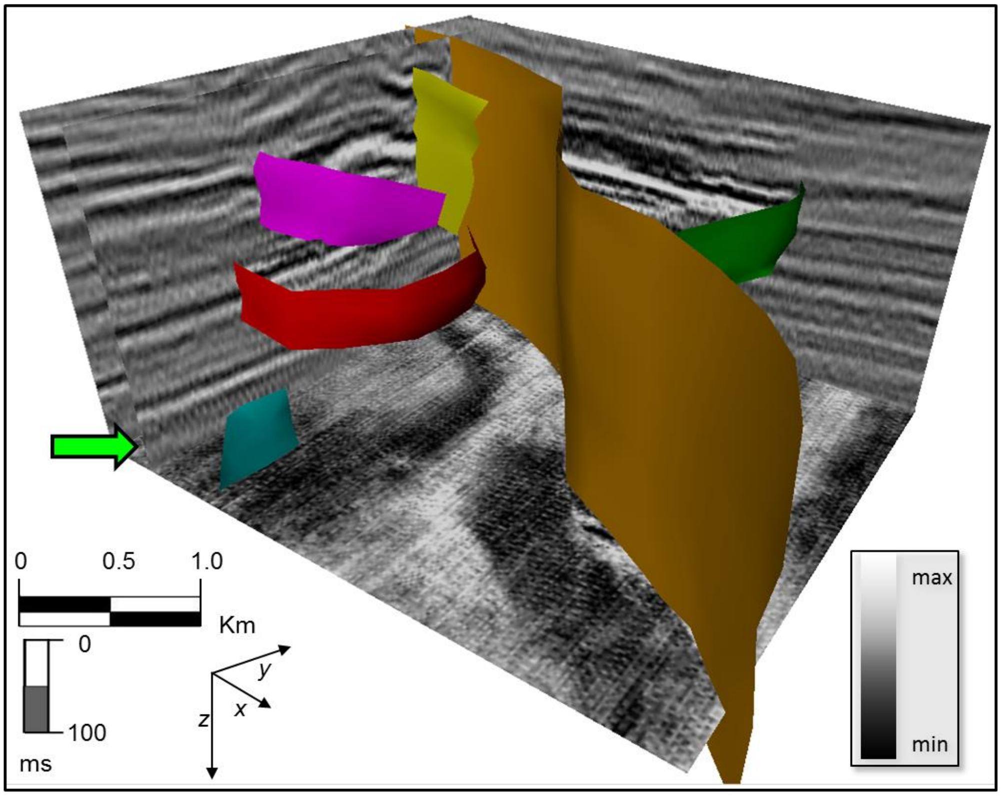

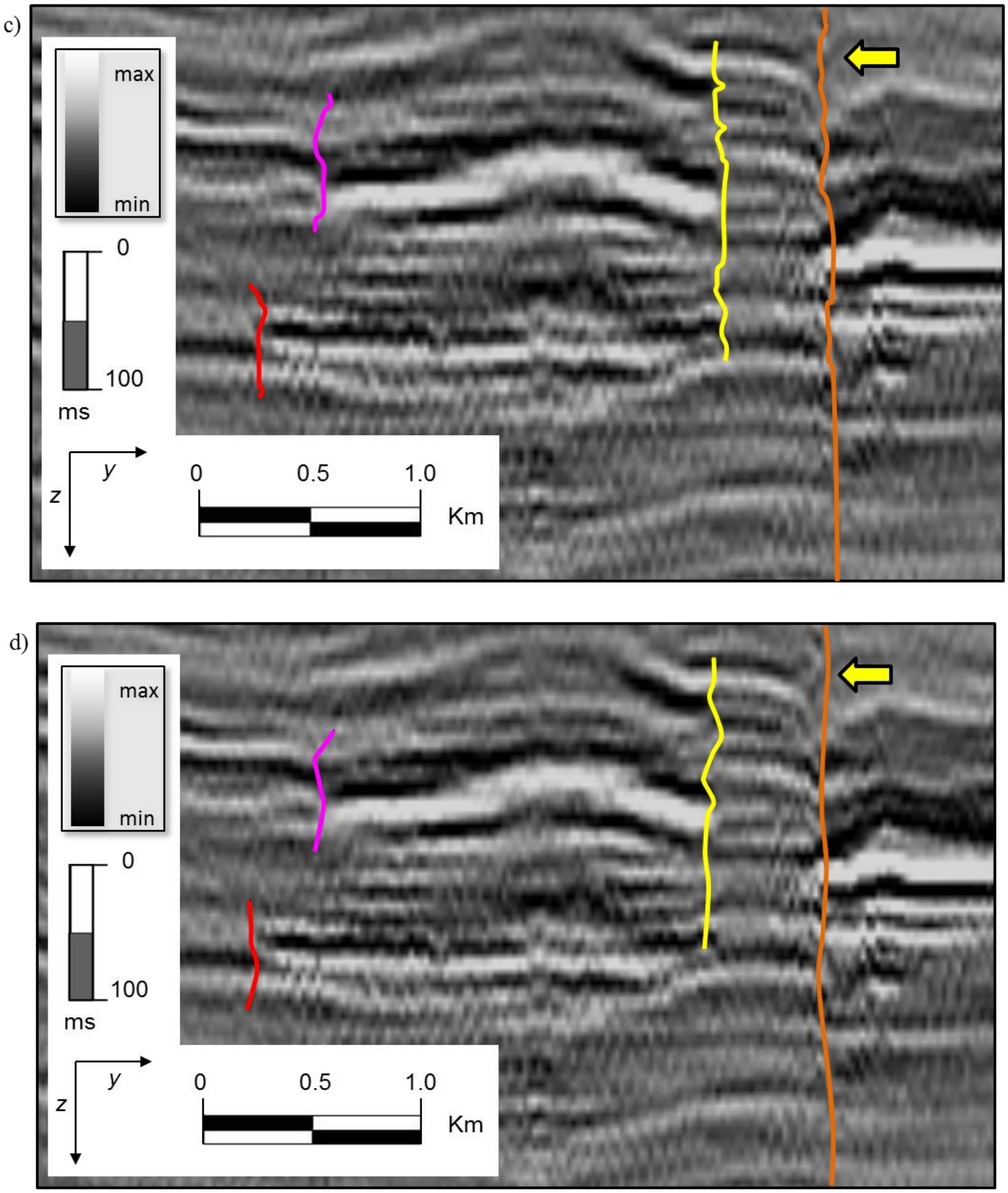

Figure 5.11. Visualization of the fault surfaces and original seismic data. Different color means different fault systems. (a) Extracted fault surfaces using the workflow shown in Figure 5.7. (b) Attribute-based manually interpreted fault surfaces. (c) Vertical section view of extracted fault surfaces. (d) Vertical section view of manually interpreted fault surfaces.

REFERENCES

Aarre, V., and B. Wallet, 2011, A robust and compute-efficient variant of the Radon transform: Processing of the 31st Annual GCSSEPM Foundation Bob F. Perkins Research Conference, 550-586.

AlBinHassan, M. N., and K. J. Marfurt, 2003, Fault detection using Hough transforms: 73rd Annual International Meeting, SEG, Expanded Abstracts, 1719-1721.

Al-Dossary, S., and K. J. Marfurt, 2006, 3D volumetric multispectral estimates of reflector curvature and rotation: Geophysics, **71**, P41-P51.

Bag, S., and G. Harit, 2011, Skeletonizing character images using a modified medial axis-based strategy: International Journal of Pattern Recognition and Artificial Intelligence, **25**, 1035-1054.

Bahorich, M., and S. Farmer, 1995, 3-D seismic discontinuity for faults and stratigraphic features, The coherence cube: 65th Annual International Meeting, SEG, Expanded Abstracts, 93–96.

Barnes, A. E., 2006, A filter to improve seismic discontinuity data for fault interpretation: Geophysics, **71**, P1-P4.

Bribiesca, E. and W. Aguilar, 2006, A measure of shape dissimilarity for 3D curves: International Journal of Contemporary Mathematical Sciences, **1**, 727-751.

Gersztenkorn, A., and K. J. Marfurt, 1999, Eigenstructure-based coherence computations as an aid to 3D structural and stratigraphic mapping: Geophysics, **64**, 1468-1479.

Cohen, I., N. Coult, and A. Vassiliou, 2006, Detection and extraction of fault surfaces in 3D seismic data: Geophysics, **71**, 21-27.

Dillencourt, M., H. Samet, and M. Tamminen, 1992, A general approach to connected component labeling for arbitrary image representations: Journal of the Association for Computing Machinery, **39**, 253-280.

Dorn, G., B. Kadlec, and P. Murtha, 2012, Imaging faults in 3D seismic volumes: 82nd Annual International Meeting, SEG, Expanded Abstracts, 1–5.

Gibson, D., M. Spann, and J. Turner, 2003, Automatic fault detection for 3D seismic data: Proceedings of Digital Image-Techniques and Applications Conference, Expanded Abstracts, **1**, 821-830.

Hartmann, E., 1998, A marching method for the triangulation of surfaces: The Visual Computer, **14**, 95-108.

Jacquemin, P., and J. L. Mallet, 2005, Automatic faults extraction using double Hough transform: 75th Annual International Meeting, SEG, Expanded Abstracts, 755-758.

Kadlec, B. J., G. A. Dorn, H. M. Tufo, and D. A. Yuen, 2008, Interactive 3-D computation of fault surfaces using level sets: Visual Geoscience, **13**, 133–138.

Lavialle, O., S. Pop, C. Germain, M. Donias, S. Guillon, N. Keskes, and Y. Berthoumieu, 2006, Seismic fault preserving diffusion: Journal of Applied Geophysics, **61**, 132-141.

Marfurt, K. J., 2006, Robust estimates of 3D reflector dip and azimuth: Geophysics, **71**, 29-40.

Marfurt, K. J., R. L. Kirlin, S. H. Farmer, and M. S. Bahorich, 1998, 3D seismic attributes using a running window semblance-based algorithm: Geophysics, **63**, 1150–1165.

Miura, N., A. Nagasaka, and T. Miyatake, 2007, Extraction of finger-vein patterns using maximum curvature points in image profiles: IEICE TRANSACTIONS on Information and Systems, **E90-D**, 1185-1194.

Randen, T., S. I. Pedersen, and L. Sønnelan, 2001, Automatic extraction of fault surfaces from three-dimensional seismic data: 71th Annual International Meeting, SEG, Expanded Abstracts, 551-554.

Roberts, A., 2001, Curvature attributes and their application to 3D interpretation horizons: First Break, **19**, 85-100

Schroot B. M., and R. T. E. Schüttenhelm, 2003, Expressions of shallow gas in the Netherlands North Sea: Netherlands Journal of Geoscience, **82**, 91-105.

Silva, C., C. Marcolino, and F. Lima, 2005, Automatic fault extraction using ant tracking algorithm in the Marlim South Field, Campos Basin: 75th Annual International Meeting, SEG, Expanded Abstracts, 857-860.

Stewart, S. A., and T. J. Wynn, 2000, Mapping spatial variation in rock properties in relationship to scale-dependent structure using spectral curvature: Geology, **28**, 691–694.